Impact of Vibrational Nonequilibrium on the Simulation and Modeling of Dual-Mode Scramjets

by

Romain Fiévet

A dissertation submitted in partial fulfillment
of the requirements for the degree of
Doctor of Philosophy
(Aerospace Engineering)
in The University of Michigan
2018

Doctoral Committee:

Professor Venkat Raman, Chair
Professor James F. Driscoll
Assistant Professor Mirko Gamba
Associate Professor Eric Johnsen

Romain Fiévet

rfievet@umich.edu

ORCID iD: 0000-0002-6149-2067

ACKNOWLEDGEMENTS

The work presented in this dissertation is the culmination of an almost six-year-long adventure which started in Austin, in 2012. First, I thank my parents for their unrelenting support throughout these years. I also am extremely grateful to Charles Tinney for offering me the opportunity to join an aerospace doctorate program in the US. Of course, I feel equally grateful to Venkat Raman for his support, assistance and mentoring during my time in Michigan. A lot of this work has been made possible by the previous efforts of Heeseok Koo, whom I warmly thank for his help. I also acknowledge the fruitful collaboration with Stephen Voelkel, whose QCT rates were used in several projects. Besides, I thank my committee for their work in reviewing my thesis.

Many fellow graduate students from other research groups have helped me in the past few years. Back in UT Austin, Woutijn Baars has been a great lab-mate, and certainly put me on the right track to start doing research. I would like to thank Robin Hunt for sharing her experimental data, and for our many discussions on pseudoshock physics. I also thank Rohan Morajkar for teaching me the Triple Decomposition Method. I am also very grateful to Eric Parish for discussions on Bayesian methods, and chess practice. Of course, I thank all the people who answered the calls to discuss less-CFD related topics over Kwak(s) at Ashley's. They will recognize themselves.

Finally, this work was financially supported through an AFRL grant FA9550-12-1-0460 with Dr. Ivett Leyva as the program Manager. I also gratefully acknowledge the generous allocation of computing time by NASA High-End Computing (HEC) Program through the NASA Advanced Supercomputing (NAS) Division at Ames Research Center.

TABLE OF CONTENTS

LIST OF FIGURES

Figure

LIST OF TABLES

Table

LIST OF APPENDICES

Appendix

LIST OF ABBREVIATIONS

BPR Back Pressure Ratio, ratio between outflow and inflow static pressures

CFD Computational Fluid Dynamic

CFL CourantFriedrichsLewy number

CPG Calorically Perfect Gas

DMSJ Dual-Mode Scramjet

DNS Direct Numerical Simulation

FANS Favre-Averaged Numerical Simulation

$\mathcal{FT}$ Fourier transform

GA Genetic Algorithm

iLES implicit Large Eddy Simulation

LES Large Eddy Simulation

LTMW Landau-Teller+Millikan-White correlations

MAP Maximum-A-Posteriori

NST Normal Shock Train

OST Oblique Shock Train

PRR Pressure Rise Ratio throughout the pseudoshock

PRR_{McL} pseudoshock Pressure Rise Ratio predicted by Mc Lafferty theory

PRR_{NS} Normal shock pressure Rise Ratio

PRR_{1D} pseudoshock Pressure Rise Ratio predicted by the 1D model

PSL Pseudoshock length

RANS Reynolds-Averaged Numerical Simulation

STBLI Shock Turbulent Boundary Layer Interaction

$\mathcal{SSA}$ Single-sided amplitude spectrum

TPG Thermally Perfect Gas

TST Thermal Shock Train

1D One-dimensional

3D Three-dimensional

LIST OF SYMBOLS

Roman characters

a	1D model roll-off scalar
A	Channel cross-sectional area [m^2]
A_*	Channel cross-sectional displacement thickness area [m^2]
A_θ	Channel cross-sectional momentum thickness area [m^2]
A_c	1D model Core flow area [m^2]
$\mathcal{A}$	Channel cross-sectional boundary thickness area normalized by channel area
$\mathcal{A}_*$	Channel cross-sectional displacement thickness area normalized by channel area
$\mathcal{A}_\theta$	Channel cross-sectional momentum thickness area normalized by channel area
b	1D model roll-off power law
$\mathcal{B}$	Boltzmann distribution
c	1D model roll-off sensitivity to Mach or speed of sound [$m.s^{-1}$]
c_p	Specific heat capacity at constant pressure [$J.K^{-1}.kg^{-1}$]
c_v	Specific heat capacity at constant volume [$J.K^{-1}.kg^{-1}$]
C_f	Wall skin friction
C_{f1D}	Wall skin friction used in the 1D model throughout the pseudoshock
$\mathcal{C}$	Conservative variable vector
d	1D model friction offset
D	Pipe diameter [m]
D_h	Channel hydraulic diameter [m]
e	1D model friction multiplier or specific internal energy [$J.kg^{-1}$]
e_T	Specific total energy [$J.kg^{-1}$]
e_tr	Sum of the specific translational and rotational energies [$J.kg^{-1}$]
e_trk	Sum of the specific translational, rotational and kinetic energies [$J.kg^{-1}$]
$E_{\psi,\chi}$	1D model error using parameter population ψ on cases χ
$\mathcal{E}$	Generic error function
f	Frequency [Hz]
f_r	Resonance frequency [Hz]
F	Flow thrust [Pa]
$\mathcal{F}$	Cell face flux of a conservative variable
$\mathcal{G}(x)$	Gaussian distribution of x
h	Channel half-height [m] or specific enthalpy [$J.kg^{-1}$]
$\hbar$	Reduced Planck constant [$m^2.kg.s^{-2}$]
H	Channel height or planar jet height [m] or internal enthalpy [J]

k	Turbulent kinetic energy [$m^2.^{-2}$]
k_b	Boltzmann constant [$m^2.kg.s^{-2}.K^{-1}$]
k_{ref}	1D model pressure growth rate constant
K	Bulk specific kinetic energy [$m^2.^{-2}$]
L	pseudoshock length [m]
L_{1D}	1D model pseudoshock length [m]
m	Molecule mass [kg]
$\dot{m}$	Mass flow rate [$kg.s^{-1}$]
M	Mach number
M_{app}	Apparent Mach number
M_{ref}	1D model roll-off reference Mach number
n_i	Molecule translational quantum numbers in space
n_r	Molecule rotational quantum number
n_t	Molecule vibrational quantum number
N_{par}	Number of model parameters
P	Static pressure [Pa]
$\dot{P}_i$	Centerline static pressure at shock number i from inlet [Pa]
$\tilde{P}_i$	Pressure of shock number i from inlet computed from normal shock relations [Pa]
P_{in}	Inflow static pressure [Pa]
P_{out}	Outflow static pressure [Pa]
$Prob$	Marginal probability
P_t	Total pressure [Pa]
Pr	Prandtl number
q	Kinetic energy density [$J.m^{-3}$]
$\dot{q}$	Heat flux [$J.m^{-2}s^{-1}$]
q_{app}	Apparent kinetic energy density [$J.m^{-3}$]
Q	Partition function
R	Specific gas constant [$J.K^{-1}.kg^{-1}$]
R_u	Universal gas constant [$J.K^{-1}.mol^{-1}$]
Re	Reynolds number
Re_δ	Reynolds number based on boundary layer thickness
Re_{δ^*}	Reynolds number based on boundary layer displacement thickness
Re_θ	Reynolds number based on boundary layer momentum thickness
S	Entropy [$m^2.kg.s^{-2}.K^{-1}$]
T	Static temperature [K]
T_t	Total temperature [K]
u_i	Velocity vector component along direction x_i
U_{sta}	Thrust-averaged speed [$m.s^{-1}$]
U_{rel}	Relative velocity respect to shock frame [$m.s^{-1}$]
$V(\mathbf{r})$	Potential field where the molecule evolves
x	Streamwise coordinate [m]
x_X	Streamwise coordinate of the X% pressure rise location [m]
x_f	Streamwise coordinate of the pseudoshock foot [m]
x_t	Streamwise coordinate of the pseudoshock tail [m]

x_{si}	Streamwise coordinate of the i-th shock from the pseudoshock foot [m]
$\mathcal{X}(x)$	Normalized coordinate of x by mean(x) for distributions plots
y	Wall-normal coordinate (vertical) [m]

Greek characters

α	1D model skin friction coefficient power
β	1D model recovery efficiency power
γ	Gas specific heat ratio
δ	Boundary layer thickness [m]
δ^*	Boundary displacement thickness [m]
ϵ	Turbulence dissipation rate [$m^2.s^{-3}$]
ϵ_r	Molecule rotational energy [J]
ϵ_t	Molecule translational energy [J]
ϵ_v	Molecule vibrational energy [J]
$\mathcal{E}_X$	Oscillation amplitude of the X% pressure rise location [m]
$\mathcal{E}_{X-Y}$	Oscillation amplitude of the difference between X and Y% pressure rise location [m]
$\mathcal{E}_f$	Oscillation amplitude of the pseudoshock foot [m]
$\mathcal{E}_t$	Oscillation amplitude of the pseudoshock tail [m]
$\mathcal{E}_{BPR}$	Back pressure ratio oscillation amplitude [Pa]
θ	Boundary momentum thickness [m]
κ	1D model pressure growth rate roll-off power law or Kolmogorov lengthscale [m]
λ	Thermal conductivity [$m^2.s^{-1}$]
$\lambda_{v\,\alpha}$	Vibrational thermal conductivity [$m^2.s^{-1}$]
μ	Gas dynamic viscosity [$kg.m^{-1}.s^{-1}$]
ν	Gas kinetic viscosity [$m^2.s^{-1}$]
ξ	Shock train local stiffness for anharmonic oscillator analogy
ρ	Fluid density [$kg.m^{-3}$]
σ	McLafferty's pressure recovery efficiency factor
σ_i	Margin of error for data-element i for the likelihood function
τ_0	pseudoshock convection timescale between oscillation bounds
τ_c	Computational domain flow-through timescale
τ_{ij}	Newtonian stress tensor element [$kg.m^{-1}.s^{-2}$]
ϕ_i	Vibrational state population density
$\varphi(T, T_v)$	Chemical reaction efficiency factor
ϕ_X	Phase lag between X% pressure rise location and pseudoshock foot [rad]
ϕ_t	Phase lag between pseudoshock tail and foot [rad]
χ	Set of cases used to calibrate the 1D model parameters
ψ	Population of 1D model parameters
Ψ	Molecular wave function
ω	Pulsation [Hz]
ω_0	Natural pulsation [Hz]

Subscripts

0	Bulk flow values upstream of pseudoshock

1	Flux-conserved flow values upstream of pseudoshock
2	Flux-conserved flow values downstream of pseudoshock
app	*Apparent* state accounting for shocks relative velocity
in	Inflow value
out	Outflow value
ref	Constant value of reference
sta	Stream-thrust averaged value

Superscripts

X'	Signal X fluctuations around Reynolds-average value (unit of X)
X''	Signal X fluctuations around Favre-average value (unit of X)
$\overline{X}$	Signal X Reynolds-average value (unit of X)
$\tilde{X}$	Signal X Favre-average value (unit of X)
X^*	Equilibrated value of thermodynamic variable X (unit of X)

Others

∂	Partial derivative
Δ	Gradient
$\oslash$	Diameter
$\star$	Convolution product
$\sum$	Summation
$\prod$	Product
$\propto$	Proportional
$\approx$	Approximate

ABSTRACT

The practical realization of supersonic flight relies on the development of a robust propulsion system. These air-breathing scramjet engines process fuel and high-speed air to generate propulsive thrust. Unlike conventional jet engines, scramjets achieve efficient thrust by compressing air through a system of shocks. As a result, the reliability of the engine is highly sensitive to the stability of these shock structures. Physically, these shocks are located in an engine component called the isolator. The shock structures are spatially distributed leading to a region of pressure increase, which is termed the pseudoshock. As vehicle operating conditions change, the length of the pseudoshock will change, reflecting changes to inflow conditions and operation of downstream combustor component. The overall objective of this thesis is to understand the complex flow inside these isolators.

Of particular focus is the role of molecular processes in the development of the shocks. At high enthalpy conditions, the internal motions of the molecules are moved out of equilibrium due to compression shocks, which affects not only the thermophysical properties of air, but more critically the fuel-air mixing and chemical reactions. While there exists a vast body of literature on scramjet isolators, almost all of these works focus on low enthalpy conditions due to laboratory experimental limitations, or simply rely on equilibrium thermodynamics. In this work, the effect of nonequilibrium on isolator and scramjet combustors at high-altitude high-enthalpy flight conditions was studied using high-fidelity numerical simulations. Detailed models for the description of molecular nonequilibrium, in the form of multi-temperature model was used. Computational chemistry derived reaction rates were used to describe the combustion processes.

These studies revealed the following key features: a) nonequilibrium of vibrational states

greatly increases pseudoshock length, b) contrary to external hypersonics, nonequilibrium accelerates chemical reactions in the combustor, reducing the distance from fuel injection to flame ignition and stabilization, c) while multi-temperature models are adequate to express such nonequilibrium effects, more detailed state-specific representations clearly demonstrate that molecular populations do not follow the Boltzmann relation even at subsonic but compressible flow conditions. In a related study but using equilibrium thermal conditions, it was shown that the isolator shock structure can develop a resonance to inflow perturbations that can vastly increase the pseudoshock spatial oscillations. These results verify that isolator flow is a complex nonlinear process and clearly demonstrate that the design of scramjets needs to include the effect of thermal nonequilibrium. To begin addressing this process, reduced-order models in the form of a flux-conserved one-dimensional formulation for estimating pseudoshock length was developed for thermal equilibrium conditions.

CHAPTER I

Introduction

1.1 Dual-mode scramjet engine

1.1.1 Scramjet development

Supersonic aircraft have a special place in the aerospace world due to their transformative potential: the ability to travel at speeds greater than that of sound (Mach number greater than 1) will vastly alter the global movement of people and goods, significantly impacting the scope of civilization. A typical example is to be able to cross the Atlantic ocean under an hour. At the heart of such high-speed aircraft is the dual-mode scramjet engine - supersonic combustion ramjet engine - (DMSJ) which processes fuel and air to generate propulsive thrust required for hypersonic flights (Mach number M greater than 5).

The ramjet engine was theorized as early as 1913 by René Lorin and follows the Brayton thermodynamic cycle. In internal combustion engines, the piston motion creates the compression. In conventional airbreathing engines such as turbojets, a co-axial turbine spinning at high velocity around a shaft compresses the air to a ratio of up to 15 times the inlet pressure. In ramjets, the flow is naturally fluid-mechanically compressed by the vehicle's own high speed. Of course, this requires the vehicle to possess another means of propulsion until the fluid-mechanical compression becomes high enough to start-up the ramjet. Once initiated, this means of propulsion becomes much more efficient than a turbojet. Indeed,

the turbojet needs to dispense part of the propulsive force to activate the turbine shaft. High-speed flow can also damage the turbine fans, while the absence of moving turbomachinery in a ramjet makes it maintenance-friendly. Also, the fluid-mechanical compression scales with the square of the flight Mach number and can be much higher than that of a turbojet. Lastly, the fluid-mechanical compression also increases the airflow temperature up to auto-ignition levels which removes the need for an igniter device.

It seems at first view that the ramjet engine possesses many advantages. However, it requires to first reach approximately Mach 3 to become more efficient than a turbojet with afterburner. Furthermore, its efficiency also decays for flight speeds beyond Mach 6 for the following reason. The core concept of the ramjet is to bring the incoming supersonic flow down to subsonic speed through a series of shock waves, thereby heating the flow up to an auto-ignition temperature and pressure. However, at very high hypersonic speeds the temperature recovered by slowing the flow to subsonic speed becomes so large that it would damage the engine and even start to dissociate nitrogen N_2, which would greatly reducing the burning efficiency. For example, a Mach 10.0 ramjet flight at 30 km altitude would bring the flow up to 4000 K by the combustor entrance. It is therefore much more efficient to progressively reduce the compression ratio by adapting the shockwaves structure, and let the internal flow remain supersonic throughout the engine. In such mode, the airflow enters the combustor and burns while at supersonic speeds. When operating in supersonic-combustion mode, the engine is called a scramjet. Ideally, the engine should be able to transition between ramjet and scramjet to increase its operational range. Such an engine is called a DMSJ and was patented by Billig based on his Ph.D. dissertation work in 1964 [32] (pp.365-367). His original design permitted on paper a flight speed of up to Mach 10. He later theorized that a scramjet could fly up to Mach 28 [10] although structural and thermal load limits would probably be reached even at lower Mach numbers. A sketch of a DMSJ engine is presented in Fig 1.1. As the incoming airflow enters the engine, it crosses a few oblique shocks. The structure of these external shocks depends on the vehicle angle of attack

and geometry. The flow is then deflected into the engine by another oblique shock. The flow then enters an isolating duct, which shields the combustor from intake instabilities called the isolator. Large scale shock turbulence interactions in the boundary layer (STBLI) occur within the isolator, forming a complex structure called a shock train which decelerates the airflow and increases both its pressure and temperature. The engine operates in ramjet mode when the shock train decelerates the flow to subsonic speeds. Conversely, the engine operates in scramjet mode when the flow remains supersonic. A divergent nozzle downstream of the combustor converts the high internal enthalpy of the burnt gas into kinetic energy.

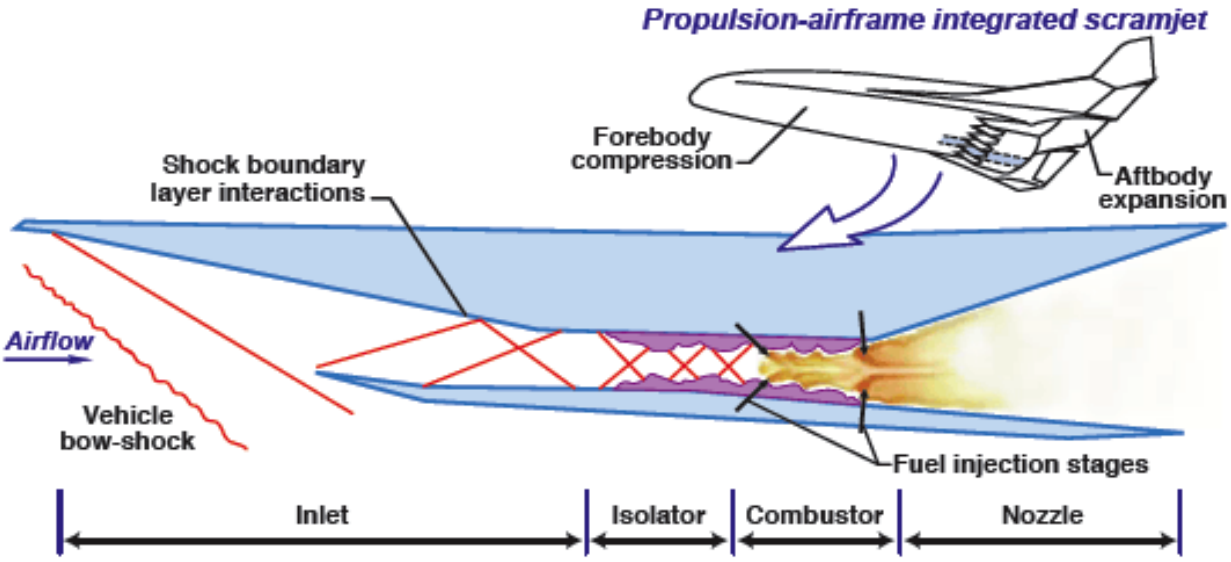

Figure 1.1: Sketch of a dual-mode scramjet engine [credit: NASA-LARC].

A propulsion performance diagram for various engines is shown in Fig. 1.2 for hydrogen combustion. The specific impulse index ISP is a ratio between the thrust generated by a kilogram of propellant and its weight and has a unit of seconds. Rockets can operate at any speed contrary to the other engines shown in the diagram. However, as they need to carry both fuel and oxidizer, the extra weight lowers their ISP: air-breathing engines are more efficient in that sense. A DMSJ engine would, therefore, fill the gap between current

low-speed high-ISP turbojets and high-speed low-ISP rockets for atmospheric travel.

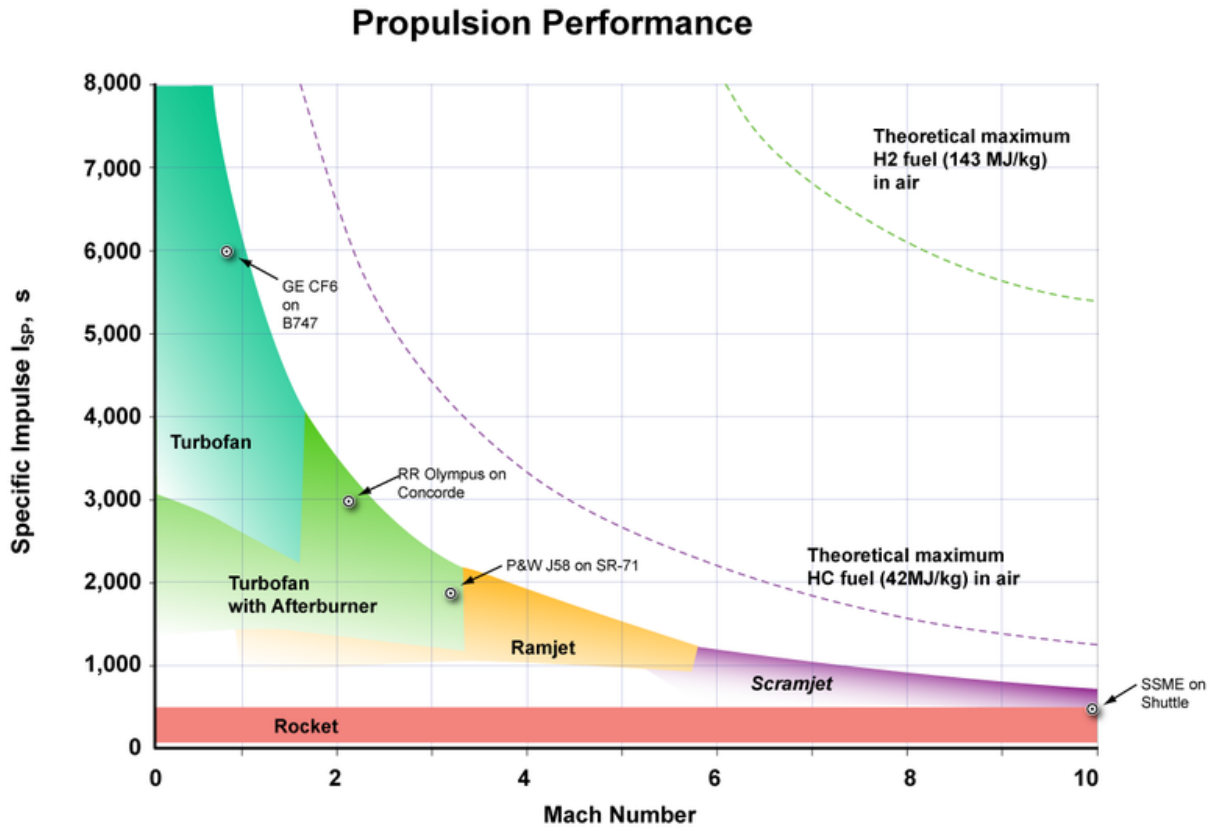

Figure 1.2: Specific impulse ratio for various propulsion engines [credit: Wikipedia].

Since the scramjet early development stage in the 70s, many successful tests have been performed. The first successful airbreathing hypersonic flight happened in the Soviet Union in 1991, using a hydrogen-fueled scramjet atop a rocket developed by the Baranov Central Institute of Aviation Motor Development. By the end of the century, a few other demonstrators flew up to Mach 6.7 for up to one minute of flight time [32, 87]. Subsequent programs such as the Australian HyShot [117] and NASA Hyper-X [43, 3] successfully flew self-propelled demonstrators. The more recent JP7-fueled X-51a WaveRider vehicle (Hyper-X program) managed to steadily fly over Mach 5.0 for 3 minutes, which is the longest hypersonic flight on public record [43]. The WaveRider was dropped at high altitude from a B-52 bomber, accelerated to Mach 4.8 by a solid rocket booster, which then separated before the WaveRider's

scramjet engine start-up. All these experiments prove that scramjets could one day provide steady propulsion for hypersonic transportation. To this day, however, ram/scramjet technology has only been successfully integrated into missiles.

A potentially groundbreaking application of the DMSJ engine is the development of Single-Stage-To-Orbit (SSTO) vehicles. Reaction Engines Ltd. has been developing an engine called Sabre which would operate in several mode during the same flight. It would take-off as a turbo-jet, and progressively transition into a ramjet around Mach 2.5, then into a scramjet around Mach 6. The rarefaction of O_2 at high altitude would eventually shut down the airbreathing mode. The intake would then close and the engine would transition into a rocket. The purpose of the initial airbreathing mode is to liquefy part of the ingested oxygen, store it and use it for the upcoming rocket mode. This allows the vehicle to save a considerable amount of weight at take-off contrary to all current space rockets. A sketch of the engine is shown in Fig. 1.3. Sabre would propel a large SSTO vehicle named Skylon designed for space travel and satellite deployment: it would drastically transform the space market. The engine development has to overcome 3 main difficulties to become fully operational. First, after a successful reentry, the vehicle would probably not be able to shortly take-off for another voyage/satellite deployment. The US space shuttle's heat shield required considerable maintenance after each flight as it would be damaged during the atmospheric reentry. Second, the O_2-liquefaction process occurs after enough heat has been taken from the hot, compressed incoming airflow. Yet, the airflow residence time within the engine will be on the order of a millisecond when operating in ram/scramjet mode. An extremely fast cooling technology is, therefore, required. Reaction Engines Ltd. claims to have successfully designed a novel heat exchanger which fulfill all these conditions, with tests beginning in 2018. Lastly, this hybrid engine will operate over a wide range of flight Mach numbers and altitudes. Hence, it requires to carefully design moving parts in order to continuously drive and contain the shock train structure within the isolator while in ram/scramjet mode.

This last difficulty is present in any DMSJ, and is particularly critical as losing the

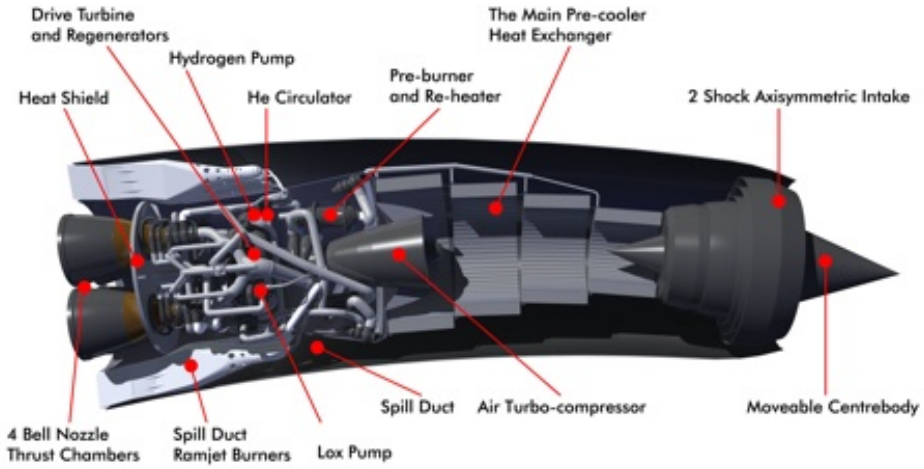

Figure 1.3: Sketch of a Sabre engine [credit: Reaction Engines Ltd].

compression stage would lead to a catastrophic in-flight engine shutdown. This risk is further discussed below.

1.1.2 Isolator unstart

The ability of the engine to burn fuel directly depends on the shock train capacity to provide the target pressure and temperature inside the combustor. Conversely, stable propulsion ensures that the vehicle speed remains high enough to permit the formation of a shock train inside the isolator. Hence, a vicious circle can be triggered if either the compression or propulsive stages fail. In such case, an abnormal pressure ratio forms between the isolator inlet and outlet which progressively dislodges the shock train from the isolator. Once the shock train is swept upstream of the isolator, a normal shock forms in front of the inlet as seen in Fig 1.4. The mass flow rate into the isolator is significantly reduced, and the combustor loses propulsive power due to this reduction in air flow. Such engine failure is called inlet/isolator unstart, and will be more simply referred to as unstart.

Coincidentally, the displacement of shocks around the engine also causes considerable transient mechanical loading. Notably, the normal shock that appears in front of the isolator

inlet is highly unsteady. Its unsteadiness results from its interaction with the intake bow shock and with the unstarted isolator backflow spillage. This oscillation is known as "big buzz" [122] and can lead to significant mechanical loads on the isolator inlet.

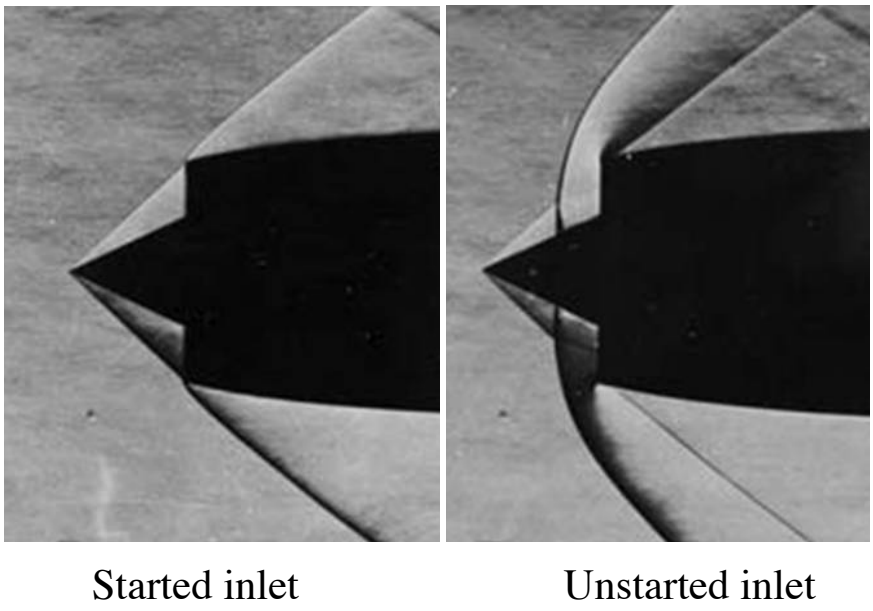

Figure 1.4: Schlieren images of a (left) started and (right) unstarted inlet on the SR-71 [credit: NASA Glenn Research Center].

Unstart is, therefore, a catastrophic event that can shutdown and damage the engine. It is a critical design condition for developing robust hypersonic vehicles. As long as the engine remains at risk of unstart, hypersonic vehicles will remain unstable, unsafe. For instance, the longest hypersonic flight on record, the X-51 Waverider, was cut short by unstart [95]. Due to its critical importance, unstart has been extensively studied, and a review of both experimental and computational works on isolator unstart will be presented in Sec. 1.2. Before this review, the mechanics triggering this event are presented.

First, the isolator shock train is sensitive to changes in inflow conditions. For instance, the far-field pressure will steadily decrease with altitude, or the vehicle acceleration will change the flight Mach number. Also, any vehicle maneuver will change the angle of attack and the intake shock pattern, affecting the thermodynamic state of the inflow to the isolator. Figure 1.5 from presents real data from the HyShot flight [117]: it shows how the angle of

attack oscillates as the vehicle tries to remain still at hypersonic speeds. In all these cases, the pressure difference between the isolator inlet and outlet is modified and the shock train position/structure adapts to it. If the isolator geometry cannot accommodate these changes (being too short for instance), unstart will eventually occur. Note that such inflow-triggered unstart could be prevented by adjusting the vehicle inlet geometry in order to change the oblique shock structures upstream of the isolator (as seen in Fig. 1.1). For instance, movable centerbodies (as seen in Figs. 1.3 and 1.4) prevent the intake shock from entering the engine, and can be displaced further outside when the shock becomes shallower with increased Mach number. This feature has been implemented on supersonic turbojets such as the American F-104, the Russian Mig-21 and the French Mirage-III as early as the 1950's. Likewise, real-time adjustment of the isolator inlet Mach number, pressure and boundary layer properties can prevent inflow-triggered unstart [125]. This requires state-of-the-art shock train prediction tools to determine the ideal inflow state based on the isolator outlet state. Inflow-triggered unstarts are "explicit" in the following sense: the instability does not reside within the engine but originates from the bulk flight conditions and are the easiest to address.

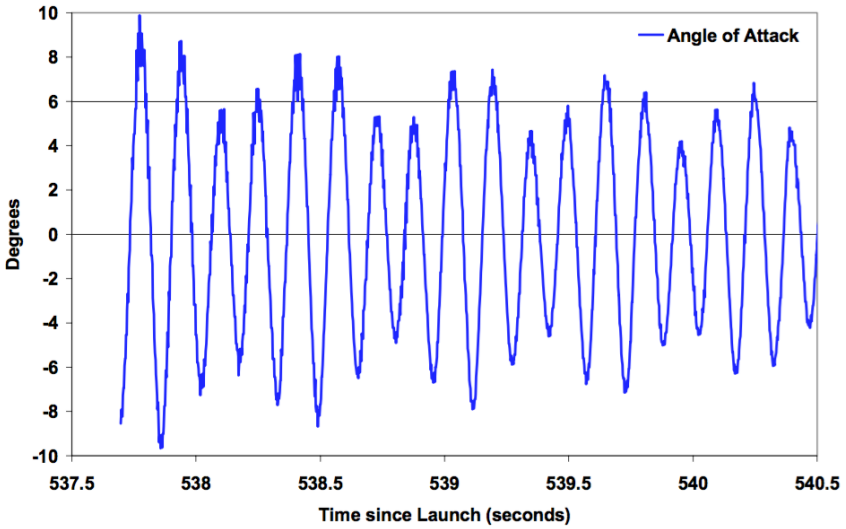

Figure 1.5: Variation in time of the HyShot experimental flight angle of attack whilst in scramjet mode from Smart [117].

On the other hand, the most complex kind of unstart is triggered by flow-choking inside the engine. Flow-choking is the evolution of the bulk flow Mach number towards unity

due to either friction (in a Fanno flow) or heat release (in a Rayleigh flow). The flow can also choke due to a change of the cross-sectional area, as in a Laval nozzle. Internal flows are referred to as choked when locally the Mach number reaches a sonic state. In the context of scramjets, the flow inside the engine is supersonic: flow-choking reduces the Mach number. This deceleration induces a pressure rise which propagates upstream through the subsonic boundary layer in the isolator. If strong enough, this adverse gradient can further separate the boundary layer, generating more blockage and building up the overpressure. If the pressure wave reaches the inlet, flow spillage and unstart happen. An example of such unstart is seen in Fig. 1.6 reproduced from Koo [68]. The figure shows how the boundary layer separates as the pressure wave convects upstream, resulting in a mass flow rate drop. The recent review paper of Im and Do [73] offers an overview of the causes of choking-triggered unstart. The main cause is heat release which leads to a large pressure rise in the combustor through thermal choking. The second cause of choking is through mass addition. The fuel mass flow rate increases the flow density while, at the same time, turbulent mixing decelerates the airflow, both of which increase the local pressure. Lastly, flow blockage is another cause of local overpressure. It happens when the subsonic turbulent boundary layer grows (or separates) so much that it decelerates the bulk flow. Note that the higher the internal flow Mach number is, the higher the overpressure has to be to trigger unstart. Hence, higher Mach flights regime are relatively immune to choking-triggered unstart, while slower scramjet flights are more at risk of a sudden (and unwanted) transition to ramjet mode.

1.1.3 Oblique and normal shock trains

The shock train has been demonstrated to be a key component of scramjet engines. In the particular case of DMSJ, its structure drastically changes during the transition between ramjet/scramjet modes: this maneuver needs to be carefully handled. As a reminder, this transition marks the limit between subsonic and supersonic combustion. Around this tran-

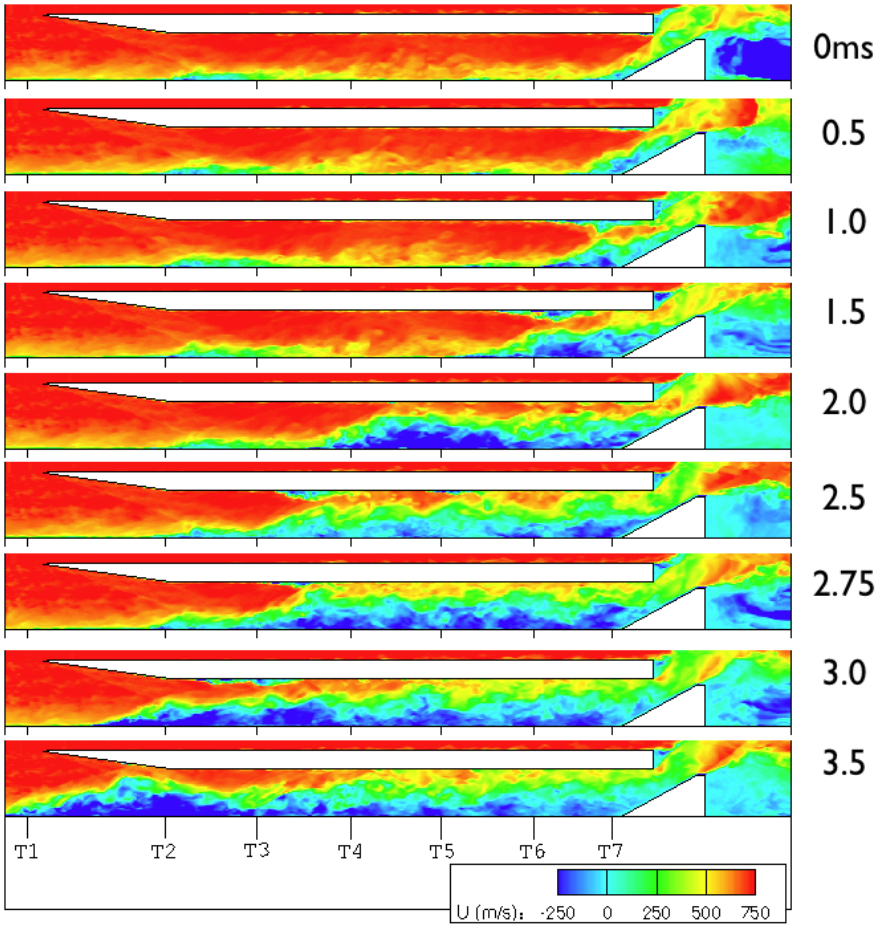

Figure 1.6: Streamwise velocity contours over time for a choked isolator from Koo [68].

sition (flight Mach ≈ 6.0), the shock train evolves from a normal shock train (NST) to an oblique shock train (OST) [85] as illustrated in Fig. 1.7. The structure of a normal shock train is very complex and comprises several cells (there are six cells in the bottom figure example). Each cell is composed of a compression wave followed by a weaker expansion: the cross-sectional pressure, therefore, rises through each cell. The flow decelerates coincidentally, which decreases the sonic core area. Hence the shock cells sizes progressively diminish too. The NST leading shock often presents a lambda-like shape: the centerline normal-like shock (*i.e.* normal to the streamwise direction) is attached to the boundary layers by lambda-like feet. In such case, it is referred to as a lambda-shock. The wall adverse pressure gradient is usually strong enough below the first lambda-shocks to separate the turbulent boundary

layer. An OST can also trigger a recirculation bubble, although its pressure growth rate is more linear and weaker than for an NST due to the angling of the shocks. Schlieren images of the leading portion of normal and oblique shock trains are shown in Fig. 1.8, revealing their particular characteristic shapes. Oblique shock trains can also appear at lower Mach number when the inflow confinement ratio (defined as the inflow boundary layer over the half-channel height) is large enough to shrink the centerline normal-like portion [52, 33].

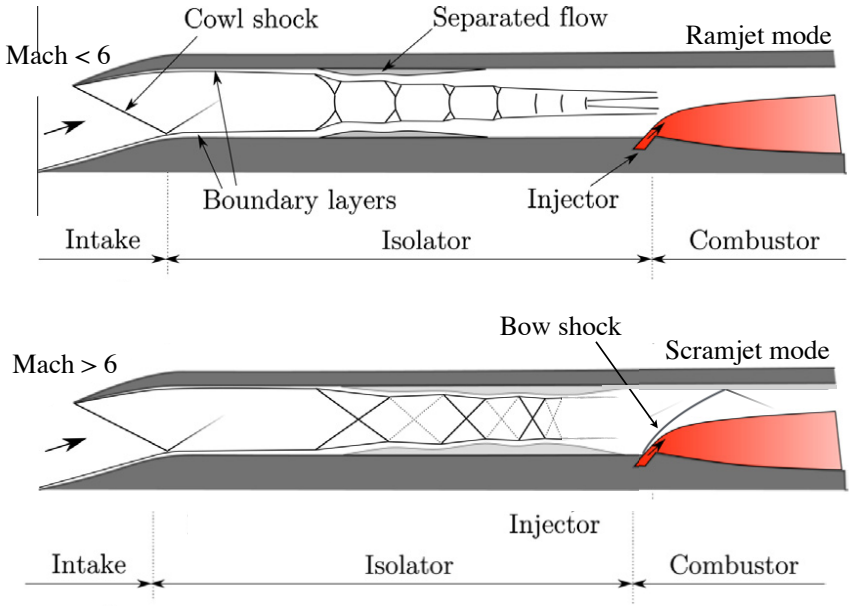

Figure 1.7: Illustration of the differences between ramjet (op) and scramjet (bottom) modes adapted from Laurence *et al.* [77].

The whole pressure growth region inside the isolator is referred to as a pseudoshock [85], since a fraction of a normal shock pressure is recovered over space. This terminology is valid for both OST and NST. The pseudoshock includes a post-shock train turbulent mixing region where pressure increases through friction. Throughout this dissertation, the term "shock train" will explicitly refer to the shock structure only. The term "pseudoshock" will instead refer both to the pressure growth process, and to the observable structure composed of both shock train and the downstream fully-developed turbulent mixing region.

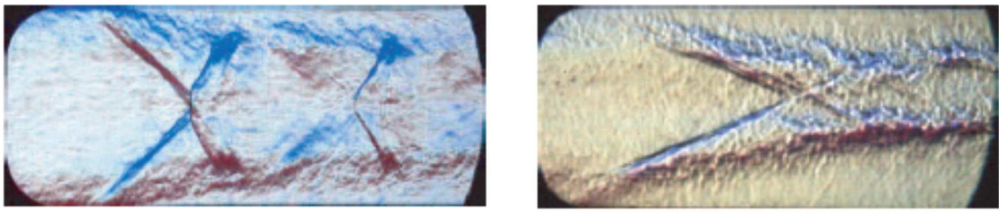

Figure 1.8: Schlieren images of the leading portion of (left) a Mach 2.0 normal shock train and (right) a Mach 4.0 oblique shock train from Sugiyama *et al.* [119]. Blue/red indicates a negative/positive vertical speed.

1.2 Previous studies on dual-mode scramjet isolators

Isolators have been the focus of many studies aimed at improving our understanding of pseudoshock physics in order to tackle the unstart problem. A detailed review of previous pseudoshock studies is now presented.

1.2.1 Isolators experiments

A pseudoshock can be created in laboratory-scale experiments by back-pressuring a supersonic duct [54]. Experimental studies have used pressure measurements, laser Doppler velocimetry (LDV), shadowgraphs, particle image velocimetry (PIV) and Schlieren images to study the shock train structure. For instance, Waltrup and Billig [136] analyzed pressure traces to propose an empirical relation between shock train length, wall pressure, and upstream flow conditions. Carroll and Dutton [16, 17] have studied the evolution of the shock train shape when varying inflow conditions using Schlieren imaging. Arai *et al.* used LDV to measure the centerline flow speed decay through an NST. Hunt *et al.* [52] quantified the size of the recirculation bubble and its displacement using PIV in an NST. Visualization techniques have become more accurate over time, as can be seen in Fig. 1.9 which presents a panel of normal shock trains at different inflow Mach number and confinement ratio.

A review by Matsuo *et al.* [85] on many pseudoshock experiments highlights the following dependence on the inflow Mach number. At low supersonic speeds ($M < 1.2$), a normal shock transitions the flow to a subsonic state. This normal shock becomes increasingly curved

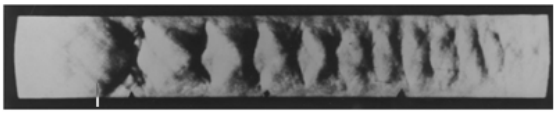

Mach 1.7 shock train from Ikui et. al. (1969)

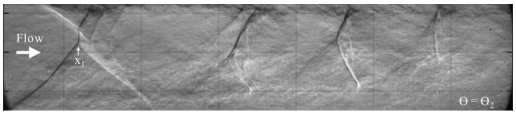

Mach 2,0 shock train from Hunt et. al. (2017)

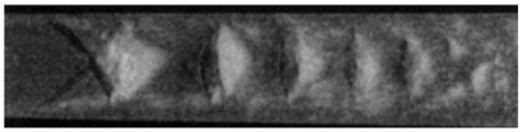

Mach 1.75 shock train from Matsuo et. al. (1993)

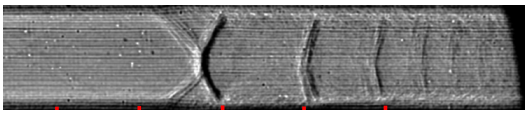

Mach 1.8 shock train from Hutchins et. al. (2014)

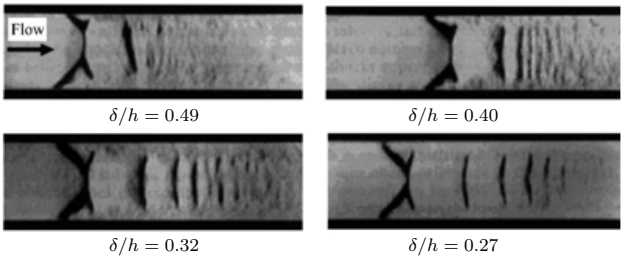

Mach 1.6 shock trains for various inlet boundary layer heights from Matsuo et. al. (1993)

Figure 1.9: Normal shock trains visualized from shadowgraph and Schlieren imaging in various experiments.

with the increase in flow speed, and at velocities greater than $M = 1.4$, the single normal shock bifurcates and forms a shock train. As the Mach number increases, the pseudoshock length (PSL) and pressure rise ratio (PRR) increase. As the Mach number increases the lambda-shock feet increase in size and their angle becomes shallower: this has the effect of pushing back and shrinking the normal-like portion. As a normal shock compresses more than an oblique shock, this decreases the pressure growth rate. In between Mach 2.0 and 2.5, depending on the inlet boundary layer height, the normal-like portion disappears and the NST transitions into an OST [52].

The incoming boundary layer properties are also known to have an impact on the pseudoshock structure. For instance, Carroll and Dutton [16] have shown that as the confinement ratio increases, both the number of shocks and the spacing between the shocks increases. At the same time, the bifurcation associated with the leading shock reaches more towards the center of the flow with an increase in confinement ratio. Further, the effect of confinement

ratio decreases as the Mach number increases.

More recent measurements [13, 20, 119, 52] show that the shock structures are inherently unsteady, with the oscillation amplitude and frequency increasing with inflow Mach number. Hunt *et al* [52] have shown that upstream-traveling acoustic waves through the subsonic boundary layer were interacting with the recirculation bubbles, exciting particular oscillation modes.

Other studies [13, 53, 125, 63, 113, 110] have focused on the physics of the unstart process, where the shock train is completely dislodged by an unsupportable pressure gradient across the isolator section. At fixed inflow conditions, increasing the back pressure results in dangerously pushing the pseudoshock further upstream. Such response is seen in Fig. 1.10 (left): as the back pressure increases through downstream flow blockage the leading shock is pushed upstream. Figure 1.10 (right) shows similar response on pseudoshocks wall pressure profiles. It appears the pseudoshock length also increases to match the higher back pressure. Instabilities leading to unstart can be caused either by upstream (change of flight conditions) or downstream (unstable combustion) perturbations. In an experimental facility, the former is more practically studied. Typically, downstream perturbations have been mimicked by varying through time the isolator exit pressure through valve actuation [13, 53, 125, 51]. Klomparens *et al.* [63] have identified a hysteresis effect during the cyclic motion that causes the shock train to travel along different paths during the upstream and downstream parts of the cycle. Bruce and Babinsky [13] found that the shock oscillations induce a corresponding change of relative Mach number which changes both its shape and the wall pressure profile, depending on the direction of motion of the shock.

In a more realistic configuration, Fotia and Driscoll [41] performed a high-enthalpy experiment of a model DMSJ including the combustor. The isolator back pressure resulted from the combustor thermal choking as in an engine, instead of a mechanical blockage. They observed the evolution of the pseudoshock location and length as the fuel equivalence ratio changed. They showed that when it suddenly drops, the back pressure decreases which had

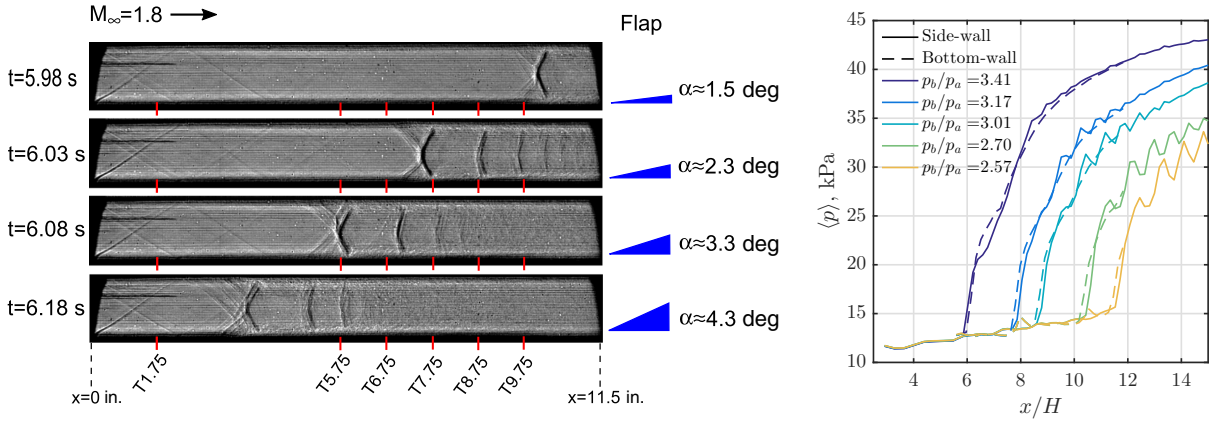

Figure 1.10: (Left) Impact of back pressure increase in a typical experimental facility shown from shadowgraph contours by Hutchins *et al.* [53]. (Right) Bottom and side wall static pressure contours for various back pressure from Hunt *et al.* [52].

the effect of transitioning to scramjet mode. Conversely, when in scramjet mode, a sudden increase of fuel mass flow rate would increase the back pressure through thermal choking and flow blockage, transitioning to ramjet mode. Such an unexpected transition could even unstart the isolator. Most interesting, they observed that pseudoshock low-frequency instabilities would propagate and excite the turbulent flame's same modes. This highlights the secondary purpose of the isolator: shield the combustor from any inlet instabilities to ensure stable combustion.

Understanding the sensitivity of shock trains to the near-wall flow is also useful for controlling the unstart process. In particular, perturbations to the boundary layers through actuation mechanisms can be used to delay unstart. For instance, Hutchins *et al.* [53] studied a Mach 1.8 channel flow, where both the inlet total pressure and the back pressure can be altered separately. This configuration was used to build a non-linear transfer function capable of predicting the time-dependent shock train location when subjected to both upstream and downstream pressure instabilities. Valdivia *et al.* [125] used the same experimental configuration to demonstrate that an active control of the shock train position in a situation of imminent unstart is possible. Using side-wall passive vortex injectors, an overpressure of 32% compared to the injector-free case was achieved without unstart. Similar boundary

layer modifications have been used to modify the shock train in other studies [29, 138]. For instance, Do *et al.* [29] studied unstart in a Mach 5 wind tunnel by impinging the flow with a wall-normal injector. It was found that symmetric, thin and laminar boundary layers were able to sustain this flow blockage longer than thick and turbulent boundary layers prone to detachment. These important results prove that anti-unstart mechanics can be designed and actuated, provided predictive tools can accurately determine the optimal pseudoshock length/compression rate at all time, and detect the onset of unstart.

1.2.2 Numerical simulations of isolator flow

In addition to these experiments, a number of computational simulations have also been performed to study isolators. Such simulations are essentially of two kinds. The first kind utilizes an inlet ramp to create an initial incident shock that is fixed in time [71, 8, 34, 118, 107]. This yields a steady shock train attached to the foot of the first reflected shock, and which is expected to be adequately described by inviscid theory. Of course, further downstream, the reflected shocks are weaker and are affected by the turbulent flow structure inside the isolator. Koo and Raman [71] used a large eddy simulation (LES) to simulate a Mach 5 supersonic inlet-isolator with unstart, which was caused by an increase in back pressure at the outlet. LES resolve the time-dependent Navier-Stokes equation on a grid which is too coarse to resolve the smallest turbulence lengthscales. Hence, sub-grid and near-wall turbulence models are used to account for their effects on the flow. Overall, they concluded that the LES approach, with relatively simple sub-grid and wall models, is able to capture the overall shock structure for both static and unstart cases. However, there was a significant difference in the timescales associated with unstart, where the LES predicted a faster upstream shock propagation speed compared to the experiments. Su *et al.* [118] simulated a ramp-based inlet of a vehicle flying at high altitude and at Mach 6 using a Reynolds-averaged numerical simulation (RANS). A RANS consists in resolving the time-averaged solution to the Navier-Stokes equations closed with a turbulence model. In Su *et*

al.'s work, a varying back pressure condition was applied at the outlet. It was observed that the shock train oscillation amplitude was the highest for the smallest frequency simulated and that increasing the dynamic pressure oscillation amplitude increased the corresponding wall pressure oscillation amplitude. Their use of a time-averaged method such as a RANS to study pseudoshock dynamics was, however, questionable.

The second kind of isolator simulations involves a normal shock train [81, 18, 126, 91, 21, 82, 59, 44, 31], which is more relevant to the DMSJ regime. Here, the initial shock bifurcation is caused by flow confinement: this requires either an outlet numerical back pressure condition or the inclusion of the combustor in the computation domain. Both RANS [81], LES [21, 91, 59, 126, 114] and hybrid models [44, 31] have been used. In general, time-resolved LES and hybrid RANS/LES approaches have been fairly successful in capturing experimental measurements, as opposed to RANS computations [92]. In particular, LES wall-modeled approaches or techniques that contain no special treatment for the shock-boundary layer interaction still predict the shock train structure reasonably well, although wall-modeling was found to slightly improve predictive accuracy [59]. Such studies demonstrated that boundary layer modification can alter shock train location. For instance, wall cooling reduced the distance between the shocks [59].

Edwards & Fulton used a hybrid RANS/LES solver to simulate full DMSJ engines including both the isolator and the combustor [44, 31] as seen in Fig. 1.11. The isolator flow is resolved with a RANS solver, and an LES solver resolves the combustor. This allowed them to bypass the need for an artificial numerical back pressure as the thermal choking in the combustor was naturally providing it. While the capacity of these numerical tools to simulate the whole engine is promising, the accuracy of the solution depends on the ability of the RANS to correctly predict the location and pressure rise of the shock train. Unfortunately, the RANS method is known to poorly resolve the shock train structure, whatever closure model is used. Indeed, turbulence closure models are not universal and heavily based on empirical correlations. Additionally, the RANS is known to be inaccurate when used to

simulate a pseudoshock nearing unstart [80]. This can be attributed to the acknowledged inability of RANS to correctly resolve the dynamics of recirculation bubbles [92]. This is particularly problematic when trying to use a RANS for research purposes. A comparative study between different models from Morgan *et al.* [92] is presented in Fig 1.12. Three RANS and LES models were used to simulate Sullins *et al.* [120] Mach 1.6 shock train experiment, resulting in vastly different solutions. The LES solution (top) matched the experimental wall pressure profile better than any RANS model. This indicates that the turbulence closure model has an important influence on STBLI, hence on the pseudoshock.

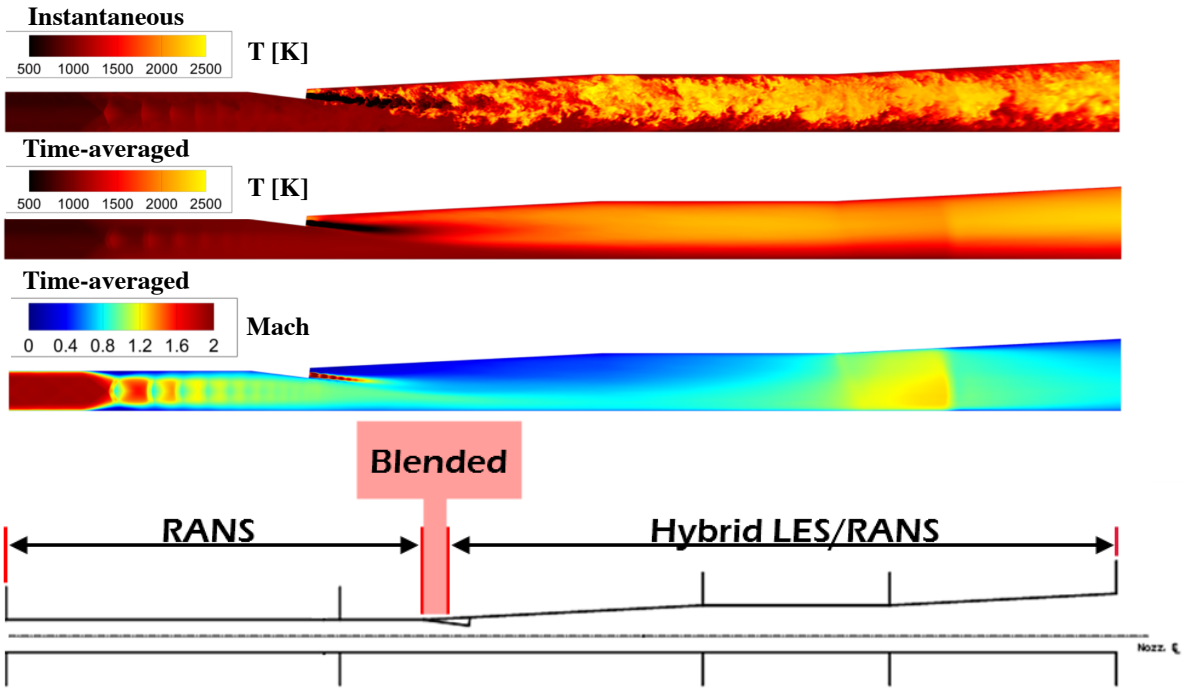

Figure 1.11: Hybrid RANS-LES simulation of a ramjet engine by Fulton *et al.* [44].

Overall, these experimental and computational studies highlight the key role of the inflow boundary layer in determining the pseudoshock structure and stability. Time-resolved simulations have proven to be able to resolve and study isolator flows, yet are too expensive to be used as practical design tools.

All these simulations, while using different numerical modeling, close the Navier-Stokes equations using the same thermally perfect gas (TPG) model. A brief presentation of this

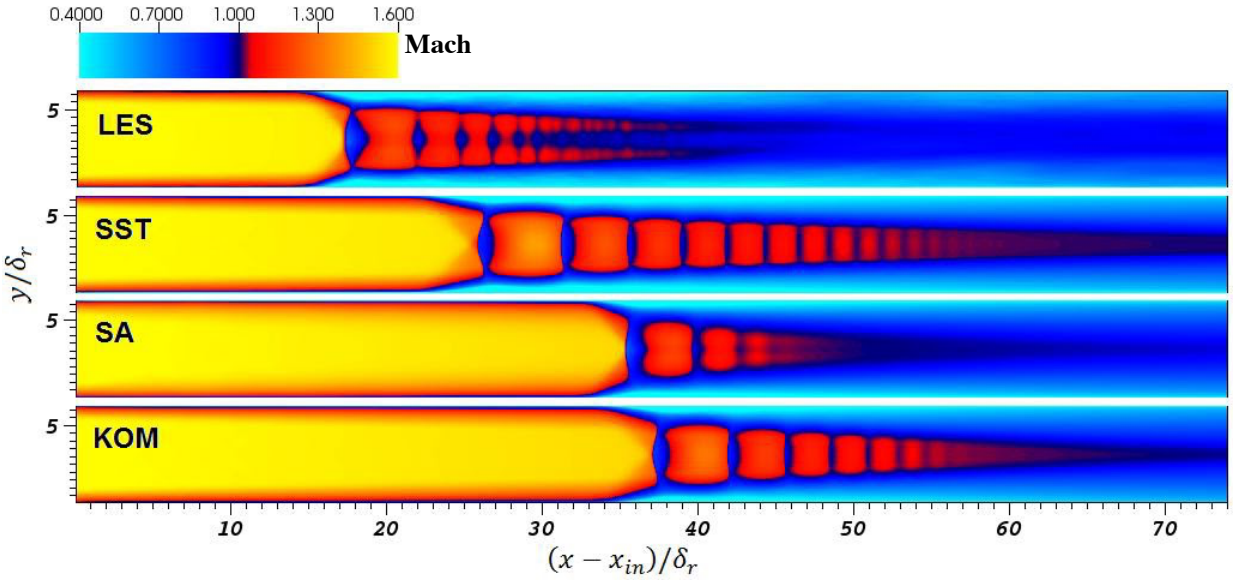

Figure 1.12: Comparison of time-averaged Mach number contours from simulations of Mach 1.6 shock trains using different numerical models from Morgan *et al.* [92].

thermodynamic model is given in the next section alongside a short presentation on statistical mechanics.

1.3 Thermodynamic nonequilibrium

A brief description of the concept of statistical mechanics and thermodynamic equilibrium/nonequilibrium is given in this section. The material presented in this section is derived from Vincenti and Kruger [127] (chapters I, II, IV, V, VII, VIII and IX).

1.3.1 Distribution of internal energy states

In this section, a gas is defined as a system formed by a fixed number of N molecules. These molecules interact through collision. The internal energy of a gas is the sum of all its molecules energies. In kinetic theory, the motions of each particle are analyzed to compute the gas energy and resolve macroscopic fluid dynamics. Instead, in statistical mechanics,

one is more interested in the distribution of the molecules quantized energy states. The core concept of quantum mechanics is wave-particle duality. If one wants to determine the energy of a particular molecule, the solution takes the form of a wave function Ψ, which leads to Heisenberg uncertainty principle. Based on 5 fundamental postulates of quantum mechanics pertaining to the operators of Ψ (see chapter IV in [127]), Ψ is a solution of the Schrodinger equation (Eq. 1.1). This equation essentially balances the wave-particle kinetic and potential energies. It is known from quantum mechanics that acceptable solutions of the Schrodinger equation occur for discrete eigenvalues. For instance, a particle in rectilinear displacement inside a closed box of length L and no potential field $V(\mathbf{r})$ possess a translational energy ϵ_t shown in Eq. 1.2. In this equation, integers n_1, n_2 and n_3 are the translational quantum numbers in the 3 spatial directions. Likewise, a diatomic molecule also possesses rotational and vibrational quantum numbers n_r and n_v which characterize its internal rotational and vibrational energy and are also solutions of Eq. 1.1. Every quantum number is associated with a particular state which corresponds to a unique energy. The quantum numbers of all the particles inside of a gas form a distribution of energy states. These distributions (one per energy mode, translational, rotational and vibrational) form the link between the molecular scale to macroscopic thermodynamics. Excitation of electronic states higher than the ground state (gas ionization) will not be considered in this dissertation.

$$\frac{\hbar^2}{2m}\nabla^2\Psi + V(\mathbf{r})\Psi = -i\hbar\frac{\partial\Psi}{\partial t} \tag{1.1}$$

$$\epsilon_t(n_1, n_2, n_3) = \frac{\pi^2\hbar^2}{2mL^2}\left(n_1^2 + n_2^2 + n_3^2\right) \tag{1.2}$$

The definition of entropy S, as a measure of the degree of molecular randomness and freedom of a system of N particles, connects the molecular and macroscopic scales through Eq. 1.3:

$$S = k_b log(\Omega), \tag{1.3}$$

where Ω measures the number of possible quantum numbers arrangements across the allowed quantized energy states yielding the same integrated energy. k_b is the Boltzmann constant. Indeed, as the energy of a mode increases, higher states are more likely to become populated. A micro-state $W(C_j, N_j)$ is defined as a set of N_j molecules distributed across all C_j states. The set must be coherent: the energy it contains must sum up to the bulk energy of the system. The sum of possible micro-states W form a macro-state, and the largest macro-state $W_{max}(C_j, N_j^*)$ determines Ω. Analytical solutions for Ω exist, and depend on some arrangement rules. The differences resulting from either Bose-Einstein and Fermi-Dirac statistics will not be detailed here, and the reader is encouraged to read Vincenti [127] (fourth chapter). At energies high enough such that there exist more possible states than molecules (*i.e.* $N_j << C_j$ always the case in practical applications), known as the Boltzmann limit, the solution maximizing entropy can be shown to converge towards:

$$log(\Omega) = log(W_{max}) = \sum_j \left[1 + log\left(\frac{C_j}{N_j^*}\right)\right] = N\left[1 + log\left(\frac{1}{N}\sum_j C_j \exp(-\frac{\epsilon_j}{k_b T})\right)\right] + \frac{E}{k_b T}, \tag{1.4}$$

and the gas particles are distributed across this special macro-state such as:

$$\frac{N_i}{N} = \frac{g_i \exp(-\frac{\epsilon_i}{k_b T})}{\sum_j g_j \exp(-\frac{\epsilon_j}{k_b T})}. \tag{1.5}$$

Equation 1.5 corresponds to the Boltzmann states distribution for any state-level i. g_j the degeneracy of level j, and N_i the number of molecules in state i (having quantum number i). The denominator serves as a normalization factor and is called a partition function. There exists a partition function for the translational, rotational and vibrational energy modes called Q_t, Q_r and Q_v. Their product $Q_t \times Q_r \times Q_v$ forms the gas partition function Q.

1.3.2 Macroscopic thermodynamic properties

All the macroscopic thermodynamic properties are derived from the partition function Q. We know from classical thermodynamics that $dS = \frac{dE}{T} + \frac{P}{T}dV - \frac{\tilde{\mu}}{T}dN$. By using Eq. 1.5 with Eq. 1.3 and Eq. 1.4, we obtain:

$$S = Nk_b\left[log\left(\frac{Q}{N}\right) + 1\right] + \frac{E}{T} \tag{1.6}$$

The next step consists in using Gibbs free energy $F = E - TS$. Hence, F is expressed as a function of Q:

$$F = E - TS = -Nk_bT\left[log\left(\frac{Q}{N}\right) + 1\right] \tag{1.7}$$

Additionally, $dF = dE - TdS - SdT = -SdT - PdV + \tilde{\mu}dN$. Thus:

$$\begin{aligned} S &= -\left(\frac{\partial F}{\partial T}\right)_{V,N} \\ P &= -\left(\frac{\partial F}{\partial V}\right)_{T,N} \\ \tilde{\mu} &= -\left(\frac{\partial F}{\partial N}\right)_{V,T} \\ E &= -T^2\left[\frac{\partial F/T}{\partial T}\right]_{V,N}. \end{aligned} \tag{1.8}$$

Finally, Eq. 1.7 can be inserted into Eqns. 1.8 to express all these thermodynamics variable in function of Q:

$$
\begin{aligned}
S &= Nk_b\left[1 + log\left(\frac{Q}{N}\right)T\frac{\partial log(Q)}{\partial T}\right] + \frac{E}{T} \\
P &= Nk_bT\frac{\partial log(Q)}{\partial V} \\
\tilde{\mu} &= -k_bTlog\left(\frac{Q}{N}\right) \\
E &= Nk_bT^2\frac{\partial log(Q)}{\partial T}.
\end{aligned}
\tag{1.9}
$$

As all the macroscopic thermodynamic properties are determined by the molecular partition functions, it is possible to evaluate these properties for each separate energy mode. This permits to evaluate how much pressure, entropy or internal energy comes from each translational, rotational and vibrational molecular motions.

The partition function for the translational energy can be evaluated from Eq. 1.2:

$$
Q_t = \sum_{n_i} \exp\left[-\frac{n_i^2}{L}\frac{\hbar^2}{8mk_bT}\right] \approx \int_{n_i=0}^{\infty} \exp\left[-\frac{n_i^2}{L}\frac{\hbar^2}{8mk_bT}\right] = V\left(\frac{mk_bT}{2\pi\hbar^2}\right)^{\frac{3}{2}} \tag{1.10}
$$

where the continuous formulation is a good approximation given the very low energy increment in between levels. The partition functions for the rotational and vibrational energy Q_r and Q_v require modeling the energy levels ϵ_r and ϵ_v respectively. A simple model for ϵ_r is the rigid rotor, $\epsilon_r(J) = 2k_b\theta_rJ(J+1)$, where θ_r is the species rotational activation temperature and J the rotational quantum number. The degeneracy g_J for the rotational energy equals $J(J+1)$. Q_r is presented in Eq. 1.11 for a symmetric molecule such as N_2. A model for ϵ_v is the simplified harmonic oscillator, $\epsilon_v(v) = vk_b\theta_v$, where θ_v is the species vibrational activation temperature and v the vibrational quantum number. The degeneracy g_v for the rotational energy equals 1 for all levels. Q_v is presented in Eq. 1.12 with a valid approximation when $T < \theta_v$. These two models neglect the coupling between these two energies.

$$Q_r = \sum_J (2J+1)\exp\left(-\frac{\theta_r}{T}J(J+1)\right) \approx \int_{n_i=0}^{\infty} (2J+1)\exp\left(-\frac{\theta_r}{T}J(J+1)\right)dJ = \frac{T}{2\theta_r} \quad (1.11)$$

$$Q_v = \sum_v \exp\left(-v\frac{\theta_v}{T}\right) \approx \frac{1}{1-\exp\left(-\theta_v/T\right)} \quad (1.12)$$

It is now possible to decompose, for instance, pressure by evaluating the partition functions in Eqns. 1.9. In kinetic theory, the pressure is defined as the molecular momentum of particles colliding with an arbitrary surface. The resulting translational pressure P_t can be shown to be equal to $P_t = \frac{Nk_bT}{V}$, which recovers the ideal gas law. The pressures obtained from the molecular internal rotational and vibrational modes equal zero. This result shows that kinetic theory and statistical mechanics are consistent with one another.

Using Q_t, Q_r and Q_v with Eqns. 1.9, the following decomposition of the specific internal energy is derived:

$$\begin{aligned} e = RT^2\frac{\partial log(Q_tQ_rQ_v)}{\partial T} &= RT^2\frac{\partial log(Q_t)}{\partial T} + RT^2\frac{\partial log(Q_r)}{\partial T} + RT^2\frac{\partial log(Q_v)}{\partial T} \\ &= \frac{3}{2}RT + RT + RT^2\frac{\partial log(Q_v)}{\partial T} \\ &= e_t + e_r + e_v \end{aligned} \quad (1.13)$$

This expression indicates that the translational and rotational modes specific heat capacity at constant volume $(c_v)_t$ and $(c_v)_r$ equals 3R/2 and R respectively. This is once again consistent with classical thermodynamic, and the correct ratio $\gamma = 1.4$ is recovered for O_2 and N_2 gas at temperatures $\theta_r < T << \theta_v$. The vibrational energy and its corresponding $(c_v)_v$ are instead dependent on the temperature:

$$e_v = RT^2 \frac{\partial}{\partial T}\left(- log\left[1 - \exp\left(- \frac{\theta_v}{T}\right)\right]\right) = \frac{R\theta_v}{\exp\left(\frac{\theta_v}{T} - 1\right)} \tag{1.14}$$

Hence, the vibrational energy specific heat at constant volume is computed as:

$$(c_v)_v = \left(\frac{\partial e_v}{\partial T}\right)_V = R\left[\frac{\theta_v/T}{sinh\left(\frac{\theta_v}{2T}\right)}\right]^2 \tag{1.15}$$

Therefore, the vibrational energy is activated as temperature increases and closes with the species θ_v. When $T << \theta_v$, e_v tends towards zero, and when $T >> \theta_v$, e_v tends towards RT such that its $(c_v)_v$ progressively increases to match $(c_v)_r$. When the vibrational mode is fully excited ($(c_v)_v = R$) the heat specific ratio γ equals 1.28. Note that θ_r equals 2.1 and 2.9 K for O_2 and N_2, while θ_v equals 2270 and 3390 K respectively. This means that the activation of the vibrational molecular motion requires much more energy than for the rotational, let alone the translational, molecular motion. By "activation of vibrational mode", it is meant the increase of the vibrational energy, or from a quantum point of view the population increase of the high-energy states. The effect of such activation as temperature increases on macroscopic thermodynamics is shown in Fig. 1.13 for air. Neglecting this phenomenon results in having a constant c_v and γ, which is also known as the calorically perfect gas (CPG) model. On the contrary, resolving the increase of vibrational energy results in a varying c_v and γ such that the energy must be computed through an integral instead of a simple product. It results in a higher energy storage capacity at the molecular level, by allowing more quantized states to be populated. Incidentally, this increases entropy. This more expensive model is called the thermally perfect gas model. In both cases, the world "perfect" refers to the use of the ideal gas law which is considered valid throughout the dissertation (Van Der Walls interactions are neglected).

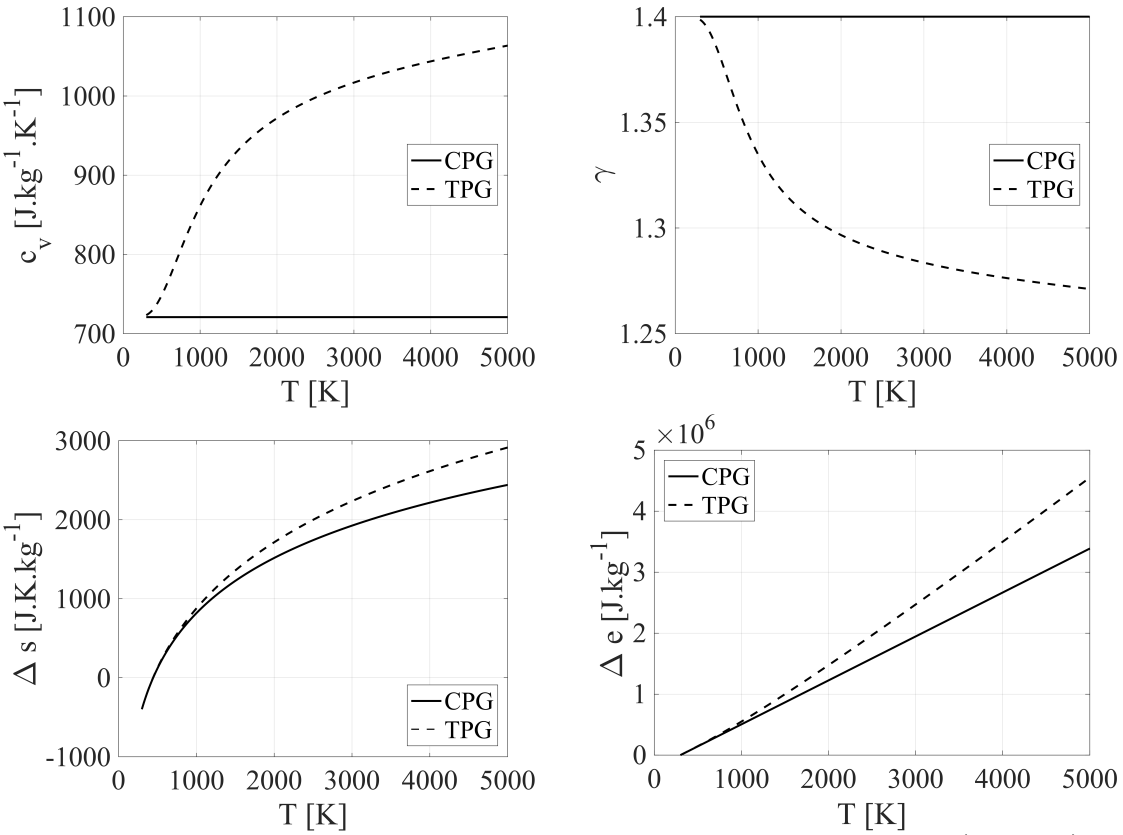

Figure 1.13: Effect of the activation of the vibrational energy mode on (top left) specific heat at constant volume, (top right) specific heat ratio, (bottom left) specific entropy and (bottom right) specific internal energy as temperature increases.

1.3.3 Vibrational nonequilibrium

The previous section showed that when the temperature of a polyatomic gas increases, the activation of the molecular vibrational energy affects its thermodynamic state. The increase in temperature means the direct increase of random molecular motion, hence translational energy. Collisions between molecules permit the exchange of energy in between the translational, the rotational and the vibrational modes. Higher vibrational energy levels become more populated through molecular collisions until the thermodynamic equilibrium state is reached. This energy exchange process occurs over time. At equilibrium, the translational, rotational and vibrational energy distributions are described by Boltzmann distributions sharing the same temperature. Note that temperatures and energies form a bijection, such that referring to an energy is equivalent to referring to a temperature. Following a change of

temperature, the translational and rotational temperatures/energies typically relax towards equilibrium within a few tens to hundreds of collisions, while the vibrational temperature/energy requires orders of magnitude more collisions (see chapter VIII in [127]). Hence, when flow timescales become smaller than the local vibrational relaxation timescale, the single temperature model becomes invalid.

This happens behind compression/expansion waves where temperature brutally increases/decreases. An example of vibrational nonequilibrium triggered by a normal shock is now presented. One-dimensional post-normal shock profiles are computed using a vibrational energy relaxation model which will be described in Chap. II and are plotted in Fig. 1.14. The flow velocity is initially set to Mach 5.0 with a pressure of 20000 Pa and a temperature of 300 K. The left plots shows how fast e_{v,O_2} relaxes compared to e_{v,N_2}. As internal energy transfers from the over-excited translation and rotational modes towards the vibrational mode, T decreases. Incidentally, this process impacts density too, and inversely velocity as density times velocity remains constant. Note that the state right behind the shock corresponds to the normal shock calorically perfect gas solution, while the final relaxed state corresponds to the normal shock thermally perfect gas solution. A plateau is observed once O_2 has reached local equilibrium while N_2 population has not yet done so. Hence, this plateau temperature is still higher than the final equilibrated temperature. As seen in the right figure all the thermodynamic variables are affected by the energy relaxation process, with consequent changes of up to 20% of the TPG post-shock state in this example. Overall, cold vibrational nonequilibrium ($T_v < T$) results in a delayed conversion of kinetic energy K into internal enthalpy H. The opposite occurs through an expansion wave where hot vibrational nonequilibrium happens.

Figure 1.15 presents another effect of vibrational nonequilibrium. Viviani and Pezzella [128] showed that it affects the bow-shock standoff distance during hypersonic reentry. This shows that changes of the thermodynamic state also result in observable "geometric" modifications of the flow field.

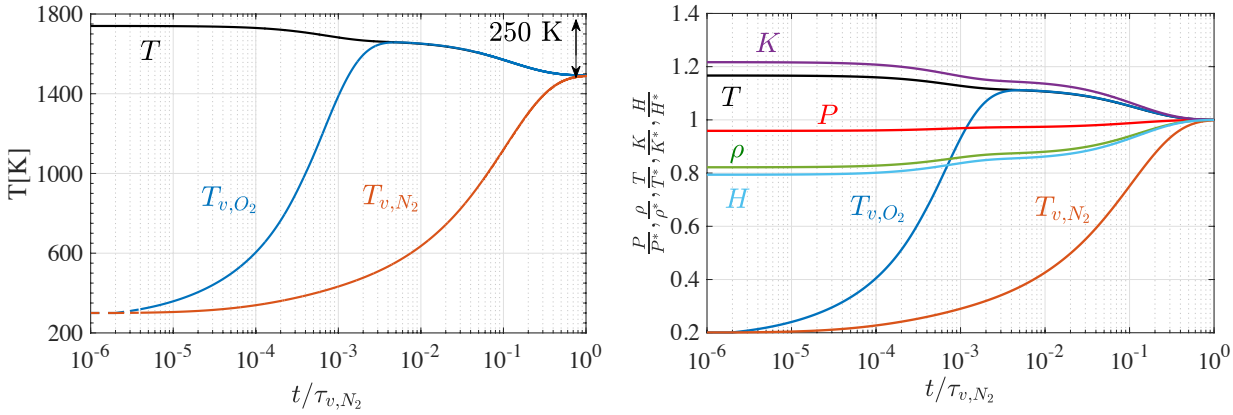

Figure 1.14: Vibrational energy relaxation behind a Mach 5.0 normal shock.

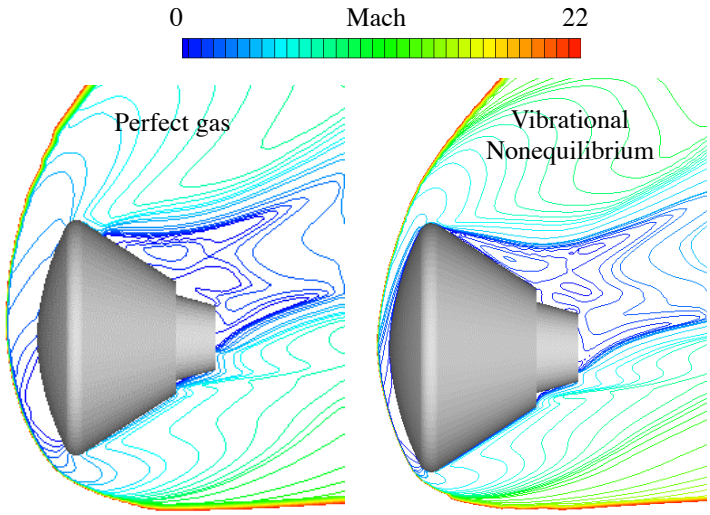

Figure 1.15: Effect of nonequilibrium on the bow-shock structure during atmospheric reentry from Viviani and Pezzella [128].

Vibrational nonequilibrium is usually studied in the context of hypersonic external flows such as atmospheric reentry [11, 101, 27]. However, these simple examples raise the following question: how does vibrational nonequilibrium impacts the flow inside a scramjet engine? One can imagine that shocks displacements or a 20% misprediction of thermodynamic variables could be catastrophic to the engine efficiency. Furthermore, chemical reactions are known to be sensitive to the internal energy states distribution [65, 64, 100, 130]. Collisions between highly excited molecules are indeed more likely to overcome the activation energy of

a particular reaction. Should the airflow still be out of equilibrium by the scramjet isolator outlet, the ignition process could be affected.

1.3.4 Measurements of vibrational energies in scramjet isolators

Despite a clear incentive into investigating the effects of vibrational nonequilibrium inside scramjets, this issue has not received much attention yet. Unfortunately, few experimental facilities have the capacity to generate nonequilibrium at all given the difficulty of replicating realistic hypersonic flight conditions, as explained below.

Scramjets are designed for hypersonic flights operating at high altitudes to mitigate drag and structural loads. Successful hypersonic vehicles such as the HyShot-II [117], the HyperX X-43 and the X-51A [43, 3] have operated at altitudes between 28 and 35 km in the stratosphere. At such altitudes, the pressure is roughly two orders of magnitude smaller than at sea-level and static temperature varies between 220 and 250 K. This means that for a vehicle traveling at Mach 6.0 for instance, the engine inflow total temperature T_t and pressure P_t are respectively 8.2 and 1578 higher: at 35 km this represents a total temperature of almost 2000 K. Pseudoshock experiments create a supersonic inflow by pressurizing a tank to several hundred times the atmospheric condition and expanding it in a channel through a Laval nozzle [120, 62, 16]. Pressurizing a tank up to hundreds of atmospheres is routinely done. However, creating a steady streamflow at such extreme temperatures requires to heat the tank up to the target T_t which is impractical in most laboratories. As a result, most pseudoshock-focused experiments occur at temperatures where the gas can be considered calorically perfect. Some facilities can accommodate high-enthalpy stagnation conditions [41, 76] but for the purpose of triggering ignition and studying thermal choking. Notably the High-Enthalpy Göttingen (HEG) hypersonic wind tunnel from the German Aerospace Center (DLR) performed experiments of a scaled scramjet combustor [76] at Mach 7.36 with a $h_t = 3.2$ MJ.kg^{-1} ($T_t = 2750$ K).

To the best of the author's knowledge, there exist two experimental studies considering

the species vibrational energies in the context of scramjet propulsion. Hannemann *et al.* [48] (also HEG) investigate the presence of vibrational nonequilibrium triggered by the upstream Laval expansion and concluded that the flow had reach equilibrium by the model scramjet intake. They did not consider nonequilibrium inside the model itself, triggered by the intake shocks or the isolator shock train. The high-enthalpy experimental study from Cutler *et al.* [26] attempted to do so. They measured the species vibrational energies using anti-Stokes Raman Spectroscopy in the combustor of a model ramjet. Contrary to [48] they observed that the N_2 vibrational temperature T_{v,N_2} remained close to the stagnation condition T_t (hence superior to local T) throughout the whole measurement window. This indicates that their ramjet model was placed too close to the upstream Laval nozzle to obtain a far-field equilibrium flow (as in a real flight, and as in [48]). The vibrational nonequilibrium triggered by the expansion wave, therefore, contaminated the whole domain, preventing any measure of the nonequilibrium triggered by the shocks structure. Additionally, it is unlikely that their experiment actually contained a pseudoshock (see wall pressure profile in Fig. 2 in [26]), but rather included an oblique shock attached to the injector ramp.

It can also be argued that an experimental study might not provide the best approach to understand the effect of the vibrational relaxation process on scramjets. Measuring the various species vibrational energies would certainly confirm the presence of nonequilibrium. However, it would be difficult to create a case-control experiment using the exact inflow Mach, density, pressure, diffusivity and thermal conductivity without the effect of nonequilibrium. It would require the use of a mono-atomic species of exact molecular weight. On the other hand, CFD tools could easily simulate the same configuration using different thermodynamic models. To the best of the author's knowledge, no numerical simulation has ever studied vibrational nonequilibrium inside scramjets. Therefore, to this day, the impact of vibrational nonequilibrium on the isolator remains unknown.

1.4 Dissertation goals

Section 1.2 demonstrated that the isolator's pseudoshock is a key component of DMSJ engines. It is responsible for both the compression stage serviceability and ensuring safe transitions between flight conditions. Its sensitivity to isolator inflow and outflow back pressure perturbations can be detrimental to the engine, leading to either inflow-triggered or choking-triggered unstart. In both unstarts, the key metric is the ratio between the pseudoshock pressure rise (as a function of the inflow conditions) to the isolator back pressure. The further from unity the ratio becomes, the larger the shocks displace within the isolator to adjust to the pressure gradient, effectively putting the engine at risk. The isolator has to be designed with sufficient margin to ensure that adverse flight conditions do not lead to unstart. However, a longer than necessary length introduces a turbulent mixing region that reduces compression efficiency due to friction losses. Hence, optimizing the length of the isolator is equivalent to estimating the length of the pseudoshock for the operational range of the vehicle. Likewise, the fuel injection scheme has to be precisely calibrated to avoid excessive flow-blockage/heat-choking and increase the isolator back pressure beyond its safety margin. Lastly, anti-unstart mechanics can be developed through upstream movable intakes or by adjusting the fuel mass flow rate to balance the pseudoshock and combustor pressures.

It is therefore of paramount importance to be able to predict both the pseudoshock length and back pressure rise as a function of inflow conditions. As of today, the lack of cheap and accurate predictive tools is detrimental to the design of robust isolators capable of containing the pseudoshock over a wide operational range. Namely, the influence of inflow confinement ratio on the pseudoshock structure is not fully understood yet.

One the goal of the dissertation is to investigate such dependence by the means of CFD, using a direct numerical simulation (DNS) approach. Contrary to RANS or LES, DNS does not rely on particular turbulence, sub-grid scales, and near-wall models. Instead, the grid resolution needs to be sufficiently high to resolve the smallest lengthscales relevant to the

problem, and grid convergence has to be proven. DNS is the ideal research tool as it does not introduce any artificial closure to the Navier-Stokes equations. However, DNS calculations are extremely expensive in terms of computational cost. The simulations presented in this dissertation were performed on high-performance computers, maintained by the NASA HECC group, and involved thousands of computer processors simultaneously for days, using a so-called distributed computing paradigm. DNS is also the ideal tool to study the effect of time-varying inflow conditions relevant to unstart. The pseudoshock sensitivity to inflow harmonic perturbations, as observed in Fig. 1.5, will also be numerically investigated. This new insight into pseudoshock physics will then be used to build a reduced-order model of pseudoshocks. The model will be designed to accurately predict the pseudoshock wall pressure profile over a wide range of inflow conditions. Also, it should be able to predict how inflow instabilities are filtered by the pseudoshock and propagate to the combustor.

One important aspect that has not received much attention from the scientific community yet. As explain in Sec. 1.3, the classical thermally perfect gas assumption becomes invalid in high-temperature and high-gradients flows. Thermodynamic nonequilibrium, namely vibrational nonequilibrium, could become relevant to scramjet internal flows by affecting the isolator outlet thermodynamic state. Furthermore, it could potentially alter the ignition process since chemical reactions are highly dependent on the internal energy distribution. It is particularly important to address this concern since flame stabilization and ignition are critical design considerations for a scramjet combustor. Overall, relying on data generated without resolving vibrational nonequilibrium could result in inaccurate models and a biased understanding of pseudoshock physics. This would cause isolators and fuel injection schemes to be misdesigned, endangering the engine. Moreover, anti-unstart mechanics calibrated using the equilibrium thermodynamic assumption could instead trigger unstart by over/under-predicting the pressure at the isolator inlet/outlet.

The other purpose of this dissertation is to decipher by the means of CFD the sensitivity of isolator pseudoshocks and supersonic combustion to vibrational nonequilibrium. A

compressible flow solver will be modified to resolve the vibrational relaxation process inside key elements such as the isolator and the combustor. A set of reaction rates depending on the reacting species vibrational energies will be used to properly account for the coupling between vibrational nonequilibrium and ignition. Comparative studies with the TPG model (assuming thermodynamic equilibrium) will also be carried out to quantify the relevance of resolving nonequilibrium in DMSJ.

Finally, the pseudoshock reduced-order model will be modified to account for the vibrational nonequilibrium effects.

Rotational equilibrium will be assumed throughout the dissertation, *i.e.* the rotational and translation energy states distributions share the same temperature T. Hence, the word "nonequilibrium" will simply refer to vibrational nonequilibrium when unspecified.

A summary of the dissertation's main goals is provided below. Note that they are all driven towards the same grand objective: use highly-detailed numerical simulation to address unstart and make DMSJ a viable propulsive mean for hypersonic vehicles.

1. Use DNS to study the pseudoshock sensitivity to inflow confinement
2. Use DNS to study the pseudoshock sensitivity to perturbations in time of the inflow conditions
3. Derive a reduced-order model for pseudoshocks
4. Implement the effects of nonequilibrium on a compressible reacting flow solver.
5. Use DNS to study the effects of nonequilibrium on compressible turbulent mixing and assess the limits of a multi-temperature approach
6. Use DNS to study the effects of nonequilibrium on DMSJ isolator flows
7. Use DNS to study the effects of nonequilibrium on DMSJ combustor flows

The dissertation is composed of the following chapters :

- **Chapter II:** The second chapter presents all the numerical tools used throughout the dissertation. This includes a presentation of the finite volume method, the compressible flow numerical schemes and of the DNS approach. The implementation of the multi-species numerical model used to resolve vibrational nonequilibrium is also detailed. An analysis of the effect of nonequilibrium on various canonical configurations will be performed using different models. Finally, working with computational chemists, modifications to reaction rates are incorporated for the numerical simulations of DMSJ combustors.

- **Chapter III:** A normal pseudoshock experiment is simulated in a model isolator by the means of DNS in this chapter. The objectives are to both verify the solver ability to simulate pseudoshocks, and investigate the effect of inlet boundary layer thickness on its structure. Three DNS computations of increasing inflow confinement ratio are performed to observe the evolution of the shock train structure as it becomes more confined. The number of details provided by the DNS permit to quantify the energy conversion process through the pseudoshock. Lastly, the shock train sensitivity to inflow harmonic perturbation is investigated.

- **Chapter IV:** The chapter presents the construction of a one-dimensional model for pseudoshocks based on a flux-conserved one-dimensional set of equations derived from the governing equations. The results obtained in Chap III are used to help derive a universal pressure growth rate closure equation for the model, which is then calibrated through Bayesian inference using a diverse collection of experimental and numerical datasets. Once the accuracy of the model assessed over a broad range of flow conditions, it is used to build an anharmonic oscillator model of the shock train resonance effect.

- **Chapter V:** In this chapter, a DNS of a pseudoshock is carried out using the nonequilibrium compressible flow solver described in Chap. II in order to study the effect of vibrational nonequilibrium on isolator flows. A case-control numerical simulation

using the thermally perfect gas model (or equilibrium model) is also performed. It is found that the isolator outflow thermodynamic state is noticeably different when resolving the relaxation process of the species vibrational energies. The effect of wall heat losses on the pseudoshock is also investigated. Finally, using the understanding gained from these DNS, the reduced-order model derived in Chap. IV is modified in order to account for these effects.

- **Chapter VI:** The impact of vibrational nonequilibrium on chemical reaction rates is described in Chap. II. In this chapter, these modified rates are used in a 9-species detailed chemistry model alongside the multi-temperature nonequilibrium solver. This solver is then used to simulate jet and crossflow configurations mimicking a DMSJ combustor. Both ramjet and scramjet modes are simulated (subsonic and supersonic crossflows). Finally, comparison with experimental data shows that resolving nonequilibrium results in a closer match.

- **Chapter VII:** The final chapter presents the conclusions of this work as well as various suggestions for future research.

CHAPTER II

Numerical methods and models for reacting flows with nonequilibrium

This chapter presents all the numerical tools used throughout the dissertation. This includes a presentation of the finite volume approach, the compressible flow numerical schemes and of direct numerical simulations (DNS). The implementation of the multi-species numerical model used to resolve vibrational nonequilibrium is also detailed. This modified solver is first tested on canonical configurations such as post-shock relaxation and free shear flows. Additionally, the coupling between turbulence and vibrational nonequilibrium is investigated by DNS. It is found that the multi-Tv model is adequate to study scramjet engines. As the burning efficiency is responsible for the back pressure ensuring a stable pseudoshock, it is also of paramount importance to investigate the effect of vibrational nonequilibrium on reaction rates which are indeed highly sensitive to the molecular energy states. Working with computational chemists, modifications to reaction rates are incorporated for the combustors simulations. Prior theories indicated that when nonequilibrium is present, chemical reactions are slowed down. By studying the quantum mechanical aspects of the reaction process, a new insight into this physics is developed which sometimes results in counter-intuitive effects. Part of this work is published in Fiévet *et al.* [39] and included in Fiévet *et al.* [38].

The chapter is organized as follows:

- Sec. 2.1 discusses the fundamentals of the in-house compressible flow solver UTCOMP.

- Sec. 2.2 describes the modeling of the vibrational energy relaxation process and its coupling with UTCOMP.
- Sec. 2.3 explains how the combustion model is modified to account for nonequilibrium by including efficiency functions, functions of reactive species temperatures.

2.1 Numerical methods for compressible flow simulations

This section presents some of the fundamental physics and assumptions used in the in-house compressible flow solver UTCOMP. All the time-resolved simulations[1] performed for this dissertation used this solver.

2.1.1 Conservation principles

A discontinuous description of fluid motion and thermodynamics was presented in Sec. 1.3, where a gas was defined as a system of N molecules interacting with each other through collisions. In most macroscopic flow, the mean free path (defined as the averaged distance between two molecular collisions) is negligible compared to the system relevant lengthscale (such as a golf ball diameter when studying its aerodynamic properties). In such cases, the flow properties can be considered continuous. Flow motion is often assumed to be continuous in fluid mechanics and will be throughout the dissertation. A flow element obeys to several fundamental conservative principles which describe its motion and evolution through time.

2.1.1.1 Conservation of mass

The first conservative principle concerns mass. Mass cannot change in an isolated thermodynamic system. With ρ being the fluid density, t a unit of time, x_i a direction of the 3D space and u_i the velocity component in the x_i direction, the conservation of mass is written in Eulerian formulation as:

[1]The RANS simulation presented in Sec. 3.3 was graciously done by from Dr.Baurle [NASA-Langley]

$$\frac{\partial \rho}{\partial t} + \frac{\partial \rho u_i}{\partial x_i} = 0 \tag{2.1}$$

2.1.1.2 Conservation of momentum

The second conservative principle is derived from Newton's second law. The flow element momentum rate of change is the sum of the external forces. In Eulerian form, it is written as the Cauchy momentum equation:

$$\frac{\partial \rho u_i}{\partial t} + \frac{\partial \rho u_i u_j}{\partial x_j} = -\frac{\partial P}{\partial x_i} + \frac{\partial \tau_{ij}}{\partial x_j}, i = [1, 2, 3] \tag{2.2}$$

In the right-hand side, P represent the surface normal force (pressure), τ_{ij} the shear stress (matrix trace equals zero) resulting from the flow viscosity, and f_i accounts for all body forces such as gravity. Gravity is usually neglected due to the reaction force (Newton's third principle). Also, flows like water, air or other gas are known to be Newtonian fluids: the viscous shear stress is proportional to the strain rate. Hence, $\tau_{ij} = \mu \frac{\partial u_i}{\partial x_j}$. The kinetic viscosity μ is evaluated using Sutherland's law and is a function of the flow temperature T and molecular composition.

2.1.1.3 Conservation of energy

The third conservation principle states that the total energy of a closed thermodynamic system is constant. The total energy ρe_{T} is the sum of the internal energy ρe presented in Sec. 1.3 and the gas kinetic energy ρK. In Eulerian form, and assuming no radiation or external body forces, it is written as:

$$\frac{\partial \rho (e + K)}{\partial t} + \frac{\partial \rho u_j (e + K)}{\partial x_j} = -\frac{\partial P u_i}{\partial x_i} + \frac{\partial \tau_{ij} u_i}{\partial x_j} + \frac{\partial q}{\partial x_i} + \rho \dot{S} \tag{2.3}$$

where q is the heat diffusion rate, and $\dot{S}$ is the energy source term from chemical reactions. It is common to use Fourier's law to express q as a $\lambda \frac{\partial T}{\partial x_i}$, where λ is evaluated from the Prandtl

number Pr which relates heat and momentum diffusion. Throughout the dissertation, the Prandtl number $Pr = \frac{\mu c_p}{\lambda}$ is set to 0.72, which is a common value for turbulent gas [140] usually within the [0.7 1.0] range. The Prandtl number can be an order of magnitude higher for liquids, but multi-phase flows will not be considered in this work. c_p is the gas heat capacity at constant pressure. The internal energy is, when using the thermally perfect gas model, evaluated as a 9^{th}-order polynomial function of temperature using the NASA coefficients from McBride *et al.* [86].

Equations 2.1 and 2.22.3 form the Navier-Stokes equations, and describe the motion of compressible viscous fluid.

2.1.1.4 Non-constant gas mixture

When the gas composition is not constant throughout space and time, conservation equations for each species mixture fractions Y_α are necessary. Such equation is written as:

$$\frac{\partial \rho Y_\alpha}{\partial t} + \frac{\partial \rho u_j Y_\alpha}{\partial x_j} = \frac{\partial}{\partial x_j} \rho D \frac{\partial Y_\alpha}{\partial x_j} + \rho \dot{S}_\alpha(Y), \tag{2.4}$$

where $Y = [Y_1, \cdots, Y_{N-1}]^T$ is the vector of $N-1$ species mass fractions and S_α the reaction source term. In all simulations considered in this work, the diluter species is nitrogen N_2. It is the N-th species and its mass fraction is simply calculated as $1 - \sum_{\alpha=1}^{N} Y_\alpha$.

2.1.2 Finite volume formulation

Computation fluid dynamics consists in resolving these conservation equations on a discrete representation of a domain of interest. The domain discretization generates a grid, which can be either structured (*i.e.* ordered, for instance, composed of uniform cubes) or unstructured (consisting of a tessellation of irregular patterns). UTCOMP uses structured grids only.

Every grid cell corresponds to a finite volume of flow which obeys to the conservation principles described in Sec. 2.1.1. There exist several mathematical methods to numerically

resolve these equations, the three classical choices are the Finite Different (FD), the Finite Volume (FV) and Finite Element (FE) methods. The FD is the oldest one and is based on a Taylor expansion approximation of all the derivatives in the conservation equations. This is feasible for simple discretization schemes such as in orthogonal structures meshes. the FV method consists in resolving the integral form of the conservation equation on every cell, assuming all the field variables to be constant within each cell. This method ensures a strict conservation and is applicable to complex meshes which makes it very popular. The third method, FE, consists in identifying a set of function solutions of the conservation equations at discrete locations.

UTCOMP uses a FV method. The integral form of the conservation equations can be formulated as:

$$\Delta \mathcal{C}_i = \frac{\mathcal{F}_{i-1/2} - \mathcal{F}_{i+1/2}}{\Delta x}\Delta t + (\text{Cell internal source term})\Delta t \tag{2.5}$$

where $\mathcal{F}_{i\pm1/2}$ is the flux of a particular conservative variable through a cell i's boundaries. The vector of conservative variables at cell i is called $\mathcal{C}_i = (\rho,\rho u,\rho v,\rho w,\rho e_{\mathrm{T}})_i$. The right-hand side, including for instance chemical reactions, does not introduce any particular complexity as long as the timestep is properly chosen to be much smaller than the source term timescale. The rate of change of the conservative variables equals the differences between inbound and outbound fluxes as illustrated for a uniform 1D grid in Fig. 2.1

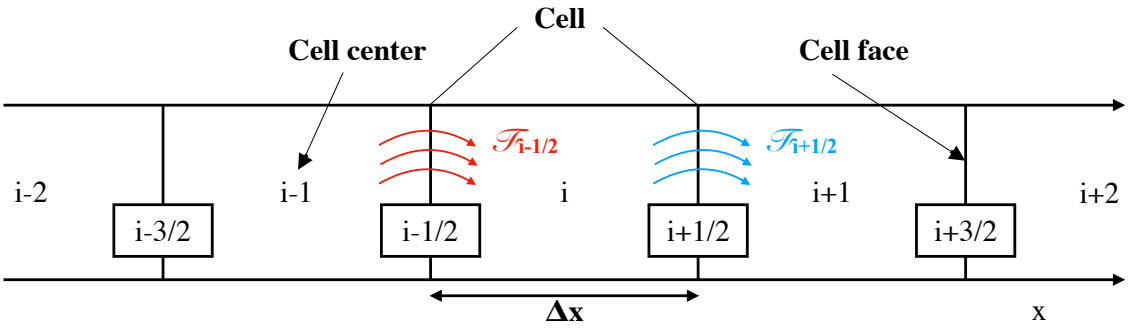

Figure 2.1: Sketch of the grid cell decomposition.

The FV method is inherently conservative as it balances the incoming/outgoing fluxes in every cell, and is therefore suited for fluid mechanics solvers based on conservation principles. Conservative methods permit to correctly resolve the Rankine-Hugoniot relation for discontinuities, which is of paramount importance for shock-containing flows [79]. It is also easily extendable in 3D space when using a structured grid as in UTCOMP.

2.1.3 Numerical schemes used in UTCOMP

The fluxes can be decomposed into the convective and diffusive fluxes. The diffusive fluxes are derived from the elliptic part of the Navier-Stokes equations. Diffusion smooths the flow solution by damping gradients [79]. Therefore, it has a stabilizing effect on the solution and is simply calculated using symmetrical central schemes. In UTCOMP, 4^{th} or 6^{th} order central difference schemes evaluate the second derivatives to compute the diffusive fluxes (both viscous and thermal fluxes).

The convective flux, however, originates from the hyperbolic part of the Navier-Stokes equations. In a hyperbolic system of equations, waves travel through space at finite speeds. There exist a set of trajectories called characteristics (system eigenvectors) along which waves remain constant while convecting at constant speeds (system eigenvalues). When characteristics merge, a singularity appears which is resolved by forming a discontinuous solution. The hyperbolicity of Navier-Stokes equations is the reason shock waves exist. The 5 eigenvalues of the hyperbolic part of the 3D Navier-Stokes equations are given by $|u_i|$ and $|u| \pm c$ where c is the local speed of sound. The numerical schemes computing the convective flux in a compressible flow solver need to accurately capture the shock waves and verify the Rankine-Hugoniot relation: these are called shock-capturing schemes. Naively using central schemes for the convective flux (as for the diffusive flux) result in spurious oscillations (Gibbs phenomenon) appearing near discontinuities. These can cause the density to become negative and the solution to diverge.

There exist many different shock-capturing numerical schemes for FV methods (see chap-

ter 12 in [79]), with varying degrees of accuracy and complexity. The FV method essentially introduces a discontinuity at every cell faces, hence every cell boundary consists in a local Riemann problem. Direct (Godunov scheme) or approximate (Roe scheme) Riemann solvers can be used to calculate the local solution at the cell interface $\mathcal{C}_{i\pm1/2}$, and then compute the resulting flux $\mathcal{F}_{i\pm1/2}(\mathcal{C}_{i\pm1/2})$. Note that the solution $\mathcal{C}_{i\pm1/2}$ is constant and entirely determined by the local Riemann problem as long as the characteristics incoming from the neighboring Riemann problems (*i.e.* the neighboring cell faces) have not yet crossed this face. This restriction determines the local timestep. Godunov's elegant way of treating each cell boundary as a 1D shock interface permits to find exact mathematical solutions. However, Riemann solvers are computationally expensive and can result in very small timesteps. Another approach consists in splitting the interface flux into contribution from the two neighbouring cells: $\mathcal{F}_{i\pm1/2} = \mathcal{F}^{-}_{i\pm1/2} + \mathcal{F}^{+}_{i\pm1/2}$. The negative and positive fluxes are reconstructed from cell-centered values, then summed to form a cell face flux. This bypass the need to compute a Riemann solution at the cell faces. Such numerical schemes are called flux splitting schemes. Lastly, high-order compact Padé schemes simply interpolate the primitive variables gradients to the cell faces. They then resort to an artificial increase of numerical dissipation around discontinuities to dampen the oscillations. This requires an efficient shock-detection metric and a careful calibration of the extra amount of dissipation. The last two numerical schemes are used in UTCOMP.

The first one is a 5^{th} order conservative FD-WENO-LLF scheme with characteristics reconstruction of Jiang and Shu [56, 115]. WENO stands for "weighted essentially non-oscillatory", while LLF stands for "local Lax-Friedrich" which is the flux-splitting scheme shown in Eq. 2.6. ENO schemes resolve discontinuities by adjusting the local stencil to upwind the solution wherever necessary. WENO schemes combine all the different stencils fluxes to compute the less oscillatory solution. In the FD version of WENO, the fluxes are first computed at the stencil's cell centers and then reconstructed (a sort of interpolation scheme) at the cell faces [115]. Instead, in FV-WENO, the cell-averaged values are used to

interpolate cell faces values, which are then used to evaluate the fluxes. Shu suggests to use the cheaper FD version on smooth grids and the FV version on more complex meshes, hence the FD version is implemented in UTCOMP. All stencils use 5 neighboring cells. Since a flux-splitting scheme is used both $\mathcal{F}^{-}_{i\pm1/2}$ and $\mathcal{F}^{-}_{i\pm1/2}$ are reconstructed. The reconstruction for $\mathcal{F}^{-}_{i+1/2}$ uses a biased stencil with one more point to the left ($i-3$ to $i+2$), while that for $\mathcal{F}^{+}_{i+1/2}$ uses a biased stencil with one more point to the right ($i-2$ to $i+3$ to obey correct upwinding. The characteristic reconstruction method reconstructs the fluxes in the characteristic variable space. Oscillations are less likely to develop when reconstructing in characteristic space instead of primitive or conservative spaces [115, 57]. The author also found out that activating characteristic reconstruction would result in a noticeably less diffusive solution. The conversion between these spaces is done by multiplying the variable vector with the Jacobian's eigenvector matrix.

$$\mathcal{F}^{\pm}(\mathcal{C}) = \frac{1}{2}(\mathcal{F}(\mathcal{C}) \pm \left|\frac{\partial \mathcal{F}}{\partial \mathcal{C}}\right| \times \mathcal{C}) \tag{2.6}$$

The conservative FD-WENO-LLF scheme consists of the following steps:

1. Compute the fluxes in all the stencil's cell centers
2. Convert both the conservative variables and the fluxes into the characteristic space
3. Do the LLF flux-splitting
4. Reconstruct the left and right fluxes at the cell faces
5. Convert back to the conservative variables space
6. Average the $\mathcal{F}^{-}_{i\pm1/2}$ and $\mathcal{F}^{+}_{i\pm1/2}$ at every cell face
7. The difference $\mathcal{F}_{i-1/2} - \mathcal{F}_{i+1/2}$ evolves the solution at cell i through time.

While very efficient at damping shock-triggered oscillations, WENO schemes are however also diffusive. This can be detrimental to the resolution of fine turbulence scales [58].

The second numerical scheme is a 6^{th} order compact Padé scheme with hyperviscosity from Cook [22, 23]. The compact scheme permits to interpolate at the cell faces the primitive variables and their derivatives as well (see Koo [68] pp.36-37), which is all that is needed to evaluate the local fluxes. This method does not include any sort of flux-splitting or upwinding. While it is not diffusive as WENO, it is instead dispersive and is unable to damp numerical oscillations. Shock oscillations are damped by a hyperviscosity scheme which artificially increases viscosity in high-gradient regions. The smaller dispersive waves can also lead to an unstable solution if not canceled, hence an 8^{th} order implicit filter is applied over the computational domain at the end of each timestep sub-iterations. This process involves matrix inversions which render Padé schemes less cost-effective than WENO for large-scale simulations as seen in Figs. 2.2 and 2.3.

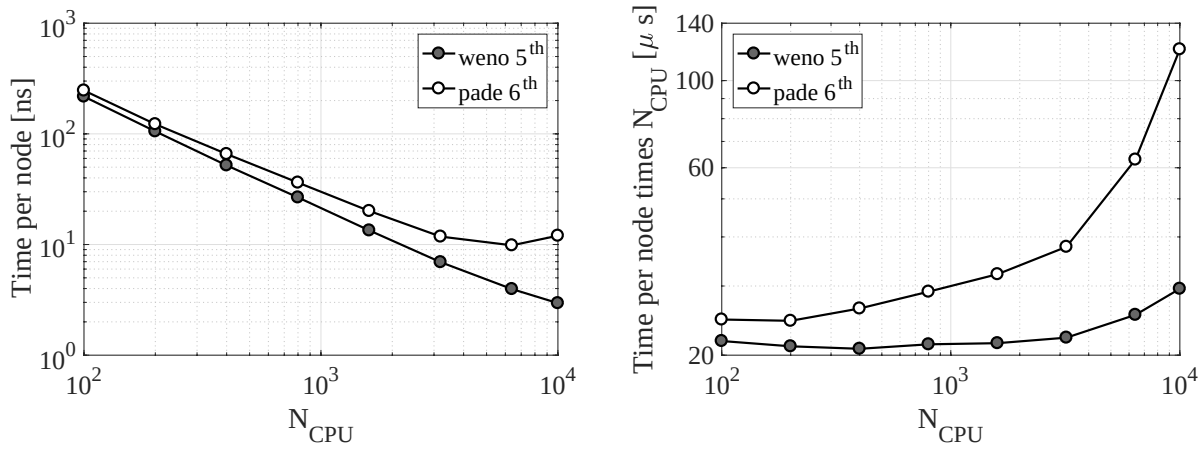

Figure 2.2: UTCOMP scaling efficiency for a constant grid using both WENO and Padé schemes.

Figure 2.4 compares some shock train simulations using the two numerical schemes presented above. The grid is kept very coarse (n_x,n_y,n_z) = (1024,128,128), which incidentally has the effect of fading the leading shock when using WENO. At higher resolutions, as will be presented in Chap. III, the WENO solution presents a similar leading lambda-shock (see Fig. 3.3), and differences with Padé become minimal. However, despite the use of hyperviscosity, the Padé shock train exhibits shock oscillations and needs to run at very low CFL number to

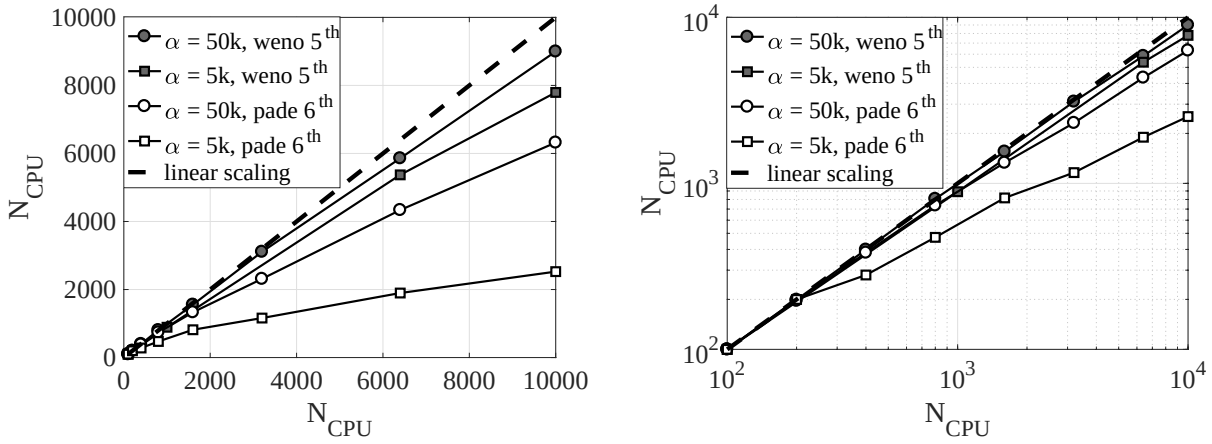

Figure 2.3: UTCOMP scaling efficiency for a constant ratio between number of grid points and processors using both WENO and Padé schemes.

remain stable. Increasing the hyperviscosity coefficients can cancel the oscillations, however, it also dissipates turbulence and reduces the timestep as the viscous CFL number increases.

Due to these limitations in both stability, accuracy and computational cost, it was decided to use the WENO scheme in all large-scale/shock-containing flows presented in this dissertation. The Padé scheme will be used only to generate shock-free highly turbulent inflow files for the main simulations.

Hybrid WENO-central schemes [24, 105, 58] provide a compromise between diffusive WENO and unstable central schemes. It consists in a variable scheme which depends on a local shock detector. Pirozzoli [105] and Costa *et al.* [24] define a Heaviside function which determines whether the WENO of less-diffusive scheme is used. This can be problematic in unsteady problems when trying to sample statistics. On the other hand, Johnsen *et al.* [58] used a linear combination of both schemes which ensures a continuous transition in space between the schemes. They showed that the hybrid scheme performed better than both the hyperviscous compact Padé and 5^{th} order WENO schemes in terms of shock and compressible turbulence resolution. However, the derivation of a universal sensor is still the focus of ongoing research. Continuous hybrid schemes were not used in the present work, but would certainly be a valuable addition to UTCOMP.

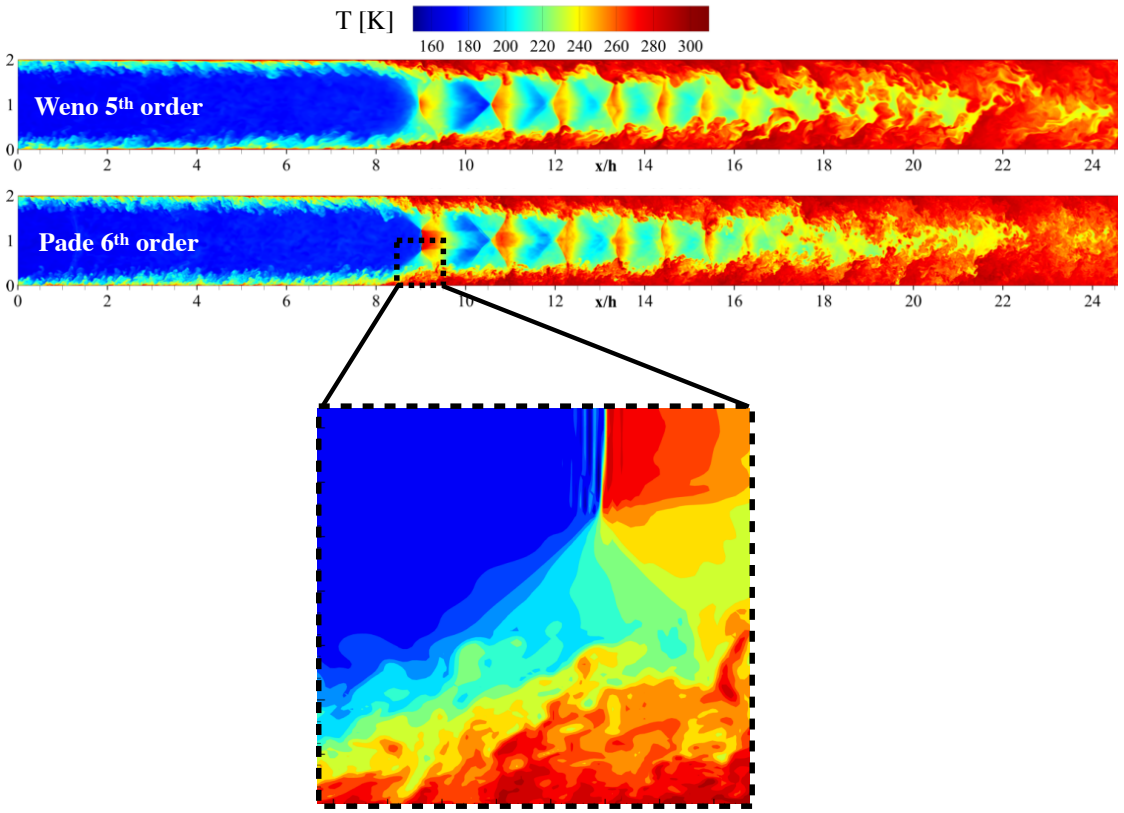

Figure 2.4: Typical snapshots of temperature [K] in a normal shock train using either (top) a WENO 5^{th} and a (bottom) Padé 6^{th} order schemes on a coarse grid ($1024 \times 128 \times 128$).

Finally, time-integration is performed by an explicit (forward-marching) total-variation-diminishing 4^{th} order Runge-Kutta scheme. The scalars are transported using a QUICK scalar scheme [78].

2.1.4 Numerical boundary conditions

In UTCOMP, boundary conditions are treated with the use of ghost cells located all around the computational domain. Due to the size of the stencils used in the convective schemes, 3 ghost cells are needed along each direction's domain boundary. Wall boundaries are treated with zero-gradient density and zero-velocities u, v and w (no-slip conditions). The ghost cells temperature is either fixed to enforce zero-gradient in the case of adiabatic conditions, or with a fixed value in the case of isothermal conditions.

Flowing boundaries (as opposed to walls) have to be carefully treated. The inflow bound-

ary ghost cells are populated with solutions read from an inflow file, which contains the time-resolved solution from an auxiliary simulation. For instance, in the case of an isolator simulation as seen in Fig. 2.4, the inflow file contains a periodic 3D compressible turbulent boundary layer flow sampled in a periodic channel using the same grid. If the inflow plane normal-velocity is supersonic, then all the flow characteristics enter the domain ($|u|$ and $|u \pm c|$ are all positive), and the inflow file determines all the inflow variables. However, $|u - c|$ becomes negative whenever this speed is subsonic, and an upstream-running characteristic exits the domain through the inflow plane. Hence the inflow thermodynamic state is partially computed using information coming from inside the domain. Likewise, outflow boundary ghost cells will simply replicate the last domain cell values u_i, ρ and T if the exit plane normal velocity is supersonic. Otherwise, one characteristic enters the domain from the outflow plane: a numerical back pressure is used to evaluate the thermodynamic state inside the ghost cells and diffuses upstream. The implementation of Navier-Stokes Characteristic Boundary Conditions (NSCBCs) follows the method from Poinsot and Lele [108]. This method enforces partially non-reflecting boundary conditions by letting the instantaneous pressure ghost cells slightly deviate from the imposed far-field pressure.

2.1.5 The DNS approach

As explained in Chap. I, the numerical model used for this work is the DNS. It consists in resolving the exact conservation equations on a grid fine enough to resolve all the problem's relevant lengthscales. Typically, when investigating turbulence, one aims to resolve the full turbulence energy cascade [109]. This requires to have a maximum grid cell size of twice the smallest local turbulence wavelength, referred to as the Kolmogorov lengthscale. This approach differs from cheaper models such as the LES which add a turbulence subgrid model to simulate the effect of the unresolved turbulence lengthscales on the flow. The Kolmogorov lengthscale is defined as $\eta = \left(\frac{\nu^3}{\epsilon}\right)^{\frac{1}{4}}$ for isotropic turbulence: it is a ratio of flow kinetic viscosity ν over the turbulence energy dissipation rate ϵ. However, in the context of

anistotropic flows such as wall-bounded flows, this ratio tends towards zero at the wall: it is unsuited to quantify the grid resolution. Instead, a wall unit $y+$ is defined based on the turbulent boundary layer properties. It is well known that the wall-normal velocity profile is linear in close vicinity to the wall inside a region called the inner region. In the outer region, the profile transitions towards a logarithmic function of $y+$. It is necessary to correctly resolve this profile when generating turbulent boundary layer inflows, as will be shown later in Chaps. III and V. Additionally, the minimum grid resolution requirement for a wall-confined DNS [133] across the computational domain are: $\Delta x < 15y+$, $min(\Delta y) < 1y+$, $max(\Delta y) < 15y+$ and at least 3 cells included within a distance of $10y+$ from all walls.

Throughout the dissertation, the accuracy of the simulations will be demonstrated in two possible ways. First, for free shear flows such as the planar jet DNS presented later in this chapter, the grid refinement will be directly compared with the Kolmogorov lengthscale. This is the most accurate way of verifying the quality of a grid. Second, in the case of wall-bounded flows, grid refinement studies demonstrating the convergence of metrics of interest will be presented for validation purposes. Note that in such flows, the Kolmogorov lengthscale might not be resolved everywhere, hence these simulations could be referred as under-resolved DNS instead. Last, the resolution of the turbulent boundary layer will also be assessed by verifying that the viscous sub-layer and outer-layer are properly captured.

To conclude this section, UTCOMP has been extensively validated on a set of canonical problems using both DNS and LES methods [68] and used on many diverse numerical studies [69, 70, 30, 39, 33]. The code uses domain-decomposition based parallelization and relies on Open MPI libraries.

2.2 Compressible flow solver with vibrational nonequilibrium

In order to study the effect of vibrational nonequilibrium in scramjet engines, the compressible flow solver presented in Sec. 2.1 is modified to resolve the vibrational energy relaxation process. Two models will be presented in this section based on either a multi-

temperature or a state-specific approach.

2.2.1 Multi-temperature model

The multi-temperature model is based on the decoupling of the vibrational energies of all present polyatomic species from the total energy conservation equation. It requires an additional conservation equation for each vibrational energy. The vibrational energy of molecular species α is defined as:

$$e_{v\,\alpha} = \int_{T_{\mathrm{ref},\alpha}}^{T_{v\,\alpha}} c_{v\,\alpha}(T')dT' - \beta_\alpha R(T_{v\,\alpha} - T_{\mathrm{ref},\alpha}). \tag{2.7}$$

In the above expression, $c_{v\,\alpha}$ is the specific heat at constant volume for species α, $T_{v\,\alpha}$ is the vibrational temperature defined relative to a reference temperature $T_{\mathrm{ref},\alpha}$ equals 298.15 K, and β_α is 5/2 for linear molecules and 3 for nonlinear molecules. Note that this represents the vibrational energy above the vibrational energy ground state, which is non-zero contrary to translational and rotational energy, and is already included in the internal energy at $T_{\mathrm{ref},\alpha}$. The translational temperature is simply called T. The rotational distribution is assumed to be fully equilibrated, i.e. $T_{\mathrm{r}} = T$. The above formulation of vibrational energies exactly recovers the equilibrium energy equation with the TPG model under equilibrium conditions when $T_{v\,\alpha} = T$ for all α.

The governing equations for fluid flow are then given by Eqns. 2.1, 2.2 and energies transport equations. The internal energy of the system is divided into different parts: the translational + rotational and the species vibrational components. Hence, the conservation equation of total energy is split between these components following the CVCV method of Knab *et al.* [65, 64].

The transport equations for the kinetic+translational+rotational energy, e_{trk}, is given by

$$\frac{\partial \rho e_{\mathrm{trk}}}{\partial t} + \frac{\partial u_j(\rho e_{\mathrm{trk}} + P)}{\partial x_j} = \frac{\partial}{\partial x_j}\lambda\frac{\partial T}{\partial x_j} + \frac{\partial}{\partial x_j}(\tau_{ij}u_i) - \sum_{\alpha=1}^{N_{\mathrm{m}}} Q_{\mathrm{T-V}_\alpha} + \sum_{\alpha=1}^{N_{\mathrm{m}}} Q_{\mathrm{C-V}_\alpha}, \tag{2.8}$$

where $Q_{\mathrm{T-V}_\alpha}$ denotes the energy exchange between the translational+rotational and vibrational modes, which leads to full thermal equilibrium for the molecular species α. N is the number of species present in the mixture. The vibrational-translational energy exchange is modeled using the Landau-Teller model [74]: the relaxation rate is proportional to the local gradient between $e_{v\,\alpha}(T_{v\,\alpha})$ and $e_{v\,\alpha}(T)$) and inversely proportional to a relaxation timescale $\tau_{v\,\alpha}$ [127]. $Q_{\mathrm{T-V}_\alpha}$ is written as:

$$Q_{\mathrm{T-V}_\alpha} = \rho Y_\alpha \frac{e_{v\,\alpha}(T) - e_{v\,\alpha}(T_{v\,\alpha})}{\tau_{v\,\alpha}}, \tag{2.9}$$

where Y_α is species α mass fraction. $\tau_{v\,\alpha}$ is found using a mixture rule, and the relaxation timescale of pairwise collisions $\tau_{\alpha\beta}$ between N species in the system is

$$\tau_{v\,\alpha} = \frac{1}{\sum_{\beta=1}^{N} \frac{\chi_\beta}{\tau_{\alpha\beta}}}, \tag{2.10}$$

where χ_β is the mole fraction of species β. The pairwise relaxation timescale is obtained based on an empirical fit to experimental data from Millikan and White [90]:

$$\tau_{\alpha\beta} = \frac{1}{P}\exp[1.16 \times 10^{-3} \mu_{\alpha\beta}^{\frac{1}{2}} \theta_{v\,\alpha}^{\frac{4}{3}} (T^{-\frac{1}{3}} - 0.015\mu_{\alpha\beta}^{\frac{1}{4}}) - 18.42], \tag{2.11}$$

where $\mu_{\alpha\beta}$ is the reduced mass of the pair and $\theta_{v\,\alpha}$ is the characteristic vibrational temperature of the species. Figure 2.5 shows species self-scattering relaxation timescales. The vibrational relaxation timescales strongly depend on the nature of the species: species α with a high vibrational activation temperature $_{v\,\alpha}$ possess higher relaxation timescales. Notably, N_2, relaxes almost a thousand times slower than O_2. Millikan and White correlation reproduces experimentally measured relaxation times for mixtures over temperatures covering the operational range of a scramjet engine [90]. It was derived from cold-to-hot relaxation only (post-compression relaxation). As noted by Cutler *et al.* [25], this correlation accurately resolves the post-shock relaxation process but uncertainties remain on its ability to describe the opposite relaxation effect in an expanded gas. This vibrational relaxation model

will be referred as the LTMW model (Landau-Teller with Millikan and White correlation), and implies a multi-temperature description of nonequilibrium. Note that a simpler two-temperature model has been considered before [72, 100, 102] consisting in using a single mixture-averaged T_v. In this simpler formulation, the mixture T_v relaxation timescale is heavily weighted towards the diluter N_2 relaxation timescale. Therefore, the vibrational energy of fast-relaxing species such as H_2O or O_2 will not be correctly evaluated.

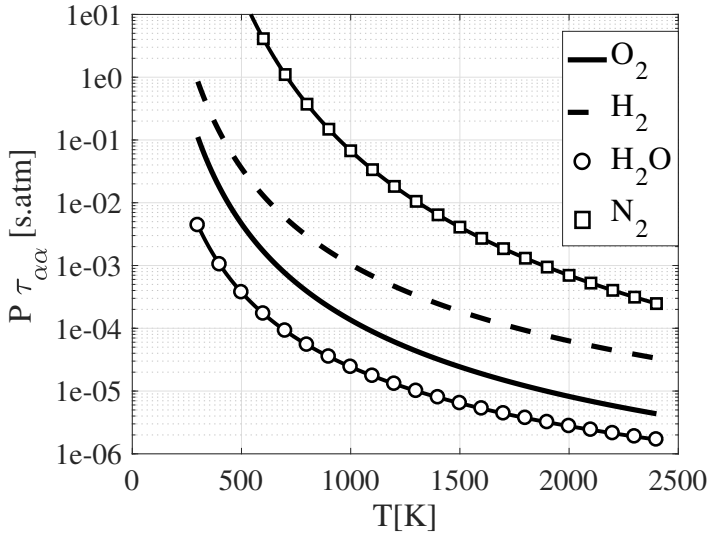

Figure 2.5: Species self-scattering relaxation timescales computed from Millikan and White correlations.

In Eq. 2.8, $Q_{\mathrm{C-V}_\alpha}$ is the chemistry-vibration coupling term [65]. When a molecule containing a vibrational energy dissociates, this energy is lost to other modes. Likewise, when a polyatomic molecule forms, it will possess a certain vibrational energy. This term will essentially decrease the reactant species vibrational energies as the molecules with higher vibrational quantum number are, in a simplified picture, more likely to overcome their reaction activation energy. Hence, the reacting molecules are skewed towards the high-energy states. Knab *et al.* shows that this term can be approximated as :

$$Q_{\mathrm{C-V}_\alpha} = \left[\frac{R\theta_{v,\alpha}}{e^{\frac{\theta_{v,\alpha}}{T_{v,\alpha}}} - 1}\right]\left[\frac{\mathcal{D}_\alpha}{e^{\frac{\mathcal{D}_\alpha}{RT_{v,\alpha}}} - 1}\right]\rho\dot{S}_\alpha \tag{2.12}$$

where $\mathcal{D}_\alpha$ is species α's dissociation energy.

The conservation equation of the vibrational energy of molecular species α, $e_{v\,\alpha}$, is given by

$$\frac{\partial \rho Y_\alpha e_{v\,\alpha}}{\partial t} + \frac{\partial \rho Y_\alpha u_j e_{v\,\alpha}}{\partial x_j} = \frac{\partial}{\partial x_j}\lambda_{v\,\alpha}\frac{\partial T_{v\,\alpha}}{\partial x_j} + Q_{\mathrm{T-V}_\alpha} + \sum_{\beta=1}^{N_\mathrm{m}} Q_{\mathrm{V}_\beta-\mathrm{V}_\alpha} - Q_{\mathrm{C-V}_\alpha}. \tag{2.13}$$

where $\lambda_{v\,\alpha} = \frac{\mu c_{p,v\alpha}}{Pr}$ is the vibrational energy thermo-conductivity and $Q_{v_\beta - v_\alpha}$ denotes the vibrational energy exchange rate between all species, defined as [64]:

$$Q_{\mathrm{V}_\beta-\mathrm{V}_\alpha} = N_\mathrm{a}\sigma_{\alpha\beta}\sqrt{\frac{8RT}{\pi\mu_{\alpha\beta}}}P_{\alpha\beta}\rho^2 Y_\alpha Y_\beta\left[\frac{e^{eq}_{v\,\beta}}{e^{eq}_{v\,\alpha}}e_{v\,\alpha} - e_{v\,\beta}\right], \tag{2.14}$$

where $\sigma_{\alpha\beta}$ is the collisional cross-section, N_a is Avogadro's number, R the universal gas constant, $e^{eq}_{v\,\alpha}$ the vibrational energy of specie α evaluated with the local translational temperature. In the current study, this summation simply equals $Q_{v_{\mathrm{O}_2} - v_{\mathrm{N}_2}}$ and there only is one $P_{\alpha\beta} = P_{\mathrm{O_2N_2}}$. $P_{\mathrm{O_2N_2}}$ is the exchange probability that a collision between a O_2 and N_2 molecules result in a change of vibrational states at constant translational and rotational quantum numbers. Knab *et al.* arbitrarily fixed it to 0.01 since the occurrence of a collision resulting in a V-V exchange is relatively small compared to a V-T exchange or simply no exchange at all (elastic collisions).

Reising *et al.* [111] showed that a value of 0.0001 (which essentially curtails all V-V energy exchanges) gave a closer match with experimental vibrational temperature profiles obtained from turbulent mixing between 500 and 1500 K streams. Based on this study, $P_{\mathrm{O_2N_2}}$ was set to 0.0001 in UTCOMP. Recent computational chemistry calculations from Voelkel [129] showed that $P_{\mathrm{O_2N_2}}$ varies between 0.000065 and 0.0002 for translational temperatures between 500 and 2000 K (relevant range in the current configuration).

The example of one-dimensional post-normal shock vibrational energy relaxation profiles presented in Fig. 1.14 used the model presented in this section.

2.2.2 State-specific scattering rates

The multi-temperature model makes an important assumption: it considers that the species vibrational states distributions remain Boltzmann-like at nonequilibrium. However, it is known that the states' populations evolve through molecular scattering, and it is unlikely that such stochastic process will not affect the shape of the states distributions. A method called Quasi-Classical-Trajectory (QCT) permits to resolve the states distribution instead of its integral value [6, 130, 131]. It requires to transport every state population and to model the inelastic state-specific scattering rates. An inelastic collision is a collision resulting in a change of the collided molecules vibrational quantum numbers. The QCT approach, by its quantized description of the vibrational energy, is both more accurate and computationally more expensive than the empirical LTMW model. It will, therefore, be used in the remainder of this section to assess the LTMW capacity in resolving expansion and mixing-triggered nonequilibrium.

2.2.2.1 Quasi-Classical-Trajectory formulation of inelastic rates

The vibrational inelastic rates for the reaction

$$\mathrm{N}_2(v_1) + \mathrm{N}_2(v_2) \longrightarrow \mathrm{N}_2(v_1') + \mathrm{N}_2(v_2') \tag{2.15}$$

were calculated by Voelkel using the QCT code [129]. The QCT method assumes that the motion of the nuclei are classical and driven by the potential energy surface (PES). Hence, this method requires PES for all the different kind of molecular collisions occurring inside the computational domain. Such information is often unavailable as PES are still the focus of ongoing research. Available PES for N_2-N_2 collisions were used to compute the trajectories and collisions occurring in a pure Nitrogen mixture [40]. For a particular trajectory, the i^{th} nuclei follows a classical path governed by

$$\frac{d\boldsymbol{Q}_i}{dt} = \boldsymbol{P}_i \tag{2.16}$$

$$\frac{d\boldsymbol{P}_i}{dt} = -\frac{\partial V}{\partial \boldsymbol{Q}_i}, \tag{2.17}$$

where $\boldsymbol{Q}_i$ and $\boldsymbol{P}_i$ are the position and momentum vectors of the i^{th}, respectively, and V represents the PES. Solving these classical equations is the main process in a QCT simulation. A thorough description of Voelkel's QCT algorithm is given in [129]. For the sake of clarity, a brief summary is provided.

The first 10 vibrational quantum numbers were sampled, so for N_2-N_2 collisions, there exist 10^4 vibrational state combinations (*i.e*, degrees of freedom). A total of 2.8 billion trajectories were simulated using the QCT program developed by Voelkel et al. [130, 131] on the Texas Advanced Computing Center (TACC) machine using 4,104 cores for 30 hours. At the end of each trajectory, the final vibrational quantum number was determined as the closest lying state compared to the classical vibrational energy resulting from the collision. The inelastic scattering rates were approximately determined using Monte-Carlo integration as conventionally done in QCT analysis [6, 130, 131]. Here, the rates were determined a function of a translational-rotational temperature T, an initial vibrational quantum number $\boldsymbol{v} = (v_1, v_2)$, and a final vibrational number $\boldsymbol{v}' = (v_1', v_2')$. The scattering rate is denoted as $k_s(\boldsymbol{v}, \boldsymbol{v}', T)$. So, for each trajectory, $\boldsymbol{v}$ is fixed, and the relative speed and initial rotation quantum numbers are sampled based on their respective probability distribution functions (PDFs). After the N_2 molecules collide, the final state is marked (*i.e.*, $\boldsymbol{v}'$). The aggregation of the outcomes is used to determine the inelastic scattering rates. More details on the sampling of the inelastic scattering rates can be found in Fiévet *et al.* [40] for this N_2-N_2 system.

Figure 2.6 compares the thermal equilibrium dissociation rate computed via QCT in the temperature range 6000 to 60000 K. The results are almost identical to those of Bender *et*

al. [5] who used the same potential energy surfaces.

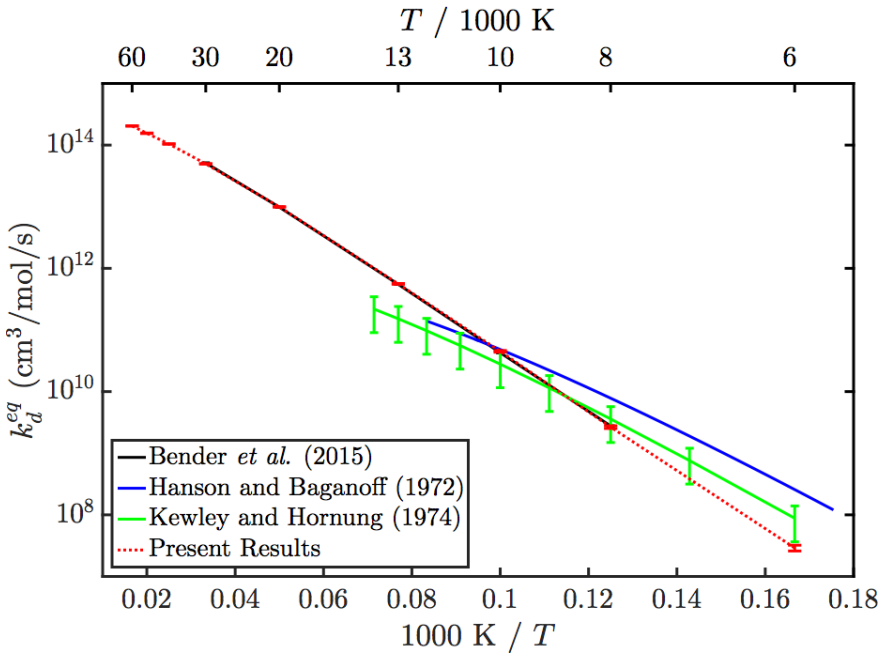

Figure 2.6: Verification of the QCT code through comparison of N_2 dissociation rates with other calculations and experiments.

2.2.2.2 Implementation of the state-specific rates into UTCOMP

The integration of the relaxation rates into the compressible flow solver is done by adding additional transport equations for every state's population number density (in the present study, 10 equations), and by transforming the energy conservation equation to account for V-T energy transfer modes.

ϕ_m is the number density of vibrational energy state level m, and its source term is called $\dot{\phi}_m$. The transport equation of ϕ_m is defined as :

$$\frac{\partial \rho \phi_m}{\partial t} + \frac{\partial \rho u_i \phi_m}{\partial x_i} = \frac{\partial}{\partial x_i} \rho D \frac{\partial \phi_m}{\partial x_i} + \rho \dot{\phi}_m. \tag{2.18}$$

$\dot{\phi}_m$ is directly computed from the state-specific rates :

$$\dot{\phi}_m = \sum_i \sum_j \sum_k \sum_l \epsilon_{m,ijkl} \times k_s(v_i \rightarrow v_k, v_j \rightarrow v_l, T) \times \phi_i \times \phi_j, \tag{2.19}$$

where $\epsilon_{m,ijkl}$ characterizes the impact a particular reaction would have on the mth level population, and is defined as :

$$\epsilon_{m,ijkl} = -\delta_{i,m} - \delta_{j,m} + \delta_{k,m} + \delta_{l,m}. \tag{2.20}$$

While energy gets pumped in/out of the gas molecules vibrational motion during relaxation, energy conservation ensures that an equal amount is transferred from/into the two other modes of internal energy: the translation and rotational modes. We call e_{trk} the sum of the translational, rotational and kinetic energies which are assumed to be local thermodynamic equilibrium. The coupling with Navier-Stokes equations appears in the right hand side of e_{trk} transport equation. All the source terms of states populations number densities ϕ_k are multiplied by their respective vibrational level energy $e_{v,k}$, and summed up to represent the amount of energy transferred into vibrational motion. The transport equation of e_{trk} becomes :

$$\frac{\partial \rho e_{\text{trk}}}{\partial t} + \frac{\partial u_j(\rho e_{\text{trk}} + P)}{\partial x_j} = \frac{\partial}{\partial x_j}\left(k\frac{\partial T}{\partial x_j}\right) - \frac{\partial}{\partial x_j}(\tau_{ij}u_i) - \rho\sum_k \dot{\phi}_k(e_{v,k} - e_{v,0}) \tag{2.21}$$

where ρ is the fluid density, u_i is the velocity vector and k the heat transport coefficient.

In addition to the energy conservation Eq. 2.21, the compressible solver's governing equations are given by the conservation of mass and momentum.

2.2.2.3 Reduced formulation of the state-specific rates

In an effort to reduce the computational cost of rates calculations at every iteration, $\dot{\phi}_m$ does not need to be directly computed as in Eq. 2.19. Instead, it is reduced into a more compact form during the initialization of the simulation. In Eq. 2.19, the summations on the index k and l corresponding to the product of the scattering reaction rate can be pre-computed into a matrix of size number of levels power 3 called $\mathcal{R}_{mij}$ defined as :

$$\mathcal{R}_{mij} = \sum_k \sum_l \epsilon_{m,ijkl} \times k_s(v_i \rightarrow v_k, v_j \rightarrow v_l, T). \tag{2.22}$$

Then, Eq. 2.19 simply becomes

$$\dot{\phi}_m = \sum_i \sum_j \mathcal{R}_{mij} \times \phi_i \times \phi_j. \tag{2.23}$$

It can be observed that this reduced formulation is analogous to the law of mass action for conventional chemical reaction rates. For each vibrational energy level m, $\mathcal{R}_{mij}$ gives at a given temperature a clear vision of the kind of trajectory replenishing/depleting the number density ϕ_m. Figure 2.7 presents $\mathcal{R}_{mij}$ for the first 10 levels ($m = [0\ 9]$) at a temperature of 3000 K. Dark blue corresponds to a maximum depletion and dark red to a maximum replenishment over the global temperature range (2000 to 4000 K). The table is symmetric along the identity diagonal. A first observation is that all almost all cells located on the $i = m$ or $j = m$ lines are blue, *i.e.* collisions involving at least one molecule of level m usually result in a depletion of ϕ_m. At high levels ($m > 3$), depletion is usually maximum when both colliding molecules are initially on level m. On the other hand, it tends to be shifted towards the right/left of the $(i, j) = (m, m)$ cell for lower levels as inelastic collisions with a m molecule is more likely to occur when involving a partner at a higher level. This appears clearly when looking at the $m = 2$ table for instance. At 3000 K, a $(i, j) = (2, 2)$ collision is less effective at depleting ϕ_2 than $(i, j) = (6, 2)$ for instance. Interestingly, the ground state rates table is characterized by a positive production (red cell) for any neighbor of the $(i, j) = (0, 0)$ cell. Similarly, the highest replenishment rates are found for high levels ($m > 3$) in vicinity of the (m, m) cell on its diagonals. Logically, the fourth quadrant (both $i, j > m$) always have higher rates than the second quadrant (both $i, j < m$).

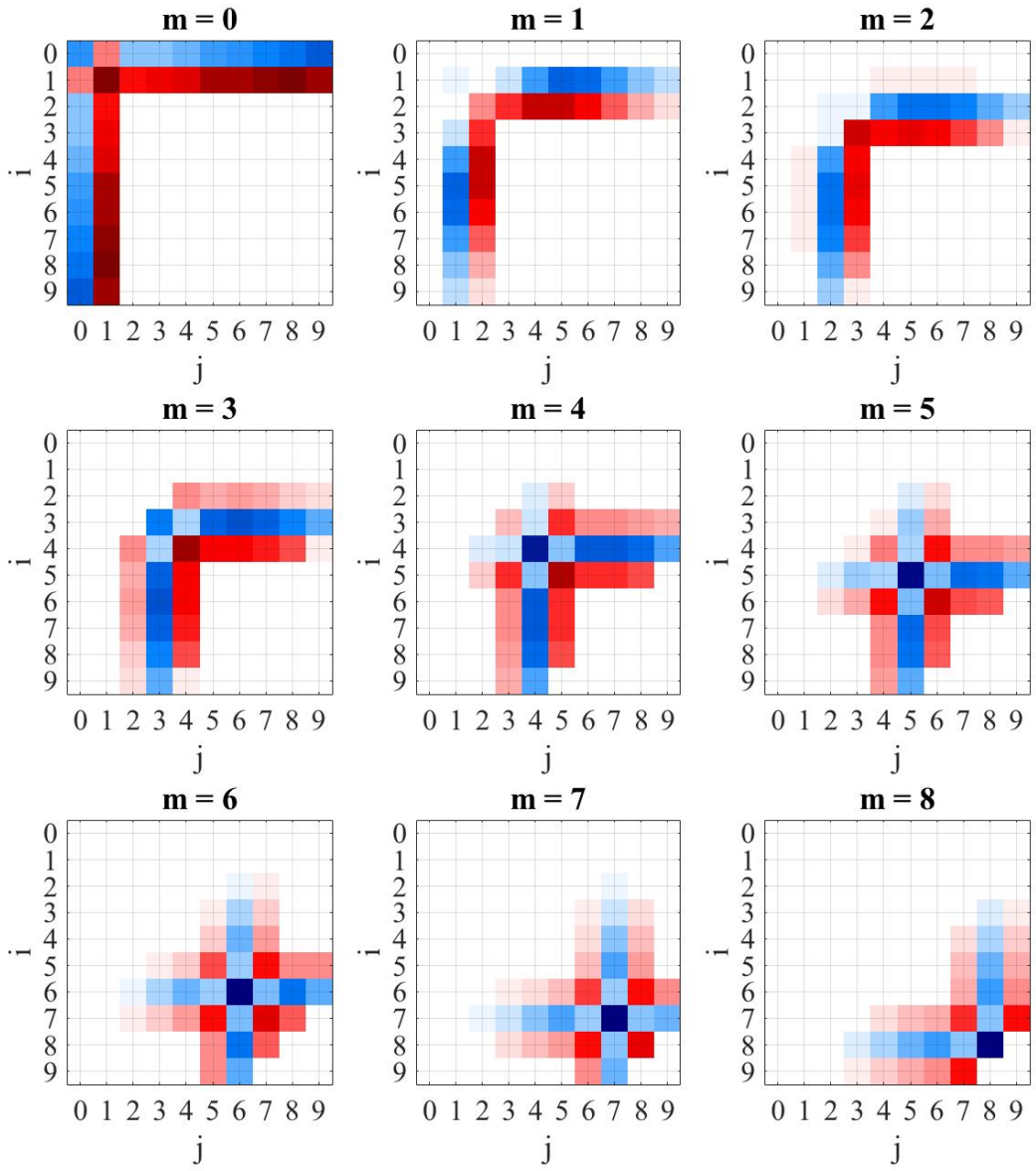

Figure 2.7: $\mathcal{R}_{mij}$ for the first 10 levels (m = [0 9]) at a temperature of 3000 K. Blue/red colors represent a population maximum depletion/replenishment rate.

2.2.3 Thermal bath simulations

In order to compare the QCT and LTMW models, the rates were used to simulate vibrational relaxation on N_2 in a 0D heat bath, hence at a fixed translational-rotational temperature T. The initial vibrational populations were set based on a Boltzmann distribution is

some T_v. Then, the solution was marched in time until the final vibrational state matched a Boltzmann distribution at the translational-rotational temperature T.

Figure 2.8 shows the normalized energy versus time for various bath temperatures and initial distribution temperatures. Interestingly, the relaxation process for all temperature combinations is well characterized by a Landau-Teller model [74] (i.e. exponential relaxation). The time to reach a final steady state is approximately independent of the initial distribution, regardless of the final temperature. This suggests the relaxation model can be parametrized by only the translational-rotational temperature, as done by Millikan and White [90].

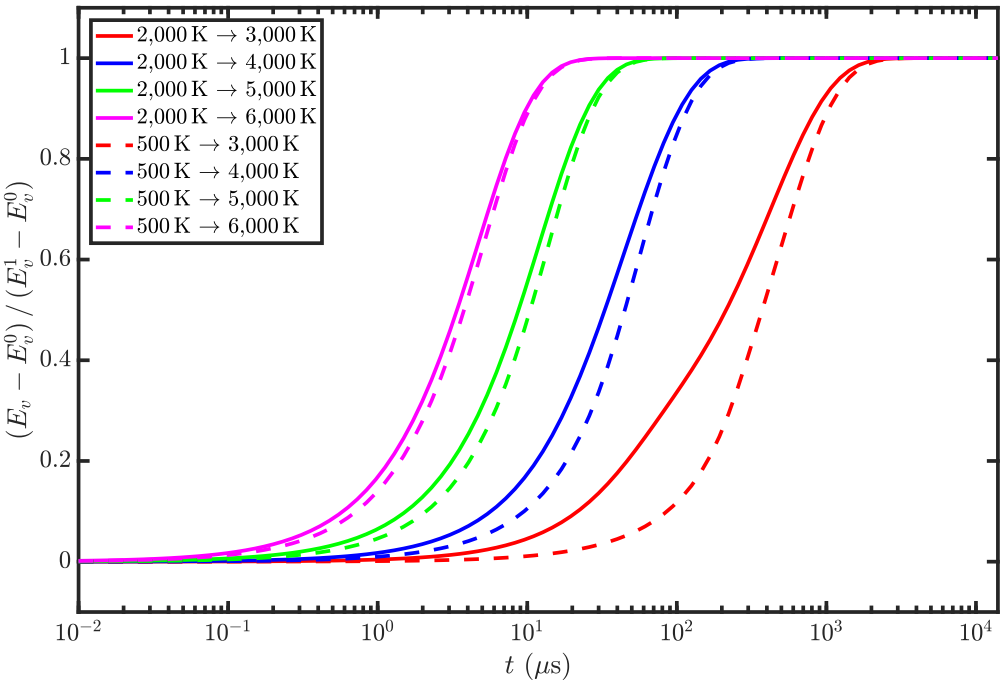

Figure 2.8: Vibrational relaxation profiles computed from QCT rates for different configurations and initial gradients.

A comparison of relaxation times computed from both the state-specific rates and Millikan and White correlations is presented in Fig.2.9 for various bath temperature. Both the post-compression and post-expansion relaxation processes were simulated. While Millikan and White's correlation was designed to capture the cold-to-hot process, it appears to be suited to evaluate expansion-triggered nonequilibrium as well. However, the results differ for the

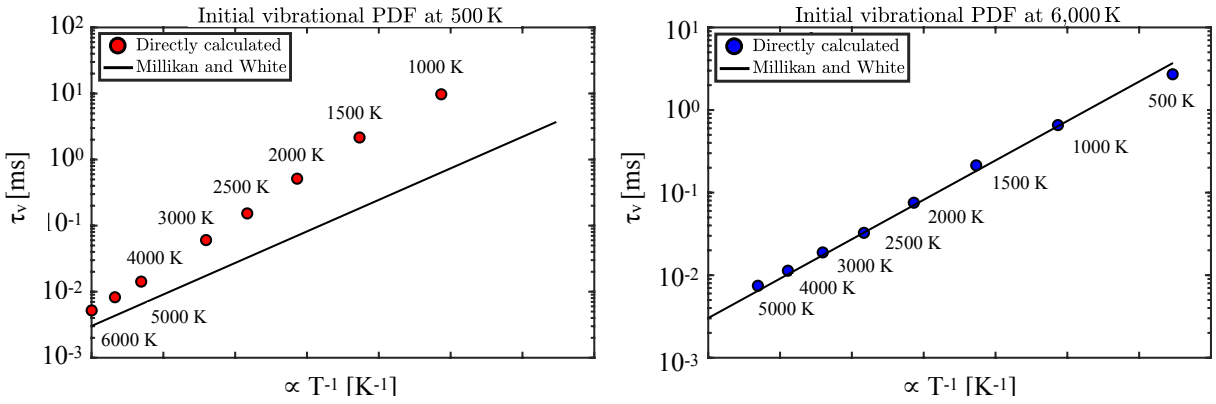

Figure 2.9: Comparison of the QCT relaxation rates and Millikan and White correlations for a (left) cold-to-hot and (right) hot-to-cold relaxation process.

post-compression simulations while other studies have confirmed that the LTMW multi-temperature model would accurately resolve such case [49, 12].

The differences between the models in the left figure (initial distribution at 500 K) can be explained by the inaccuracy of QCT at such low temperatures. Indeed, fewer transitions were observed at lower temperatures (resulting in fewer calculated rates) because the total energy of the colliding N_2-N_2 pair was not sufficient to dramatically shift the vibrational state. At high temperatures and vibrational quantum numbers, more energy is stored in translational-rotational and vibrational energy modes on average. This increases the total energy that can be repartitioned during the collision event, which in turn increases the likelihood of observing vibrational transitions. To illustrate the difficulty of observing transitions at low-lying vibrational states and at low temperatures, consider the transition from $(v_1 = 0, v_2 = 0)$ to $(v_1' = 1, v_2' = 0)$. For N_2, at 500 K the most probable rovibrational energy to be sampled is 0.165 eV, and the most probable translational energy to be sampled is 0.043 eV, corresponding to an initial total energy of 0.373 eV. Assuming that all translational-rotational energy can be converted into vibrational energy, there exists 0.079 eV of available energy. However, the energy difference between $v = 0$ and $v = 1$ is approximately 0.3 eV, so at this temperature, the translational-rotational energy is not sufficient to cause a transition. In contrast, using a similar analysis at 4,000 K, there exists 0.690 eV of translational-rotational energy,

which is sufficient to increase the vibrational energy from $v = 0$ to $v = 1$. Thus, it is far more likely that this transition will be observed. Indeed, the relaxation timescales converge towards Millikan and White's correlation as the bath temperature increase. Hence, the QCT algorithm will accurately evaluate the high-temperature inelastic collisional probability and is not suited to study low-temperature compression waves as present in scramjets.

2.2.4 Turbulent mixing with nonequilibrium

An aspect that has received little attention from the scientific community is how compressible turbulent mixing between high-temperature flows can trigger vibrational nonequilibrium as shown by Reising *et al.* [111, 112]. In scramjets, fuel-air mixing in the combustor or even boundary layer flows could trigger such nonequilibrium. Yet, it is unclear how the empirical LTMW model can resolve it. To address this concern, DNS of turbulent N_2 planar jets at temperatures over 2000 K (where QCT rates are accurate) were performed using both models. First, the QCT approach is used to elucidate the nonequilibrium mixing mechanics with great details. Then, the two models are compared.

Most of these results are presented in Fiévet *et al.* [38]. The focus and primary objective of this study was to investigate mixing-triggered nonequilibrium, and how the distribution distorts from a Boltzmann-like shape. The comparison with the LTMW model was only of secondary interest. Hence, more results of Fiévet *et al.* [38] are presented in App. A.

2.2.4.1 Numerical details

The planar jet has a height of 8 mm and is 1.6 cm wide, while the computational domain is 16 cm long. It is discretized using a structured grid system of $(n_x, n_y, n_z) = (3072, 960, 196)$ cells clustered around the core. The domain is periodic in the spanwise direction, and non-reflective characteristic boundary conditions are applied at all the non-streamwise boundaries of the domain. The plane jet inflow is a fully developed turbulent channel flow obtained from an auxiliary DNS with adiabatic walls. It possesses a 0.8 mm top and bottom boundary

Table 2.1: Numerical inflow conditions.

Case	U_{jet} [m/s]	U_{coflow} [m/s]	T_{jet} [K]	T_{coflow} [K]	$Re_{H/2}$
1	400	80	2000	4000	4600
2	400	80	4000	2000	1600

layer, and a 400 m/s core velocity, with a static pressure of 2.0 atmospheres and a static temperature of either 2000 (case 1) or 4000 K (case 2). The case 1 inflow Reynolds number based on the boundary layer height is $Re_\lambda = 1875$. The coflow is also at 2.0 atmospheric pressure, has a speed of 80 m/s and its static temperature is either 4000 (case 1) or 2000 K (case 2). The inflow density and temperature are simply rescaled from one case to the other. Both cases are presented in Tab. 2.1, but only the case 1 results are presented in this section. A comparative analysis of the two case yielding more insight on the turbulence-nonequilibrium coupling is given in App. A.

The simulations were performed using the two nonequilibrium flow solver presented in Sec. 2.2.1 and Sec. 2.2.2. Statistics were then sampled over 0.25 ms, which corresponds to 0.5 flow-through timescale τ_c based on the integrated centerline velocity in order to assess the time-averaged turbulence grid resolution. The simulations ran with a CFL number of roughly 0.9, giving a timestep of about 80 ns. The code uses domain-decomposition based parallelization, and each simulation was run on 10000 cores for 16 hours. An inert mixture fraction Z_{mix} was transported alongside the reacting first 10 vibrational state number densities ϕ_i. Z_{mix} allows us to observe how turbulent mixing tends to naturally bring the cell-averaged vibrational energy states distribution out of the equilibrium. A qualitative view of the computational domain and the turbulent mixing layer is shown in Fig. 2.10.

Figure 2.11 presents an instantaneous snapshot of the density gradient magnitude and streamwise velocity fields, revealing a highly turbulent mixing layer and post-potential core region. The turbulence is fully resolved as is shown in Fig. 2.12 when the local cell size is compared with the Kolmogorov lengthscale κ. When the local ratio between grid size and κ is below 2, all the turbulence energy spectra is theoretically resolved [109].

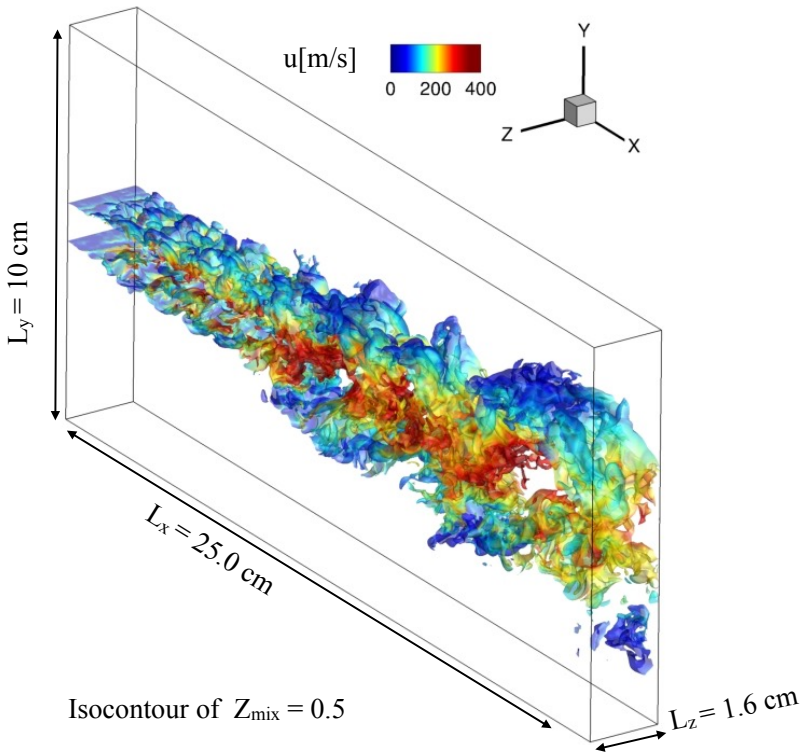

Figure 2.10: Isocontour of mixture fraction colored by streamwise velocity.

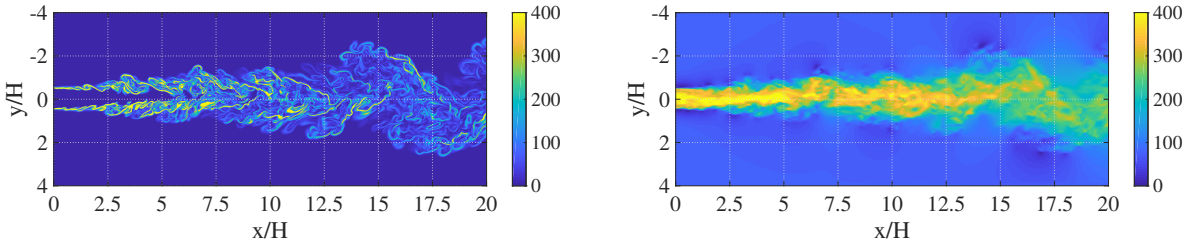

Figure 2.11: Snapshots of (left) Magnitude of density gradient in kg/m^2 of the N_2-N_2 planar jet and (right) contour of streamwise velocity U [m.s^{-1}].

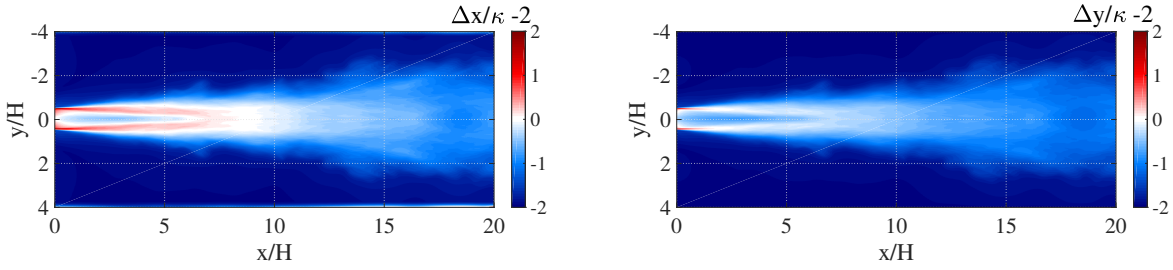

Figure 2.12: Spatial resolution in the (top) x and (bottom) y directions.

2.2.4.2 Bulk vibrational nonequilibrium in the mixing layer

First, the higher-order state-specific model is used to investigate how vibrational nonequilibrium is triggered by the turbulent mixing.

The flow bulk vibrational energy e_v is simply computed by integrating the energy across the 10 states populations. To quantify the presence of nonequilibrium, it is useful to define a state variable e_v^* as the vibrational energy the flow would have if it were at equilibrium. It is calculated such that the sum of the local internal energies is constant. In practice, an equilibrated temperature T^* which verifies that $e_v(T^*) + e_{tr}(T^*) = e_v(T_v) + e_{tr}(T)$ is obtained by Newton-Raphson scheme. e_{tr} is the sum of the gas translational and rotational energy (TRE). State variables $\cdot^*$ will often be used to assess the effect of nonequilibrium. The relative error between e_v and e_v^* computed as $\frac{e_v - e_v^*}{e_v^*} - 1$ quantifies nonequilibrium and is shown in Figure 2.13 (left) in percentage. The mixing layer is overwhelmingly vibrationally under-excited, with peak departure from equilibrium of around 5% from its equilibrated state. This is a surprising result, as the mass entrainment ratio (computed from Dimotakis [28]) equals 1.0: both cold and hot flow mix equally. In such case, Reising *et al.* [112] predicted that e_v should be symmetrically distributed across the mixing layer: the inner side, closer to the cold flow, should be vibrationally under-excited, while the outer layer should instead be vibrationally over-excited. Another theory is presented below.

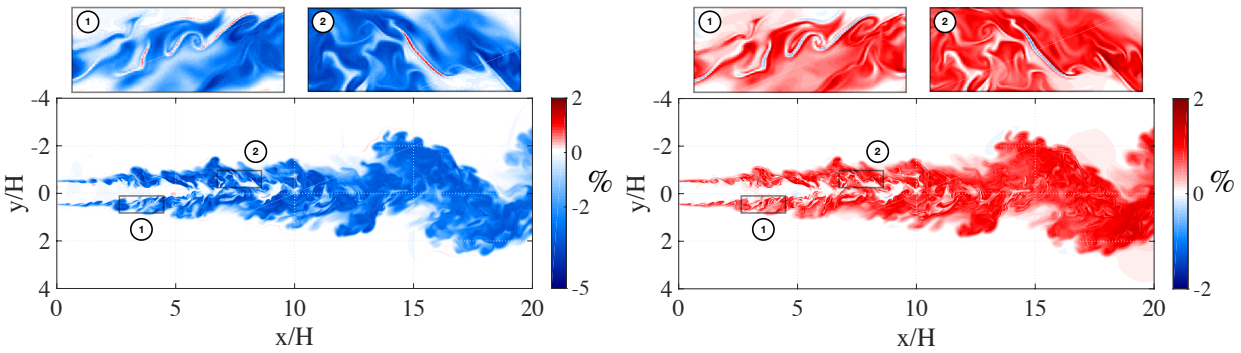

Figure 2.13: (Left) Snapshots of error between e_v and $e_v{}^*$ [%] for case 2. Red/blue colors indicate a locally vibrationally over/under-excited population. (Right) Snapshot of compressibility factor [%] for case 2. Red/blue indicate a locally compressed/expanded flow.

As the flow is mostly under-excited, T tends to be superior to T_v. Contrary to T_v which only changes through the slow Q_{T-V} energy exchange rate, T is coupled to the other thermodynamic variables through the compressible conservation equations. Hence, as the jet

flow slows down it interacts with the slower coflow and its local temperature instantaneously increases through compression. This happens at constant Z_{mix} as no mixing is needed to simply slow down a flow element emerging from the jet potential core. This means that T_v remains constant and that compressibility triggers nonequilibrium, in particular, cold nonequilibrium. Note that similarly the acceleration of the outer shear layer has the opposite effect and triggers hot nonequilibrium. However, instead of computing the mass entrainment ratio, the volume entrainment ratio is a better indicator of the surface area of slow hot coflow entrained, hence expanded. This time, it is equal to 2.1 which indicates the low-density jet dominates, and is therefore unable to entrain much of the higher-density coflow into the mixing layer. This result in an overwhelmingly cold compressibility-triggered nonequilibrium as the fast jet slows down. The following quantitative analysis is performed to support this theory. A compressibility factor is defined as the ratio between the local internal energy minus its vibrational component, *i.e.* simply c_vT, and the mixing of both sides *i.e.* $c_v(Z_{mix}T_{jet} + (1 - Z_{mix})T_{coflow})$. As the translational and rotational c_v is constant in our temperature range, this corresponds to a ratio of temperatures. In this ratio, c_vT includes the effect of compressibility, while the denominator does not. This compressibility factor is plotted in Fig. 2.13 (right). A positive value means the flow is locally compressed which should result in cold nonequilibrium. When comparing the right and left figures in Fig. 2.13 it appears to be remarkably consistent and correlated. Notably, the rare vibrationally hot areas coincide with the rare expanded areas. This is further quantified in Fig. 2.14 which presents the corresponding realizations of e_v against the mixture fraction on the left figure, and against the compressibility factor on the right figure. The color indicates the local concentration (blue is lowest, yellow is highest). It appears that most hot nonequilibrium occurs where the flow is expanded as predicted (top right quadrant in the left figure). Such hot nonequilibrium realizations tend therefore to occur in the close vicinity of the cold jet potential core, *i.e.* $Z_{mix} = 1$, as seen in the right figure. The larger the compression factor, the colder the nonequilibrium becomes (larger departure from local equilibrium). Note that as

most realizations populate the top left and bottom right quadrants, the e_v turbulent mixing profile could be symmetrical as predicted by Reising *et al.* [112] in absence of compressibility effects.

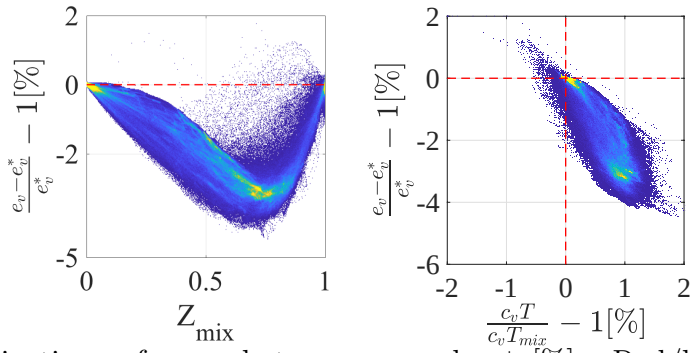

Figure 2.14: Realizations of error between e_v and $e_v{}^*$ [%]. Red/blue indicate a locally vibrationally over/under-excited population.

The same observation was made when using the LTMW model. The distributions of bulk e_v with the mixture fraction, presented in Fig. 2.15, compare well for both models. The linear mixing suggests that the relaxation timescales are in both case higher than the local turbulent mixing timescale.

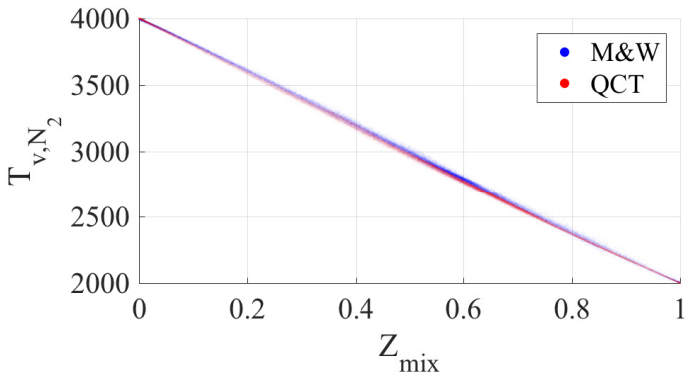

Figure 2.15: Comparison of the QCT relaxation rates and Millikan and White correlations for turbulent mixing of vibrational temperature.

2.2.4.3 Vibrational energy states distribution in the mixing layer

As the states populations mix, they fall out of equilibrium due to the equilibrium distribution being a nonlinear function of temperature.

Instantaneous snapshots of ϕ_1 and ϕ_9 are shown in Fig. 2.16. It can be seen that the overall mixing appears to be complex and dependent on the vibrational level. ϕ_9 appears to be dominated by the cold part of the jet while lower level populations like ϕ_1 seem to mix more evenly, similarly to Z_{mix}. This suggests that ϕ_1 relaxation process is slower than the mixing timescale, meaning the linear mixing process dominates. On the contrary, higher level 9 known to have the highest scattering rates (*i.e.* relaxation faster than mixing), the state population doesn't simply follow the same process. In general, the populations ϕ_i mix and relax towards their local equilibrium. Hence, they are bound by $\phi_i(T = 2000K)Z_{mix}+\phi_i(T = 4000K)(1 - Z_{mix})$ and $\phi_(T)$, as seen in Fig. 2.17 for the first 6 levels (the last 4 are similar with the 6^{th} one). The fast relaxing levels populations are distributed closer to their local equilibrium value, while the lower levels are more passively mixing and are closer to the simple mixture rule distribution.

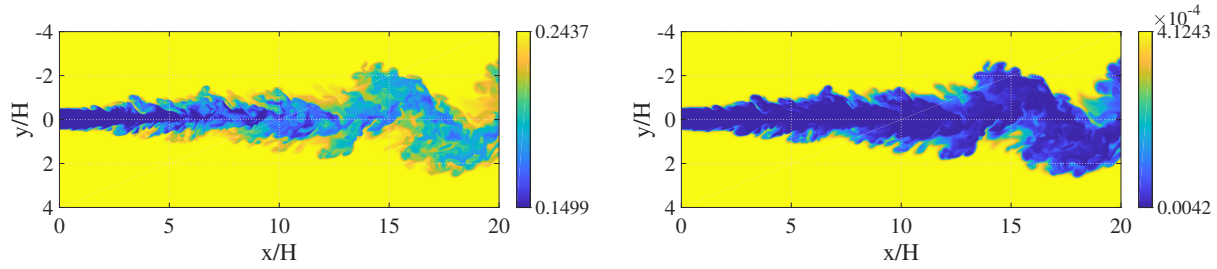

Figure 2.16: Instantaneous snapshots of vibrational state population number densities for levels $i = 1$ (left) and $i = 9$ (right).

As the ϕ_i do not mix uniformly, it is unlikely that the distribution remains Boltzmann-like throughout the shear layer. The integrated vibrational energy, e_v, corresponds to one unique Boltzmann distribution, called $\mathcal{B}_i(\mathrm{e_v})$. It is possible to evaluate how distorted from this Boltzmann distribution the states populations are throughout the mixing layer. To this end, an error $\mathcal{E}_i$ is defined as:

$$\mathcal{E}_i = \frac{\phi_i - \mathcal{B}_i(\mathrm{e_v})}{\mathcal{B}_i(\mathrm{e_v})}, \tag{2.24}$$

where $\mathcal{B}_i(\mathrm{e_v})$ is the number density of level i for a Boltzmann distribution yielding the

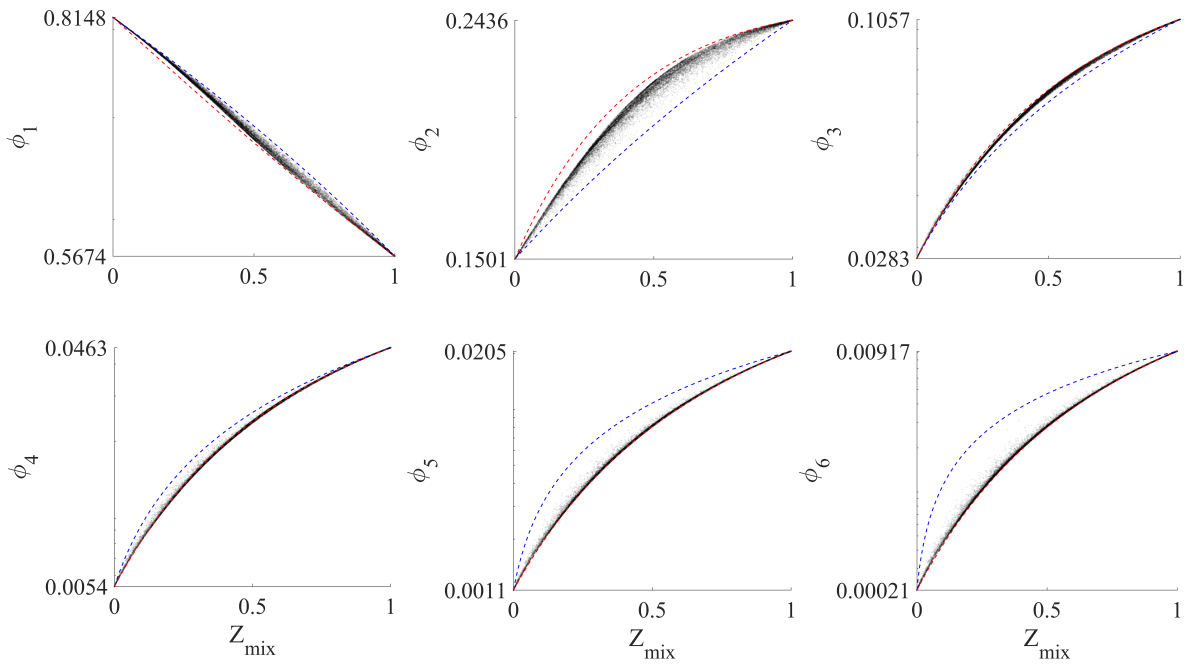

Figure 2.17: (Black dots) Distribution of state populations ϕ_i for $i \in [1\ 2\ 3\ 4\ 5\ 6]$ with (dashed blue) $\phi_i(T = 2000K)Z_{mix} + \phi_i(T = 4000K)(1 - Z_{mix})$ and (dashed red) $\phi_(T)$.

same bulk e_v.

Figure 2.18 shows the magnitude of $\mathcal{E}_i$ throughout the computational domain (left contour), along with its distribution with local mixture fraction Z_{mix} (right scatter plot). Only levels 1, 2, 3 and 9 are shown for the sake of conciseness, as levels 3 to 9 behave similarly. As i increases from 3 to 9, the higher $\mathcal{E}_i$ becomes. This indicates that these levels are locally over-populated. Level 1 is on the other hand slightly locally under-populated, which is consistent with the observation previously made from Fig. 2.13 showing a bulk under-excited vibrational energy e_v. According to the rates definition and thermal bath tests, the highest levels adjust faster than the lowest one to the local thermal equilibrium conditions. Hence, these levels rapidly relax towards the local equilibrium $e_v{}^*$ (shown to be overwhelmingly larger than e_v in Fig. 2.14) by increasing their populations. This results in a relative under-population of the slowly relaxing level 1. $\mathcal{E}_9$ high values are attributed to the large range of ϕ_9 throughout the mixing layer. This deforms the local distribution which becomes

non-Boltzmann. As a result, as the ground state is globally under-populated and the highest level is over-populated, one intermediary level presents a population inversion through the mixing layer. In this configuration, it happens to be state-level $i = 2$.

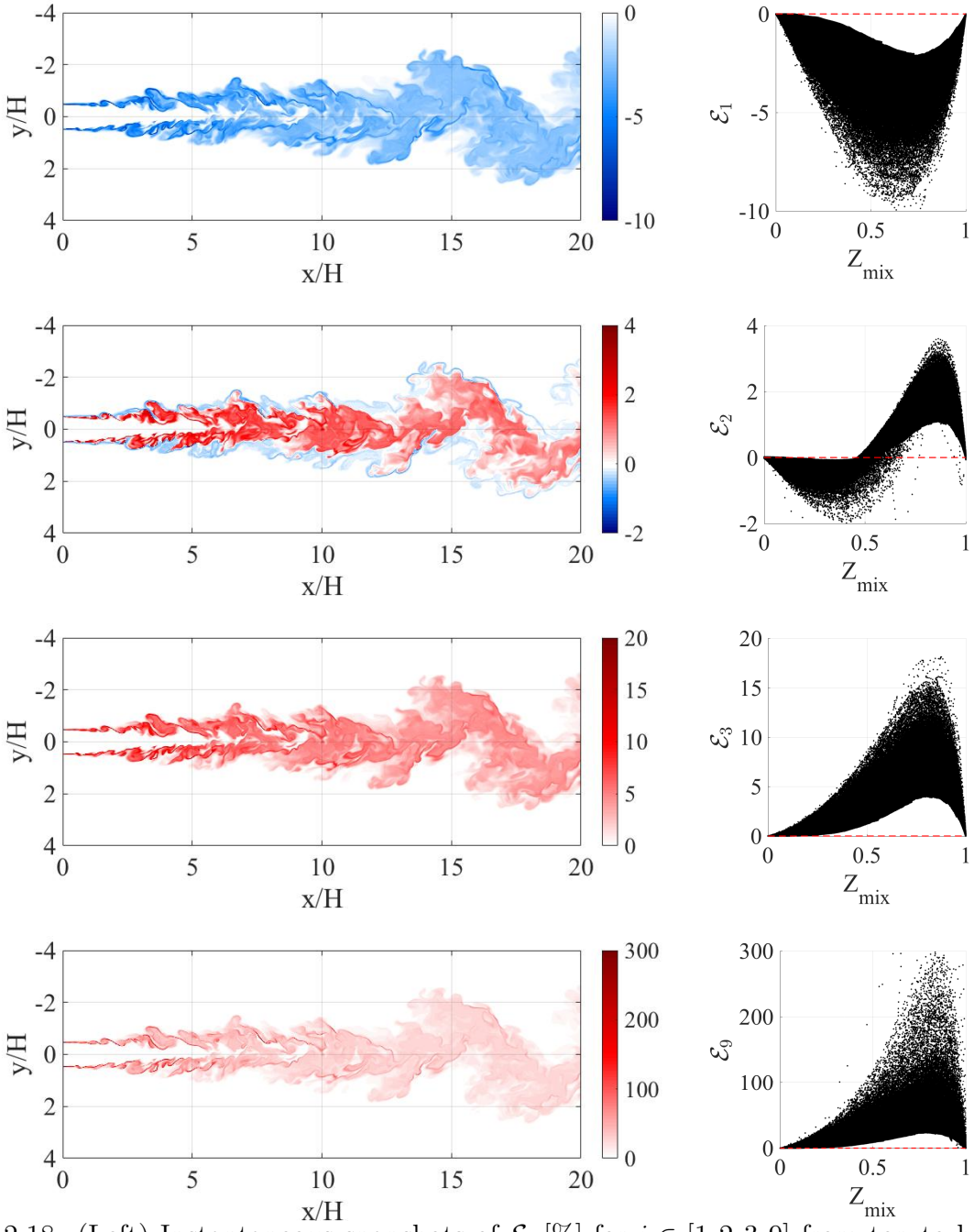

Figure 2.18: (Left) Instantaneous snapshots of $\mathcal{E}_i$ [%] for $i \in$ [1 2 3 9] from top to bottom. (Right) Realizations of $\mathcal{E}_i$ [%] for $i \in$ [1 2 3 9] from top to bottom with Z_{mix}.

2.2.5 Choice of nonequilibrium model

The multi-temperature approach using the LTMW relaxation rate model is designed to resolve the post-compression shocks nonequilibrium flow [90], and its accuracy was verified by additional studies [111, 49, 12]. The empirical correlation of Millikan and White holds surprisingly well on expanded gas too. Also, the bulk vibrational energy mixing process is captured as well as when using a state-specific model since, in both cases, the relaxation process of the dominant vibrational energy states is slower than the turbulent mixing process.

However, as is explained in Sec. 2.2.4.3, the high-lying energy states are overpopulated throughout the mixing layer as the slow-relaxing lower-lying states are underpopulated. Since chemical reactions are known to be more driven by the highly excited molecules [101] it means that a Boltzmann description of e_v will underestimate the effect of nonequilibrium on chemical reaction rates. Unfortunately, many PES are not available to this day to quantify the relaxation scattering rates of the many species involved in H_2-O_2 chemistry. The state-specific method would also require the transport of hundreds of scalars to resolve every species states populations, drastically increasing the computational cost compared the LTMW model. Moreover, the QCT rates overestimate the vibrational excitation time at low temperatures due to the low occurrence of inelastic collisions.

To conclude, the multi-temperature LTMW model will be used to investigate the effect of vibrational nonequilibrium on scramjet engines in the following chapters.

Lastly, it is possible to modify the chemical reaction rates as a function of at least T and reactants T_v, in an effort to account for bulk nonequilibrium on ignition. The derivation of such reaction rates is the focus of the next section.

2.3 Reaction rates with vibrational nonequilibrium

In order to study the effect of nonequilibrium on scramjets, it is essential that the chemical rates that describe the combustion process account for such effects. Much of the development

of nonequilibrium chemical rates have been for high-speed external flows [100, 64], and involves significant empiricism due to lack of reliable experimental data at such extreme conditions. Reaction rate expressions have been modified to account for nonequilibrium combustion [2, 72], but the models are subject to large uncertainty due to lack of validation data. It is important to note that the major impact of nonequilibrium will be on chain initiation and branching reactions since the presence of even small quantities of water vapor product will quench nonequilibrium swiftly [90]. In this sense, it is the ignition process that needs to be appropriately quantified, not the extinction.

An *ab initio* computational chemistry approach based on the same QCT algorithm used in Sec. 2.2.4.3 is used to derive nonequilibrium reaction rates for key hydrogen/air chain reactions in order to represent the combustion initiation process more accurately.

2.3.1 Efficiency function

The chemical source terms in Eqs. (2.4),(2.8) and (2.13) should take into account the local vibrational temperature. A simple approach is to use the equilibrium reaction rates (by which we mean the reaction rates computed at thermal equilibrium) but with an effective temperature that is a function of vibrational and translational temperatures [100]. However, this technique is known to have deficiencies even in high-temperature external flows [14, 83, 102]. An alternate approach is to define an efficiency function, $\varphi(T, T_v)$ that relates the equilibrium and nonequilibrium rates as

$$k_{\mathrm{qct}}(T, T_v) = \varphi(T, T_v) k_{\mathrm{eq}}(T), \tag{2.25}$$

where k_{neq} and k_{eq} denote the nonequilibrium and equilibrium rates, respectively. A 9-species 19-steps model [94] is used to compute the equilibrium rates. The efficiency function is then defined using the coupled vibration-chemistry-vibration (CVCV) model [64]. Recently, Voelkel et al. [130] directly obtained efficiency functions for key reactions in hydrogen combustion by performing QCT calculations using PES derived *ab initio* using computational

chemistry. These QCT-derived rates provide a more reliable estimate of the efficiency function. However, their validity directly depends on the quality and accuracy of the PES. In this work, the efficiency functions for the three main initiation reactions in hydrogen/air combustion, namely

$$\mathrm{H} + \mathrm{O_2}(T_{v,\mathrm{O_2}}) \rightarrow \mathrm{O} + \mathrm{OH} \tag{2.26}$$

$$\mathrm{O} + \mathrm{H_2}(T_{v,\mathrm{H_2}}) \rightarrow \mathrm{H} + \mathrm{OH} \tag{2.27}$$

$$\mathrm{H_2}(T_{v,\mathrm{H_2}}) + \mathrm{OH}(T_{v,\mathrm{OH}}) \rightarrow \mathrm{H} + \mathrm{H_2O}, \tag{2.28}$$

are based on the QCT results. All other reactions used the CVCV approach detailed in [64]. More details on the calculation of these efficiency functions are provided in [130].

Throughout the dissertation, reaction F1 will refer to $\mathrm{O_2} + \mathrm{H} \rightarrow \mathrm{O} + \mathrm{OH}$, reaction F2 will refer to $\mathrm{H_2} + \mathrm{O} \rightarrow \mathrm{H} + \mathrm{OH}$ and reaction F3 to $\mathrm{OH} + \mathrm{H_2} \rightarrow \mathrm{H_2O} + \mathrm{H}$. These are the 3 chain-branching reactions in the multi-step detailed chemistry model used from Mueller [94].

The efficiency functions of the theory-based rates are provided in Fig. 2.19 for fixed $T = 1300\,\mathrm{K}$ versus the T_v/T ratio. As can be seen, the efficiency function is highly dependent on both the reacting molecules and the chemical reactions. Interestingly, the reaction $\mathrm{H_2}(T) + \mathrm{OH}(T_{v,\mathrm{OH}}) \rightarrow \mathrm{H} + \mathrm{H_2O}$ (i.e. the vibrational energy of $\mathrm{H_2}$ and OH are sampled using T and $T_{v,\mathrm{OH}}$, respectively) shows very little sensitivity to one vibrational temperature, while the other reactions show a nearly linear variation in efficiency with vibrational temperature. Overall, the ratio T_v/T is the dominant factor in determining the efficiency function.

2.3.2 Reaction rates at conserved internal energy

Whenever the ratio of temperatures T_v/T is above unity, the efficiency function $\varphi(T, T_v)$ is also above unity, and vice versa. However, by bringing T_v over T at constant T, we have increased the gas internal energy. It is therefore not surprising to observe an increase in

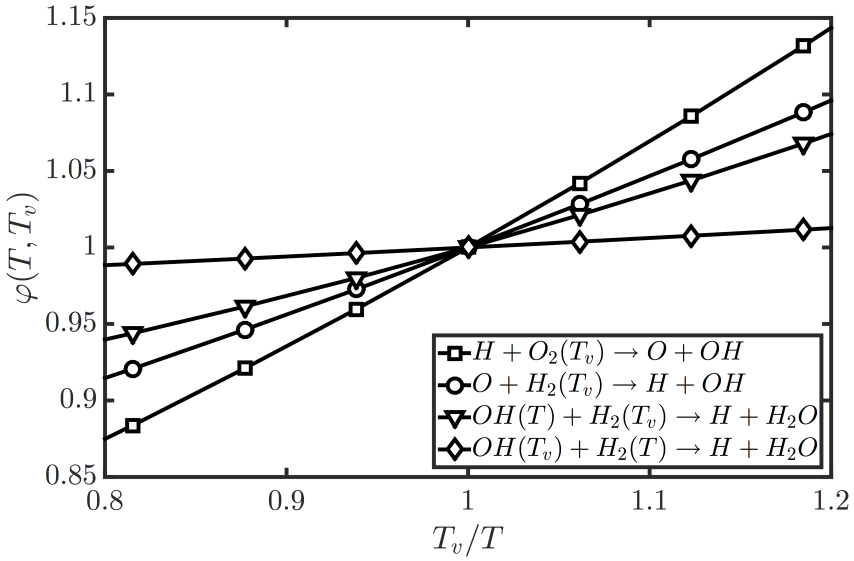

Figure 2.19: Efficiency functions plotted against T_v/T for $T = 1300$ K.

reaction rate. The analysis would be more relevant if performed at constant internal energy.

To quantitatively assess the real impact of nonequilibrium on reaction rates, it is useful to once again consider the equilibrated temperature T^* which was introduced in Sec. 2.2.4.2, which is defined as the equilibrium quantity obtained from the local sum of internal energies. The nonequilibrium reaction rates at thermal state (T, T_v) should be compared with the equilibrium reaction rates obtained at T^*. It is important to note that T^* is always in between T and T_v, following the principle of communicating vessels. Hence, the overall ratio $k_{\text{qct}}(T, T_v)/k_{\text{eq}}(T^*)$ depends strongly on the reaction rate pre-exponential factor n in the Arrhenius expression $k = AT^n \exp\big(-\frac{E_a}{R_u T}\big)$. For low values of n, such as the first chain-branching reaction $\text{H}+\text{O}_2(T_{v,\text{O}_2}) \rightarrow \text{O}+\text{OH}$ (n=0), $T_{v,\text{O}_2} > T$ fastens the reaction through the efficiency function $\varphi - F1(T, T_{v,\text{O}_2})$. Figure 2.20 (left) shows the equivalent T^* of a pure O_2 gas at various T and T_v. Figure 2.20 (right) shows the resulting ratio $k_{\text{F1,qct}}(T, T_v)/k_{\text{F1,eq}}(T^*)$ for the forward reaction. For large values of n, it might be more profitable to have $T_v < T$. This is typically the case for the second chain-branching reaction $\text{O} + \text{H}_2(T_{v,\text{H}_2}) \rightarrow \text{H} + \text{OH}$ which has $n = 2.67$. Figure 2.21 shows that, this time, the ratio $k_{\text{F2,qct}}(T, T_v)/k_{\text{F2,eq}}(T^*)$ depends on the local translational temperature. At low temperatures, the efficiency function

is predominant. However, above 1200 K, such as in scramjet combustors, the differential between T and T^* becomes large enough such that the T^n counter-balances the effect of the efficiency function. At temperatures higher than 1600 K, it becomes more profitable to have a vibrationally cold gas from a kinetic point of view.

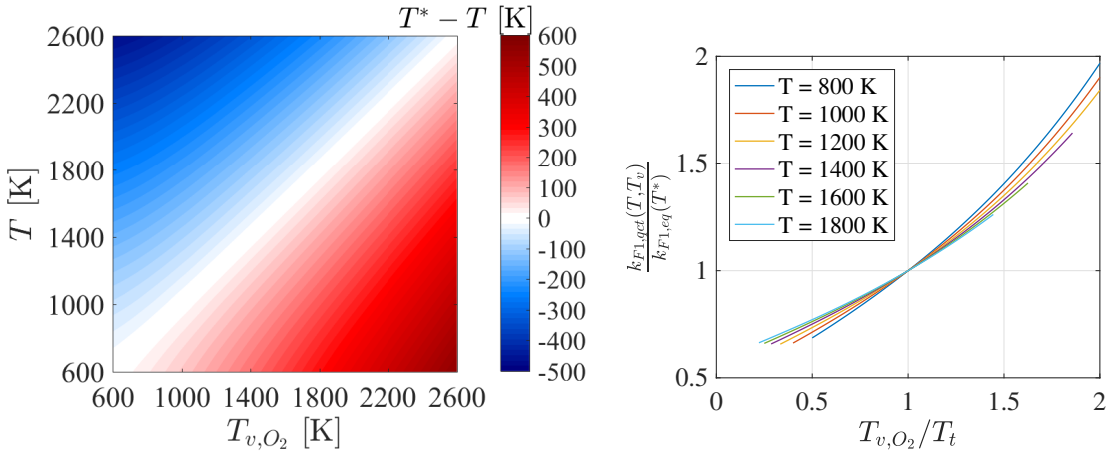

Figure 2.20: (Left) Difference between local temperature T and equilibrated temperature T^* for various thermal states of O_2 gas. (Right) Ratio between $O_2 + H \longrightarrow OH + O$ reaction rate at various thermal states and their corresponding equilibrated state.

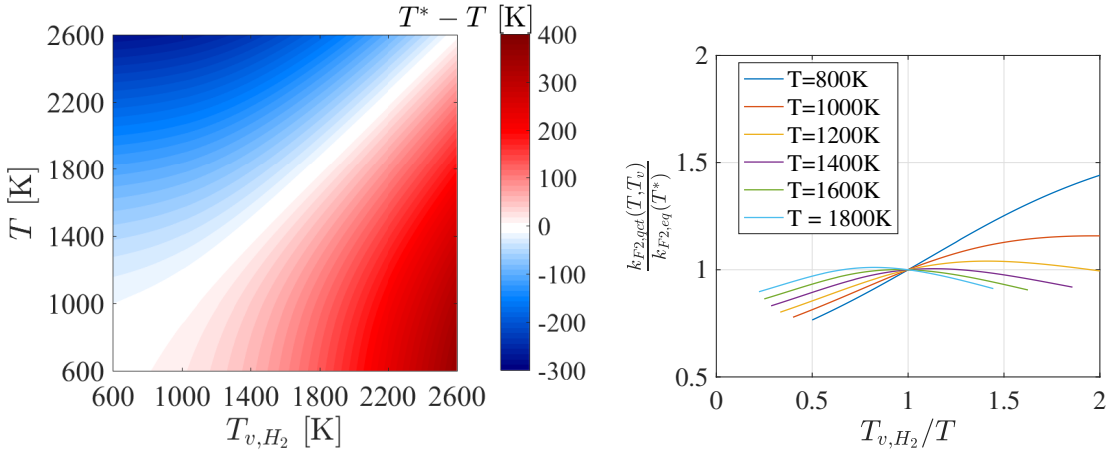

Figure 2.21: (Left) Difference between local temperature T and equilibrated temperature T^* for various thermal states of H_2 gas. (Right) Ratio between $H_2 + O \longrightarrow OH + H$ reaction rate at various thermal states and their corresponding equilibrated state.

2.3.3 Influence of diluter N_2 as a thermal sponge

The analysis Sec. 2.3.2 just showed how the effect of the pre-exponential factor can lead to counter-intuitive results. There is another important variable to consider. In an

air-breathing engine, the reacting species are typically outnumbered by the diluter N_2. This non-reacting species relaxes very slowly (see Fig. 2.5), and can be considered as a thermal sponge in the following sense. In a N_2 and H_2 mixture of 4 moles to 1, the impact of the dominant species' vibrational temperature T_{v,N_2} on T^* is more important than T_{v,H_2}. Figure 2.22 is equivalent to Fig. 2.21 with the addition of 4 moles of diluter N_2. The thermal state is now described by 3 temperatures. This additional degree of freedom can create situations where $T_{v,N_2} < T$ and $T_{v,H_2} > T$ which results in both $T^* < T$ and $\varphi(T, T_{v,H_2}) > 1$, hence a large $k_{\mathrm{F2,qct}}(T, T_v)/k_{\mathrm{F2,eq}}(T^*)$ ratio. On the other hand, having a vibrationally cold H_2 population in a bath of vibrationally hot diluter N_2 would drastically decrease the reaction rate. Likewise, this can occur for the first reaction.

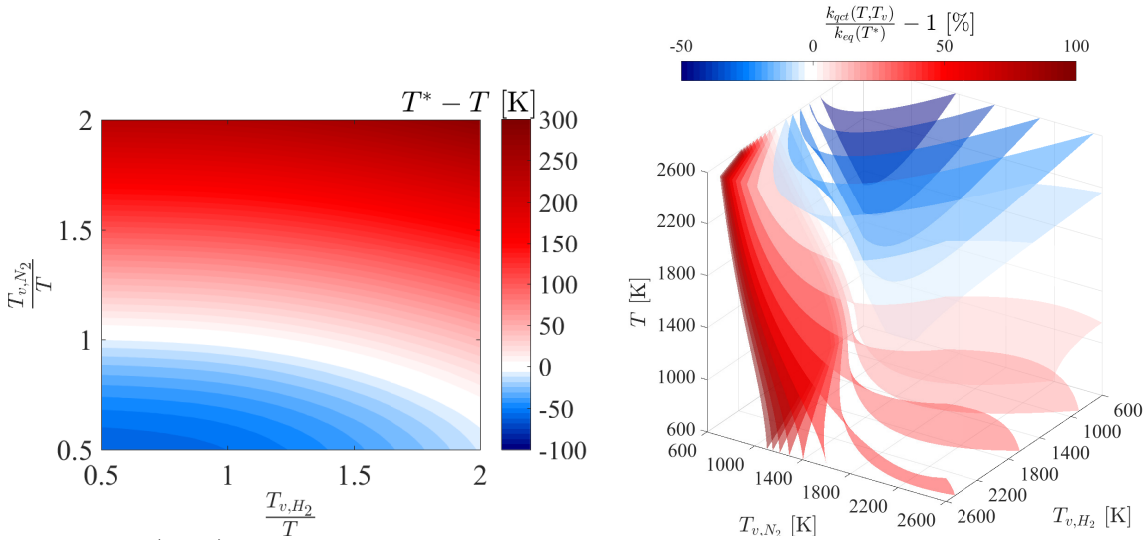

Figure 2.22: (Left) Difference between local temperature $T = 1200$K and equilibrated temperature T^* for various thermal states of N_2-H_2 gas (4/1 moles). (Right) Ratio between $H_2 + O \longrightarrow OH + H$ reaction rate at various thermal states and their corresponding equilibrated state.

Every species can, therefore, have an effect on a particular reaction: even if it is not reactive, its vibrational energy affects the translational temperature. In a realistic ignition scenario, the three species N_2, O_2 and H_2 would be present. Such configuration is shown in Fig. 2.23 for a fixed temperature $T = 1200$ K. The left surfaces again shows the gradient $T^* - T$ in Kelvin while the right surfaces show the product of first two chain-branching

reaction rates. It can be see that under favorable conditions $T_{v,\mathrm{N}_2} < T$, $T_{v,\mathrm{O}_2} > T$ and $T_{v,\mathrm{H}_2} > T$ ignition is considerably enhanced. If such conditions are met inside a ram/scramjet combustor, nonequilibrium would have drastic effects on the engine performance.

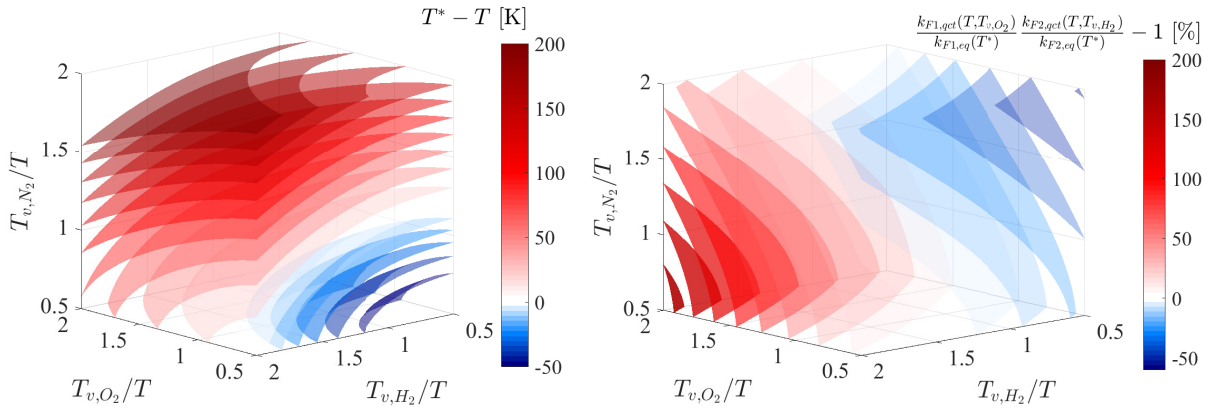

Figure 2.23: (Left) Difference between local temperature T and equilibrated temperature T^* for various thermal states of N_2-O_2-H_2 gas (4/1/1 moles). (Right) Ratios between various thermal states and their corresponding equilibrated state of products of first and second chain reactions shown in Figs. 2.20 and 2.21.

2.4 Chapter conclusions

A compressible flow solver using shock-capturing scheme has been modified to resolve the vibrational energy relaxation process using a multi-temperature approach. The vibrational energy relaxation rates are computed using the Landau-Teller model with Millikan and White's empirical correlation for the relaxation timescale. This model is capable of resolving the post-compression, post-expansion, and mixing-triggered nonequilibrium in a satisfactory way. In the future, a state-specific approach will permit to resolve nonequilibrium and reaction rates with greater accuracy. The effect of bulk vibrational nonequilibrium on chemistry is modeled using a corrective factor which is a function of the reactants vibrational temperatures. This factor was determined using quantum calculations. Overall, the numerical solver is now well-equipped to investigate the effect of vibrational nonequilibrium on scramjets.

CHAPTER III

Numerical investigation of shock train sensitivity to inflow boundary layer variations

The primary objectives of this chapter are to investigate the shock train sensitivity to changes of inflow confinement ratio and to verify the ability of the solver to resolve pseudoshocks. To this end, a shock train experiment is simulated using DNS. The solver is shown to be able to correctly capture the experiment wall pressure profile and replicate the shock train structure. The energy conversion process is also quantified revealing the importance of turbulent work and the inherent weaknesses of RANS to simulate shock trains. The inlet boundary layer momentum thickness is then varied while the bulk inflow and outflow conditions remained constant. The simulations show that the shock train is displaced upstream as the inflow confinement ratio increases. Also, an increase in boundary layer momentum thickness results in a reduction of the normal-like portion of the lambda-shock structures in the channel core. This leads to more numerous but weaker bifurcating shocks as well as an increase of the shock train length. When the inflow boundary layer thickness is varied temporally, the complex shock train response depends on the excitation frequency. A resonance frequency is observed when different components of the shock train exhibit the highest amplification in terms of pressure-jumps. Further, the domain upstream of the leading shock acts as a low-pass filter, which has the end result of limiting the axial shock train motion. Nevertheless, even a small oscillation in boundary layer momentum thickness of 0.45 mm (0.6% of the channel height)

is seen to increase the shock train length by two orders of magnitude (4 cm). Most of this work was published in Fiévet *et al.* [33].

The chapter is organized as follows:

- Sec. 3.1.2 discusses the flow configuration and numerical details.
- Sec. 3.2 presents the results on the effect of boundary layer thickness on shock train evolution, as well as a comparison with experimental data.
- Sec. 3.3 decomposes the conversion process of kinetic into internal energy.
- Sec. 3.4 is dedicated to temporal effects on shock train motion, as the inflow boundary layer momentum thickness oscillates at different frequencies. In particular, the role of the shock train in processing upstream disturbances is analyzed in detail.

3.1 Configuration of the numerical simulations

3.1.1 Flow configuration and computational domain

The simulation configuration is chosen to replicate the University of Michigan expansion tunnel facility, where an experimental study on the effect of back pressure variations on shock train behavior has been conducted [62, 63, 51]. The simulation domain consists of a 69.8 $\times$ 57.2 mm constant-area rectangular channel to which a back pressure is applied at the outlet as a numerical boundary condition. Figure 3.1 presents a qualitative view and some perspective of the computational domain and typical flow structures. The inflow is at Mach 2, and is injected as a turbulent channel flow at pressure P_{in}. The outflow back pressure P_{out} is fixed to 46200 Pa corresponding to about 70% of a normal shock pressure rise for this Mach number. The channel half-height, $h = 34.9$ mm, is used as a reference length throughout the chapter. The computational domain spans 856 mm in the streamwise direction (roughly $25h$), which is sufficient to fully accommodate the shock train for the range of conditions studied here. The domain is discretized using an orthogonal grid system

of various resolutions as detailed in Tab. 3.1. The grid cells are clustered near the walls such that the spatial resolution based on wall units is $\{\Delta x+ = 12.6,\ \Delta y+ = 0.69 - 14.7,\ \Delta z+ = 0.69 - 14.7\}$. The wall viscous length scale was computed to be 22μm based on the inflow boundary layer statistics shown in Fig.3.2.

3.1.2 Inflow generation

As previously discussed, the focus of this study is to understand the impact of inflow boundary layer conditions on shock train formation and response. For this purpose, three different inflow boundary layers generated from an auxiliary channel flow simulation are used. The inflows are generated from an auxiliary simulation on the same domain as the main channel simulation, but without a numerical back pressure. The domain has streamwise periodic boundary conditions, which simplifies boundary layer development, and a grid resolution of $\{\Delta x+ = 17.7,\ \Delta y+ = 0.95 - 20.6,\ \Delta z+ = 0.95 - 20.6\}$. Starting from a uniform flow, the governing equations are evolved using a 4^{th} order Runge-Kutta temporal scheme, 6^{th} order compact scheme for spatial discretization, and an 8^{th} order implicit filter with hyperviscosity. The turbulent boundary layer grows to the target height, at which point the flow field is sampled with planes of data written to a data file. Since the turbulent boundary layer grows during this time, the data is collected only for a short time of 1/4 flow-through times. This approach allows inflow data that is continuous in space and time (within numerical accuracy) to be generated. Further, no numerical shocks are observed in the main simulation, which can arise from discontinuous inflow conditions that are patched in time. The inflow conditions and the corresponding parameters are shown in Tab. 3.2. The resolution was carefully chosen such that no extraneous compression shocks are generated at the inlet due to a mismatch between the isolator and channel computational grids. Figure 3.2 presents the wall-normal time-averaged velocity and turbulence intensity profiles for all inflows. It is seen that the Van Driest transformed velocity profiles are similar to conventional incompressible turbulent boundary layer flows, which is a known result [84] and

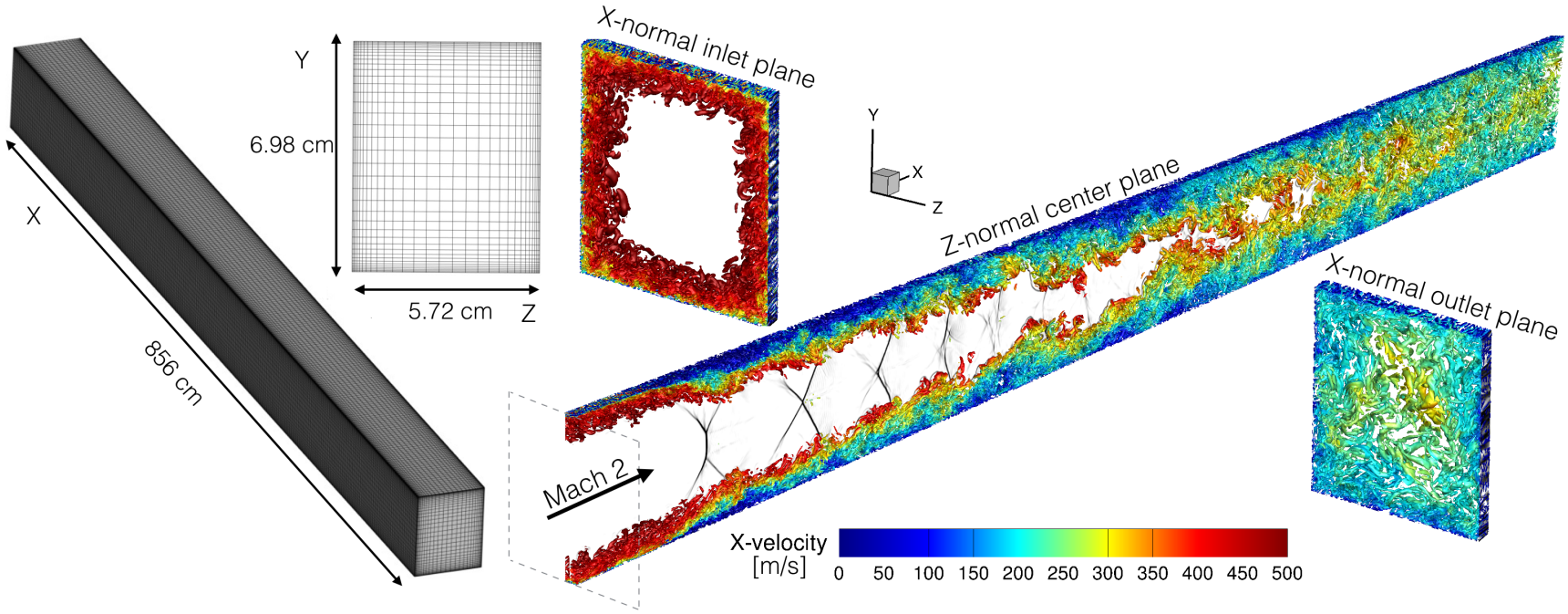

Figure 3.1: (Left) Computational domain and grid with 1/8th cells in each direction. (Right) Iso-contours of second-invariant of the velocity gradient tensor colored by streamwise velocity with density gradient in black.

Table 3.1: Different grid resolutions used for the shock train DNS.

Grid	N_x	N_y	N_z	$\Delta x+$	min $\Delta y+/\Delta z+$	max $\Delta y+/\Delta z+$	Cells <10y+
$R1$	1024	160	128	35.4	1.90	41.2	4
$R2$	2048	320	256	17.7	0.95	20.6	8
$R3$	3072	480	384	12.6	0.69	14.7	13

Table 3.2: Flow conditions for the three different inflow considered

Case	$P_{in}[kPa]$	$T[K]$	Ma	$\delta[mm]$	δ/h	δ^*/h	$\theta[mm]$	Re_θ
A	14.1	170.0	1.97	8.8	0.25	0.046	1.3	4530
B	14.5	171.0	1.97	9.8	0.28	0.070	1.8	6380
C	14.8	172.0	1.96	11.9	0.34	0.083	2.2	7900

compares well with similar flows in the literature, such as the Mach 2.32 and $Re_\theta = 4450$ DNS of Martin [84]. Likewise, the wall-normal density-weighted Reynolds stresses profiles at the bottom wall compare favorably well with other profiles in the open literature considering the differences in viscosity, Mach and Reynolds numbers [84, 106, 91, 114]. Closer to the corners, the interaction of the boundary layers will cause the profiles to differ from the conventional log-law profiles. Note that the friction coefficient measured at the center of the bottom wall (y=0 and z=0) is constant for all inflows at 0.00105.

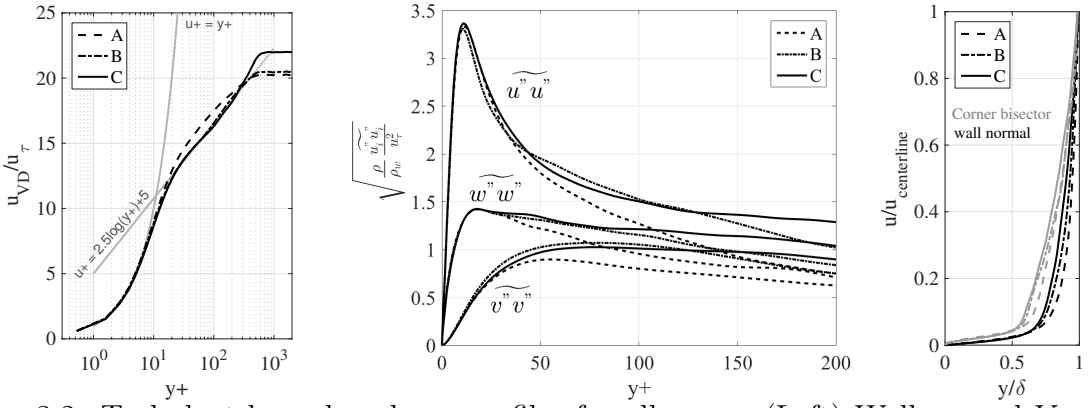

Figure 3.2: Turbulent boundary layer profiles for all cases. (Left) Wall-normal Van Driest transformed velocity profiles and (middle) wall-normal density-scaled turbulence intensity profiles and (right) corner bisector and wall-normal Reynolds-averaged velocity profiles.

3.1.3 Numerical details

The simulations were performed using the in-house compressible flow solver UTComp presented in Chap II. In this chapter, the viscosity is determined using Sutherland's law and is multiplied by 4 to obtain a more tractable Reynolds number. It is estimated that using standard air viscosity would bring the wall unit down to about 9μm, increasing the computational costs by a factor of 36 and requiring 8.2 billion cells grid to achieve the same resolution. The thermal diffusivity is obtained using a constant Prandtl number of 0.72. Further details on the flow solver are provided in Sec. 2.1. The walls are treated adiabatically as the recovered wall temperature is estimated to be very close to the room temperature[1]. Each case was initialized on grid R1 with respective inflow conditions in the first half of the channel, and post pressure-rise conditions in the second half. Each case was computed until a stable shock train was constructed: its position along the channel was observed to be fully converged over $30\tau_c$. Each case was then interpolated on grid R2 and further ran on 4000 cores for 120 hours over $8\tau_c$. During the R2 run, the shock train became unsteady for all cases. It first relaxed downstream, slowed down, then moved steadily upstream at a constant velocity of 1.5% mean centerline velocity. The shock trains were then interpolated on grid R3 and ran for an additional 24 hours on 8000 cores over $1.5\tau_c$. Statistics were then sampled over 0.5 ms on R3, which corresponds to a quarter of a flow-through timescale τ_c ($\tau_c = 2.05$ ms) based on the integrated centerline velocity, or one inflow period. Although every simulation ran over multiple τ_c, it was found that sampling statistics over a longer time would decrease the shock resolution due to the unsteady position of the shock train. The simulations ran with a Courant-Friedrichs-Lewy number of 0.9, giving a timestep of about 32 ns for the finest grid.

[1]Discussion with Dr.Hunt

3.1.4 Validation of simulation accuracy

3.1.4.1 Grid convergence

A grid convergence analysis was performed with conditions corresponding to case B and is shown in Fig.3.3. Time-averaged profiles for the stable R1-grid sampled over the whole run ($30\tau_c$, *i.e.* >0.06s) are also shown. The relative L2-norm error of R1 and R2 wall pressure profiles with respect to R3 are 2.01 and 0.32%. The convergence from R2 to R3 of both wall and centerline pressure profiles are excellent. Interestingly, even the coarsest grid (R1) reproduces the bulk of the physics by resolving most shock cell sizes and location, as well as capturing the time-averaged wall pressure growth rate. However, R1 is unable to correctly resolve the leading cell's compression and expansion wave strengths. The under-resolution of the successive compression/expansion cycles leads to a roughly 3-4 h shorter shock train based on the pressure time-averaged profiles. The R3 simulation achieves both convergence and meets the resolution requirement for a wall-confined DNS [133] : $\Delta x+ < 15$, $min(\Delta y+) < 1$ and at least 3 cells included within a distance of 10y+ from all walls (in our case, the spanwise direction z+ is also a wall-normal direction with similar resolution). In fact, the maximum $\Delta y+/\Delta z+$ throughout the inlet boundary layer are 6.9, 7.6 and 8.8 y+ for cases A, B and C respectively. The R3 simulation will be referred to as a DNS throughout the chapter.

3.1.4.2 Comparison with experimental data

Additionally, in order to ensure that the simulations capture the general trends observed in the experiments, direct comparison with the experimental data of Klomparens *et al.* [62, 63] is presented here. Figure 3.4 shows the time-averaged DNS pressure profiles compared with experimental measurements. In these plots, $P_0 = P(x_0)$ denotes the pressure on the lower wall at the location x_0 preceding the location of shock-triggered pressure rise. In the experiment, the shock train inflow confinement ratio is increased/decreased by displacing

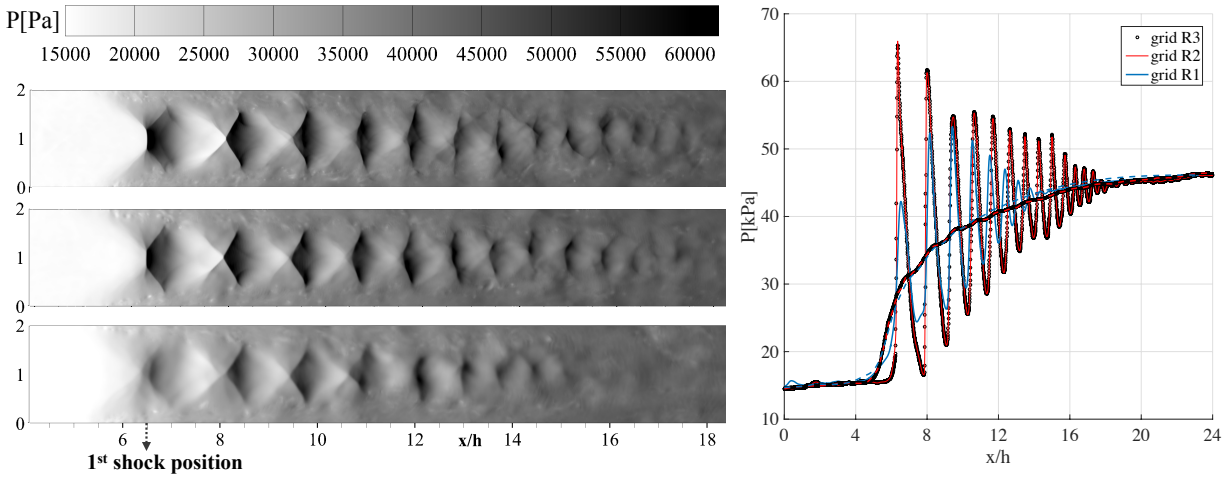

Figure 3.3: (Left) Typical static pressure snapshots for grid R3, R2 and R1 (top to bottom). (Right) Centerline (solid) and wall (dashed) time-averaged static pressure profiles for all grids.

the train downstream/upstream in the tunnel. This motion is achieved by changing the back pressure ratio through a control valve downstream. From the available data, case B is the closest to the experimental conditions : $\delta/h = 0.27$ for both and $P_{out}/P_{in} = 3.17$ and 3.18 for the experiment and the DNS respectively. It should be noted that due to the artificial increase in viscosity in the simulations, the inflow momentum thickness is larger in the experiments for the same confinement ratio. The bump observed in the experimental profile around $(x - x_0)/h = -1$ is an uncanceled wave from the nozzle expansion process. As seen in Fig. 3.4, the simulations compare well with experiments. Even so, there is a steeper pressure rise in the simulation compared to experiments. This is consistent with other simulation data (Morgan *et al.* [91], Roussel *et al* [114]) also. One possible reason is the time duration of averaging. In the experiments, the data was averaged over a few seconds, over which low-frequency oscillations of the shock-structure were observed. The simulations were averaged over a much shorter time on the order of a millisecond. The low-frequency oscillations were observed to have a broad spectral response, with a frequency between 90-120 Hz. It is likely that these oscillations act as a moving bandwidth averaging filter, leading to a more gradual pressure rise in experiments compared to the simulations.

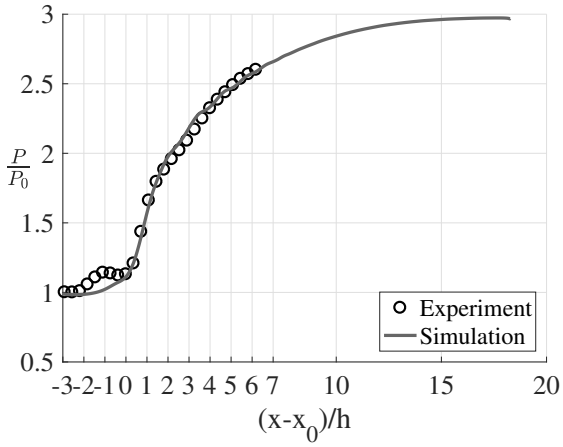

Figure 3.4: Time-averaged pressure profiles along the wall from simulation and experiment for case B.

3.2 Effect of inflow boundary layer thickness

3.2.1 Instantaneous snapshots

The three cases (A, B, and C, see table. 3.2) were simulated using the procedure described in Sec. 3.1.2. Figures 3.5 and 3.6 show the DNS instantaneous Mach number and density gradient magnitude contours for all cases on the center plane in the spanwise direction. Similar to experimental predictions, a series of shock structures is present. Once the primary shock is formed, the boundary layer thickens, leading to an increasing volume of subsonic flow with axial distance. Note that the density gradients across the shock structure are roughly equal for all cases, indicating that the growth of the subsonic region plays a bigger role in affecting the axial compression rate. Past the terminating (last) shock, a mixing region is observed, where both subsonic and supersonic flows are present. Overall, the simulation reproduces the essential features of a shock train. The observed trend is that a higher confinement ratio moves the shock train upstream.

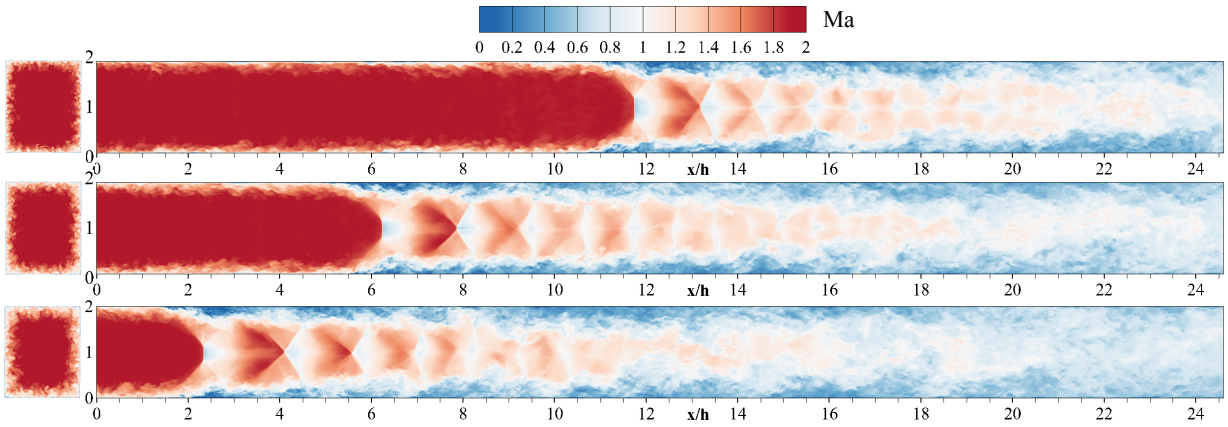

Figure 3.5: Instantaneous snapshots of Mach number for (top) case A, (middle) case B and (bottom) case C with the inlet plane on the left side.

3.2.2 Shock train structure dependence on convective velocity

The equilibrium location of the shock train changed when interpolating from the coarse grid R1 to the finer grids R2 and R3, and all shock trains started moving. The equilibrium position of the shock train depends on the balance between the back pressure force (which pushes the shock train upstream) and the wall shear stress (which attaches the shock train to the wall). Since the boundary layer is better resolved on the finest grids, that location is subject to change during grid refinement. When interpolating from grid R1 to R2, we observed a slow steady displacement upstream of the shock train for case B. For cases A and C, the shock train first relaxed downstream, slowed down, then moved steadily upstream. These low-speed and large-scale displacements from the previous R1 steady location existed for many flow-through times over the whole R2-simulation as seen in Fig.3.7. The shock train is still steadily moving upstream by the end of the R2 and R3 simulations, with a converged convective speed comprised between 7 to 9m/s, which corresponds to about 1.5% of the bulk inflow velocity. Consequently, even with the long simulation times considered here, the statistics cannot be assumed to be fully converged since very low-speed dynamics may not have been completely considered. Hence, as mentioned in Sec.3.1.2 the DNS statistics are sampled over 0.5ms, which corresponds to a quarter of a flow-through timescale τ_c (τ_c =

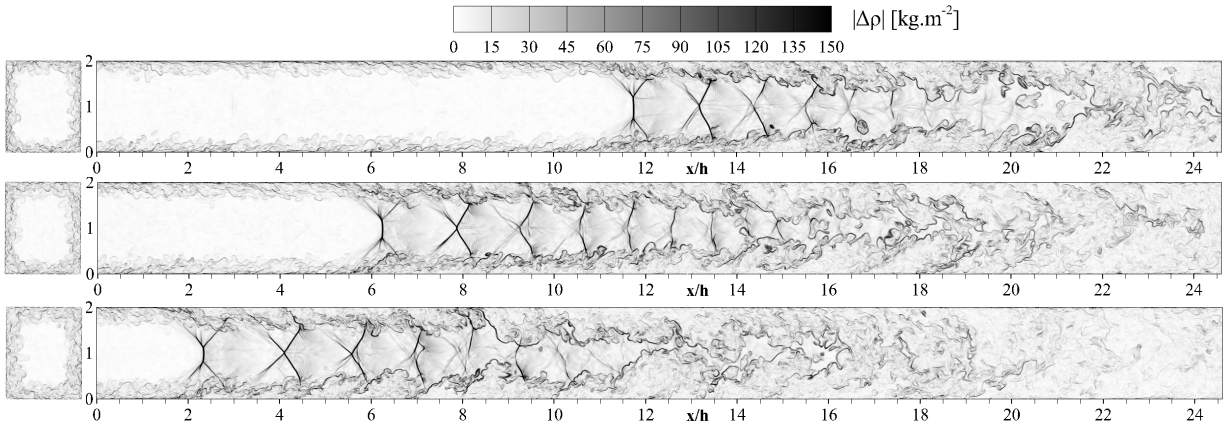

Figure 3.6: Instantaneous snapshots of density gradient magnitude for (top) case A, (middle) case B and (bottom) case C with the inlet plane on the left side.

2.1ms). Such unsteadiness is likely a consequence of the grid refinement and has been previously observed by Morgan *et al.* [91] who had to decrease the back pressure by 15% to keep the shock train idle on their finest grids. Alternatively, this could have a physical relevance as oscillatory behaviors are common in shock-boundary layer interactions [20, 141, 1, 106]. Regardless of the cause, the direction of shock train motion interestingly affects its structure appreciably. This change in structure is shown in Fig.3.7 where 16 frames are equally spaced in time and span a total time of 2 τ_c for case A. The contours of numerical Schlieren images highlight both the shape of the shocks and the turbulent boundary layer, giving insight into their coupling mechanics. Indeed, the magnitude of the boundary layer separation depends on the pressure gradient between the wall and the centerline, and is, therefore, a good indicator of the first shock strength. As can be seen from Fig.3.7, the shock train first moves downstream towards the outlet, and comes back upstream against the flow. When the shock train moves with the flow its relative speed decreases, which weakens the shocks. Whereas, with an upstream shock motion, the relative Mach number increases which strengthen the shocks. This causes the appearance of slip lines along the normal-like portion of the lambda shocks at the bifurcation points with the expansion waves [16]. A crude evaluation of the *apparent* Mach number evolution can be made assuming from

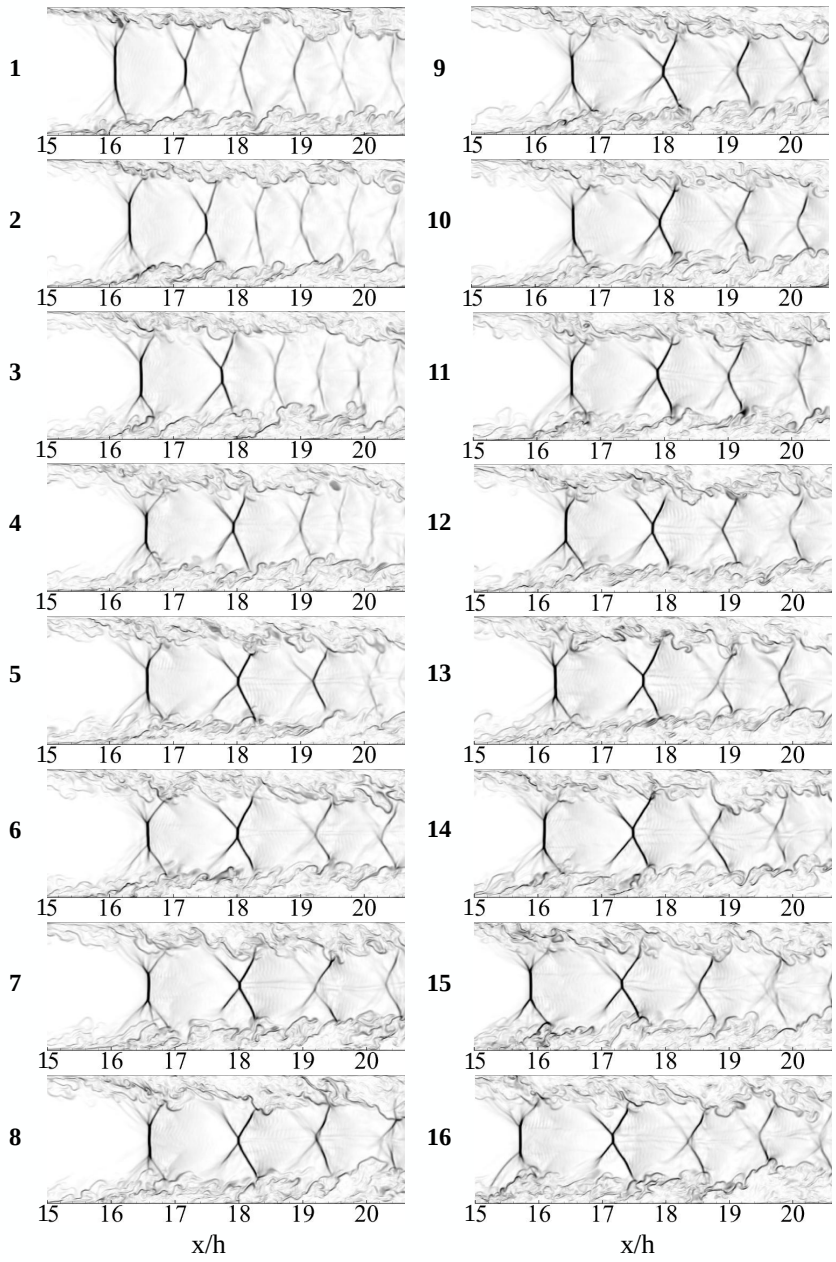

Figure 3.7: Snapshots of density gradient of the shock train foot for case A on grid R2 at 16 different times equally spaced over a duration of 2 τ_c.

Fig.3.7 a sinusoidal oscillation of amplitude of 1 channel height and of period $T = 2\ \tau_c$. This leads to a relative convective speed of maximum amplitude $2\pi h/T$, resulting in a range of *apparent* Mach number $Ma_{app} \in [1.83; 2.17]$, oscillating around the bulk Mach number $Ma = 2$. This broad range of *apparent* Mach number changes the nature of the shock train

from a normal shock train to an oblique shock train type (smaller normal part in the leading shock, thicker boundary layer and larger distance between shocks) [85]. In Fig.3.7, frames 1-4 correspond to a weak structure, 5-8 to a steady strand, and 9-16 to a strong shock structure. A comparison between frames 1 and 16 validates the previous statements as both the distance between shocks and the turbulent boundary layer thickness increase, which is characteristic of a higher Mach number shock train. Due to the large timescales involved with this phenomenon, statistics might differ based on whether the samples were taken in the oblique/weak or normal/strong shock train instances. A similar change in shock structure has been observed experimentally [13], albeit with smaller oscillation amplitude in a lower Mach number flow. These observations are parts of the motivation to investigate the shock train response to forced oscillations in Sec. 3.4.

3.2.3 Time-averaged contours

Figures 3.8 and 3.9 show the time-averaged statistics of the Mach number and pressure fields, respectively, for the three different inflow confinement ratios. These statistics correspond to the last 0.5ms ($\tau_c/4$) of the DNS run. Case A's leading lambda-shock presents a larger normal-like portion than case C, resulting in a larger subsonic region behind it. This suggests that the first shock strength depends directly on the confinement ratio. It is found that a thinner boundary layer leads to a smaller boundary layer detachment below the leading shock. As a result, the shocks occupy more space in the channel and the pressure growth rate is steeper than for the large confinement ratio case.

This feature appears clearly when plotting wall and centerline pressure signals on the center plane in the spanwise direction. Figure 3.10 shows the centerline and wall pressure traces while the middle figure in Fig.3.11 shows the wall pressure growth along the pseudoshock region. The shock train length is then defined based on the location where 90% of the compression is reached and is denoted by x_{st}. Overall, the same compression ratio is achieved over a shorter length for a shorter inlet confinement ratio, with the wall pressure

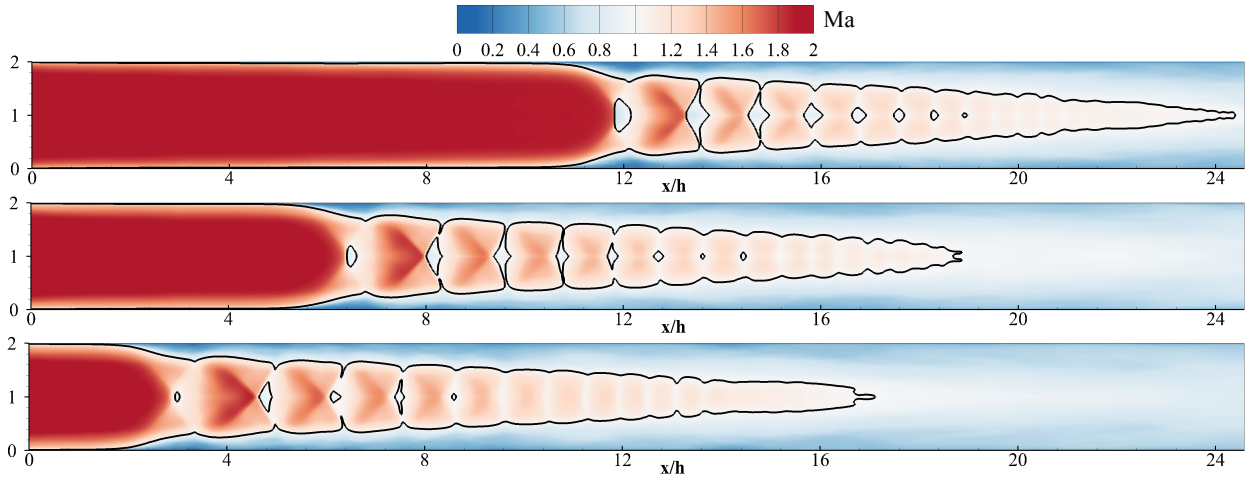

Figure 3.8: Time-averaged contours of Mach number with sonic line in black for (top) case A, (middle) case B and (bottom) case C.

showing a steeper rise for smaller inlet δ/h. To estimate the axial rate of compression, a quantity Σ is defined such that

$$\Sigma(x) = \int_{(yz)} \frac{P(x) - P_{in}}{P_{out} - P_{in}} dydz. \tag{3.1}$$

It is seen in the middle figure in Fig.3.11 that the first cell compression is stronger, and shorter. This difference is further increased for the following cells, therefore shortening the shock train. This metric shows a linear correlation with inflow momentum thickness based Reynolds number as seen on the right figure.

Based on both instantaneous and time-averaged results, the following dependence of the shock train structure on the inlet confinement ratio can be elucidated. In case A to case C, the confinement ratio increases. The leading shock is bifurcated with a normal-like portion and a lambda shock that interacts with the boundary layer. Since the bulk inflow Mach number is the same for all simulations, the angle of the oblique foot of the lambda shock remains similar. As the confinement ratio increases, the bifurcation point moves towards the center of the flow, leading to a smaller normal-like portion. Since normal shocks provide higher compression, this reduction in size leads to a weaker compression

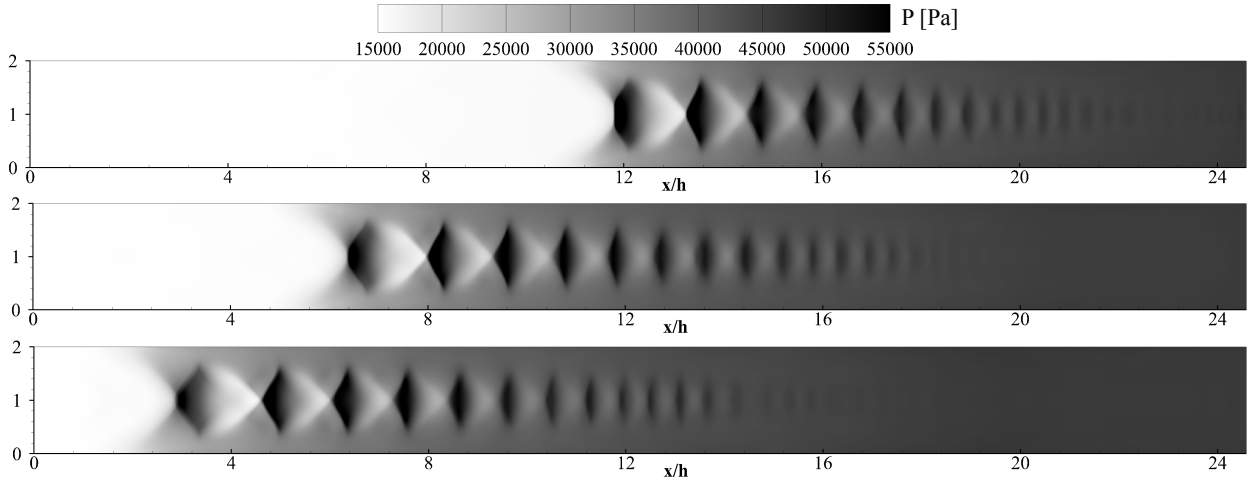

Figure 3.9: Time-averaged contours of static pressure for (top) case A, (middle) case B and (bottom) case C.

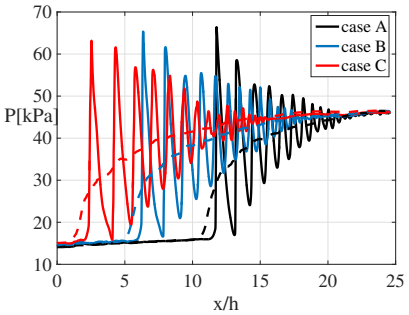

Figure 3.10: Centerline (solid) and wall (dashed) static pressure profiles for all cases.

across individual shock structures in the shock train. At the same time, as the bifurcation point moves towards the center of the channel, the back foot (downstream part) attaches to the boundary layer further downstream, delaying the appearance of the expansion wave and the subsequent shock structures. Consequently, increasing the confinement ratio increases the diamond-patterned cell size but decreases compression and flow deceleration. Past the first shock, reattachment causes the boundary layer to regenerate, and the influence of the shock-generated detachment decreases. The generation of the next shock structure is again based on the local confinement ratio. As a result, the distance between the shocks depends mainly on the core Mach number. The discrepancies between the cases thus build up after each compression/expansion cycle.

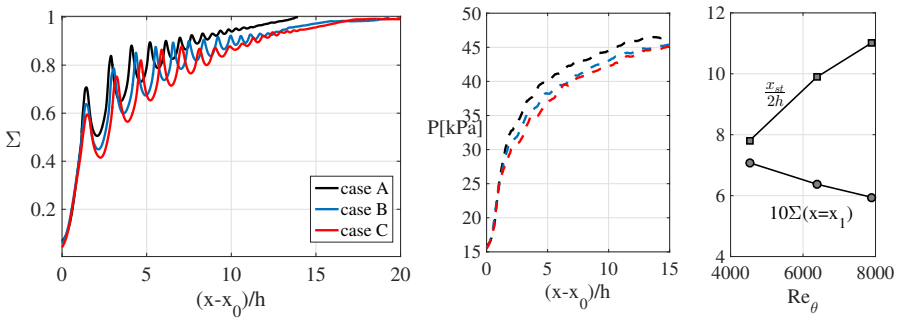

Figure 3.11: (Left) Integral of the normalized static pressure gradient Σ over the isolator rectangular cross-section. (Middle) Wall pressure rise profiles along the pseudoshock. (Right) Evolution of shock train length (■) and leading compression strength $10 \times \Sigma(x_1)$ (●) as a function of inflow Re_θ.

In summary, the inlet boundary layer thickness determines the normal-like portion of the leading shock. This directly impacts compression efficiency as well as the size and spacing of the diamond cells. Ultimately, the length of the shock train is determined based on the applied back pressure and the boundary layer thickness. This means that the increased length is directly tied to a slower conversion process of kinetic into internal energy. This process is investigated in the next section.

3.3 Energy conversion process

The pseudoshock is a system converting the inflow kinetic energy into internal energy. While computationally cheaper than time-resolved simulations, RANS simulations compute the increase in internal enthalpy by evaluating an approximated and closed form of the time-averaged Navier-Stokes equations. Notably, it typically neglects the turbulent pressure strain rate source terms. The current DNS simulations are exempted from any alteration of the Navier-Stokes equation and can offer some insight into the energy conversion process throughout various zones across the pseudoshock. Such decomposition, term by term, is the focus of this section. In the remainder of the analysis, an overline represents a Reynolds-averaged quantity while a tilde corresponds to a Favre-averaged quantity defined as $\tilde{X} = \frac{\overline{\rho X}}{\overline{\rho}}$. The Favre-averaged definition permits to account for the gas compressibility when deriving

the time-averaged Navier-Stokes equations [97]. Compressible RANS solvers are therefore sometimes referred to as FANS, although the widely-used RANS terminology is kept for the sake of simplicity throughout the dissertation to refer to both compressible or incompressible time-averaged simulations.

The Favre-averaged total enthalpy $\tilde{H}$ can be decomposed into internal enthalpy $\tilde{h}$, mean kinetic energy K and turbulent kinetic energy k:

$$\tilde{H} = \tilde{h} + \frac{\tilde{u_k}\tilde{u_k}}{2} + \frac{\widetilde{u_k'' u_k''}}{2} = \tilde{h} + K + k. \tag{3.2}$$

Each of these components has its own transport equation :

$$\frac{\partial \overline{\rho}\tilde{u_i}\tilde{h}}{\partial x_i} = \tilde{u_i}\overline{\frac{\partial p}{\partial x_i}} + \overline{u_i''\frac{\partial p}{\partial x_i}} + \overline{\tau_{ij}\frac{\partial \tilde{u_j}}{\partial x_i}} + \overline{\tau_{ij}\frac{\partial u_j''}{\partial x_i}} + \overline{\rho}\tilde{\dot{q}} + \overline{\frac{\partial \lambda_i}{\partial x_i}}, \tag{3.3}$$

$$\frac{\partial \overline{\rho}\tilde{u_i}k}{\partial x_i} = -\overline{\rho u_i'' u_i''}\frac{\partial \tilde{u_i}}{\partial x_j} - \overline{\tau_{ij}\frac{\partial u_j''}{\partial x_i}} + \frac{\partial}{\partial x_j}\left(-\frac{1}{2}\overline{\rho u_i'' u_i'' u_j''} + \overline{\tau_{ij}u_i''}\right) - \overline{u_i''\frac{\partial p}{\partial x_i}}, \tag{3.4}$$

and

$$\frac{\partial \overline{\rho}\tilde{u_i}K}{\partial x_i} = \overline{\rho u_i'' u_i''}\frac{\partial \tilde{u_i}}{\partial x_j} - \overline{\tau_{ij}\frac{\partial \tilde{u_j}}{\partial x_i}} + \frac{\partial}{\partial x_j}\left(-\frac{1}{2}\overline{\rho \tilde{u_i} u_i'' u_j''} + \overline{\tau_{ij}\tilde{u_i}}\right) - \tilde{u_i}\overline{\frac{\partial p}{\partial x_i}}. \tag{3.5}$$

The source terms colored on the right-hand side corresponds to energy exchange processes between the internal enthalpy and the mean/turbulent kinetic energy. Mean pressure work is colored in red and the turbulent pressure work is colored in cyan. The last term is often called turbulent pressure-strain correlation and is usually neglected in RANS. It usually appears in its decomposed form $\overline{u_i''\frac{\partial p}{\partial x_i}} = u_i''\frac{\partial \overline{p}}{\partial x_i} - \overline{\frac{\partial u_i'' p}{\partial x_i}} + \overline{p'\frac{\partial u_i''}{\partial x_i}}$. The viscous dissipation of mean kinetic energy is colored in purple, negative production of turbulent kinetic energy is colored in blue, and viscous dissipation of turbulent kinetic energy is colored in green. The energy conversion process is illustrated in Fig. 3.12. Note that the inflow kinetic energy can, therefore, flow into the internal enthalpy through different paths. Notably, the mean kinetic

energy can first be converted into turbulent kinetic energy which could either dissipate or interact with a fluctuating pressure gradient to be converted into internal enthalpy. This will be referred to as the indirect path, as opposed to direct conversion of mean kinetic energy into internal enthalpy.

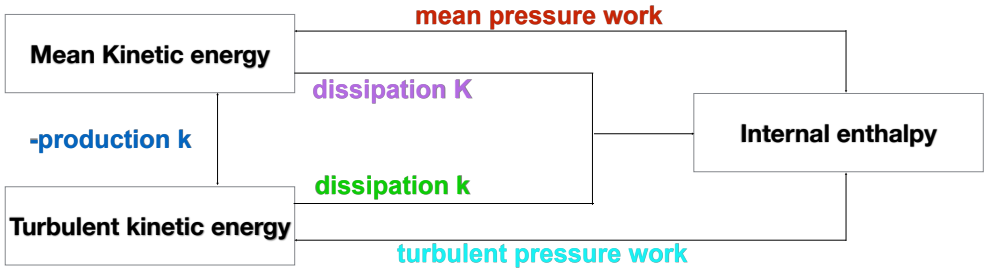

Figure 3.12: Energy conversion process from kinetic into internal energy.

In order to investigate the energy pathways throughout the pseudoshock, a set of streamlines is extracted from the 3D time-averaged dataset for case B. Projections of these streamlines on the Z-centerplane are presented in Fig. 3.13. They cover various location along the boundary layer by being initiated at various wall normal distance: y = 1, 0.75, 0.5, 0.25 and 0.1 half-channel heights and at x=z=0 m. This results in various residence times along these streamlines presented in Fig. 3.14. The residence time is computed from the local velocity vector and is used to evaluate the various source terms from the energy conversion rates of interest. It is, therefore, possible to integrate these source terms and reconstruct the internal enthalpy rise: such normalized reconstruction is presented in Fig. 3.15. The profiles match the local internal enthalpy with small departures due to the neglect of the diffusion term which gains in importance as the streamlines are closer to the walls. It shows that the bulk process is correctly evaluated. A comparison between each energy source terms is then presented in Fig. 3.16. It reveals that mean dissipation accounts for less than a percent of the process regardless of the streamline distance to the wall. This is not a surprising result since the overall mean dissipation process is expected to occur at the walls. However turbulent dissipation does account for a non-negligible amount of internal enthalpy rise, particularly across the boundary layers. Also, turbulent pressure work is even dominant around

the shocks: this could be caused by the interaction of centerline turbulence with the shocks, or more indirectly by the shocks inherent instabilities. As the shocks oscillate around their mean equilibrium locations at low-frequency [20, 52] large departures from the time-averaged solution can be observed and artificially increase this term. The simulation was then rerun sampling statistics in the leading shock frame of reference. It resulted in a maximum turbulent pressure work share of only 12% along all streamlines crossing the leading shock (greatly reduced from the 70% when sampling in the laboratory frame of reference), while it increased its share along the boundary layer streamlines (green and purple in Fig. 3.16 (top)) up to 20% by artificially moving the reference frame. Hence, it is difficult to precisely determine the amount of turbulent pressure work artificially caused by the sampling process, but it appears to be non-negligible even when choosing the optimal reference frame. Therefore, it can be concluded that neglecting turbulence pressure work in most RANS affects the overall energy conversion process. A RANS simulation of case B using the VULCAN NASA solver was performed by Dr. Robert Baurle with a Menter-SST model. The RANS inflow conditions match the DNS within 1% error for the bulk properties, and within 5% of the Reynolds stresses wall normal profiles in the Z-centerplane[2]. The energy conversion process along the same streamlines is shown in Fig. 3.16 (bottom). Mean pressure work is dominant in the supersonic core flow and seem to have accounted for the disappearance of turbulent pressure work. Dissipation of turbulent kinetic energy plays also a greater role in the conversion process through the indirect path than in the DNS.

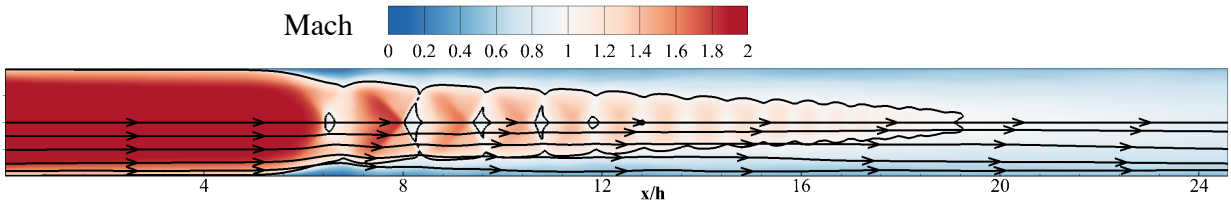

Figure 3.13: Set of streamlines spawning the shock train (case B).

[2]Correspondence with Dr.Baurle

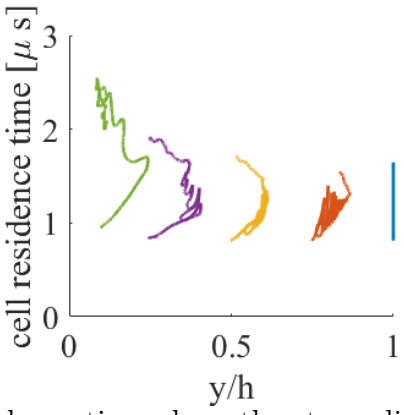

Figure 3.14: Local residence time along the streamlines presented in Fig. 3.13.

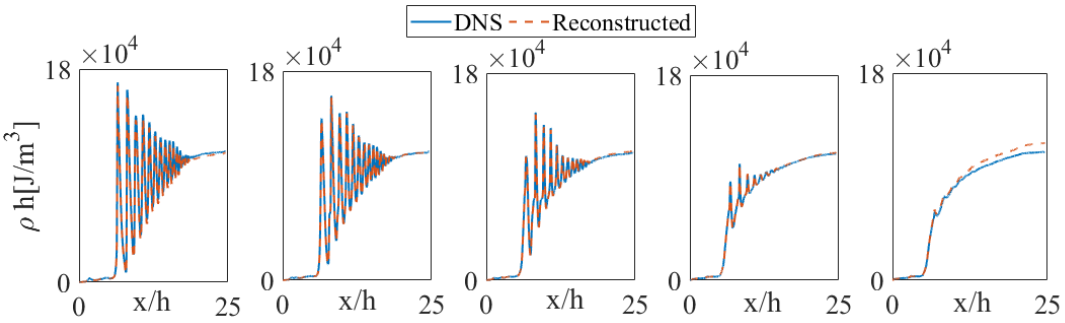

Figure 3.15: Internal enthalpy and reconstructed profile from integrated source terms along the streamlines presented in Fig. 3.13.

Lastly, another RANS simulation of case A was performed. A comparison between cases RANS-A and RANS-B is shown in Fig. 3.17. The lack of centerline normal-like portion increases the shock train length: the RANS simulations over-estimate it compared to the DNS. Also, the shifted centerline pressure profiles are almost identical as seen in Fig. 3.18 which is not realistic and highlights the limit of RANS simulation in studying pseudoshocks physics.

In summary, this analysis permits to identify turbulent pressure work as a non-negligible quantity for shock train numerical simulations. Also, while turbulent kinetic energy accounts for less than 1% of the inflow and outflow total energy in any of the shock train simulations performed, its dissipation accounts for an important amount of internal energy rise throughout the growing boundary layer and post-shock train mixing region. Turbulent kinetic energy is first produced by the initial boundary layer detachment below the leading shock, and only

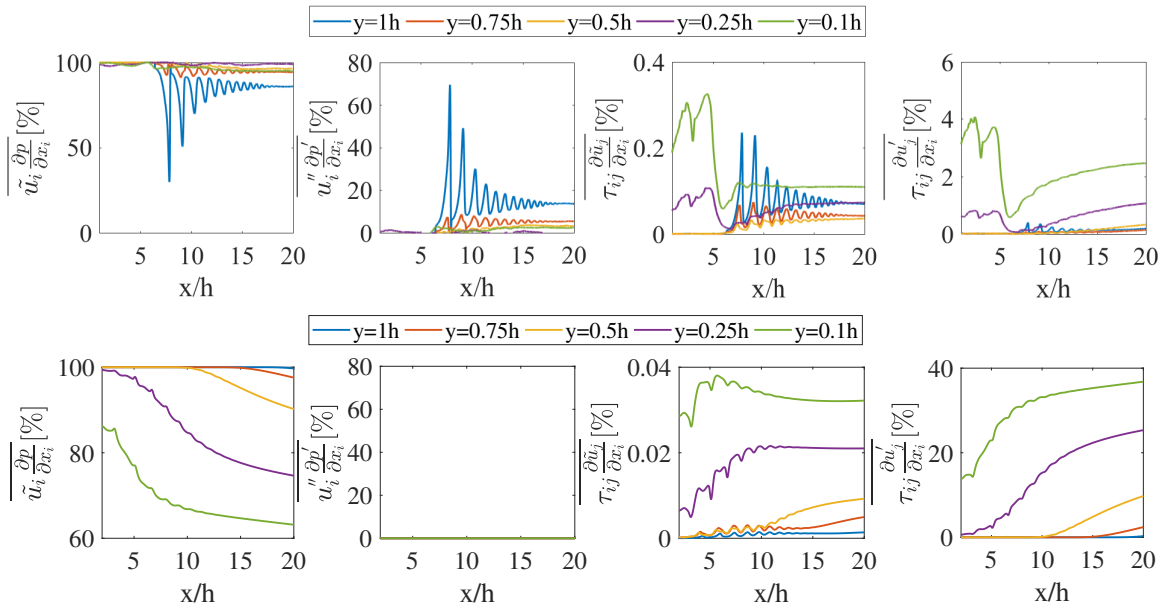

Figure 3.16: Fractions of different source terms along the streamlines presented in Fig. 3.13 for (top) DNS and (bottom) Menter-SST RANS simulation using the VULCAN NASA solver.

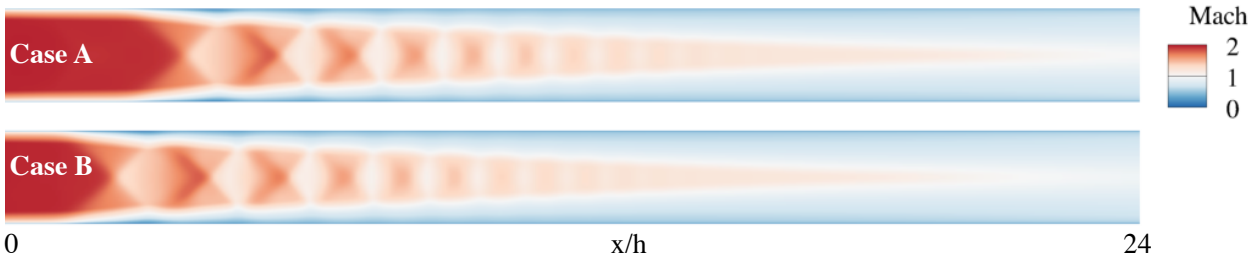

Figure 3.17: RANS simulations of cases A and B using Menter-SST model in VULCAN solver.

later dissipated. This energy conversion path is called "indirect" as opposed to the "direct" conversion of mean kinetic energy into internal energy. Thicker boundary layer cases would rely more on this indirect and slower conversion process, which partly explains why large confinement ratio pseudoshock are longer.

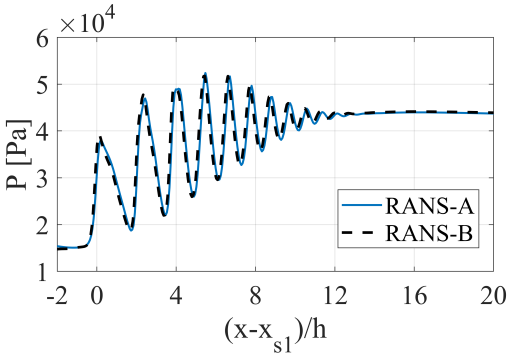

Figure 3.18: Centerline pressure profiles of RANS simulations for cases A and B.

3.4 Effect of inflow boundary layer thickness fluctuations on shock trains

In practical DMSJ designs, the downstream combustor section will respond to shock train movements, typically through a thermal throat located downstream in the combustor. Another way to introduce these motions is through upstream boundary layer variations, which is considered in this study. As discussed in Sec. 1.2, boundary layer changes are also useful for active control of the unstart process. Hence, a critical design aspect is the dynamic response of the shock train to back-pressure rise ratio or inflow confinement ratio fluctuations. While experiments can cover much lower frequencies (<10 Hz [63, 51]), only higher frequencies (>10Hz) are tractable in high fidelity simulations. In order to capture the main response characteristics, numerical simulations have to span a computational time of the order of 100 τ_c, which is out of reach for DNS-like resolutions.

In this section, we propose to investigate the dynamic response of the shock train structure to inlet boundary layer height harmonic perturbations. In order to access the lower range of the accessible frequencies, the simulations are further accelerated by first adopting the coarser grids R1 and later R2 defined in Sec. 3.1.2. The section will be divided into three parts. First, a broad spectral range of inflow harmonic oscillations will be investigated on grid R1 over large physical timescales on the order of 100 τ_c. Second, since grid R1 was shown in in Sec. 3.1.2 to be under-resolving the shock train structure, one additional simulation

will be performed on grid R2 at any particular frequency of interest revealed by the first scan. Lastly, the shock train response to inflow oscillations will be described in light of the results obtained from all simulations.

3.4.1 Broad spectral investigation

As previously mentioned, the unsteadiness observed in Sec. 3.2 is not present on grid R1. This creates a steady shock train for case B inflow conditions (seen in the centerline pressure space-time contour shown in Fig.3.19) which serves as a baseline case. As no oscillations are found in the shock train length and position, any unsteadiness observed would be the exclusive shock train response to the inflow oscillations. The wall pressure profiles were found to compare relatively well with the DNS (Fig.3.3) and will be used in the analysis below to investigate the temporal response of the coarse shock train.

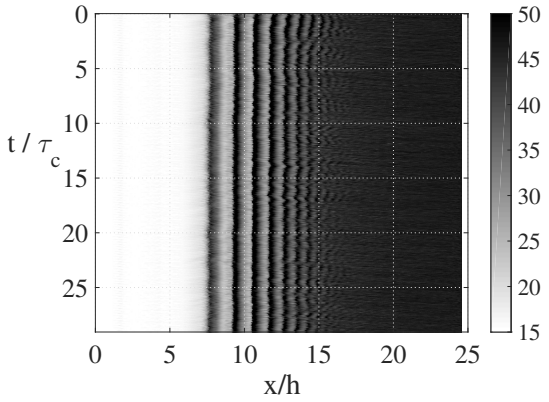

Figure 3.19: Space-time plot of the centerline pressure (kPa) for case B when using the coarse grid R1.

The inflow perturbation is introduced by temporally interpolating between the inflow fields for case A and C. Figure 3.20 shows the theoretical variation in momentum θ and boundary layer δ thicknesses over one period. Six different cases, corresponding to cycling frequencies $f_i \in [20; 60; 100; 200; 500; 1000\text{Hz}]$ were simulated. Each simulation ran on 4000 cores for 120 hours, and data was sampled at a 10 kHz rate. In each case, the wall pressure profile is used to estimate the shock train length. For instance, Fig.3.21 shows on the left

the instantaneous bottom wall pressure trace as well as a filtered trace. The foot of the shock is estimated based on the earliest location where the filtered pressure rises to 10% of the difference between the inflow and back pressure. The mid-point of the shock train is determined as 50% of that pressure difference value, while its tail is located at 80% of the pressure difference. For the discussion below, the shock train length is defined as the distance between the 10% and 80% pressure rise locations. Its unperturbed length is $7.66h$.

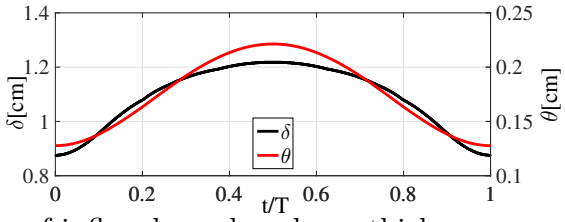

Figure 3.20: Variation of inflow boundary layer thickness over one oscillation period.

First, the temporal evolution of the 10, 50 and 80% back pressure rise locations is analyzed. Figure 3.21 presents these signals for the 20, 100 and 500Hz cases only (for the sake of brevity). The 20Hz case exhibits similar amplitude oscillations for all 10, 50 and 80% signals, although the shock train foot and tail are slightly out of phase due to the time taken for the perturbation to propagate downstream. At 500 Hz frequency, the shock train is essentially unchanged, indicating that this is too high a frequency to be accommodated by the system. However, the 100Hz intermediary case presents some interesting nonlinearity as it is not merely a blend of the low-frequency and high-frequency solutions. The shock train foot amplitude oscillation does decrease compared to the 20Hz case, but the tail response stays as strong and is out of phase. To further understand the frequency response, it is useful to define a normalized shock train length defined as the distance between the wall 10 and 80% pressure growth locations. These time-varying locations are called x_{10} and x_{80}.

$$\chi_{st}(t) = \frac{(x_{80} - x_{10})(t)}{(x_{80} - x_{10})(t = 0)}. \tag{3.6}$$

In the discussion below, $\xi_{st,i}$ refers to the single-side amplitude spectra of χ_{st} when excited with frequency f_i.

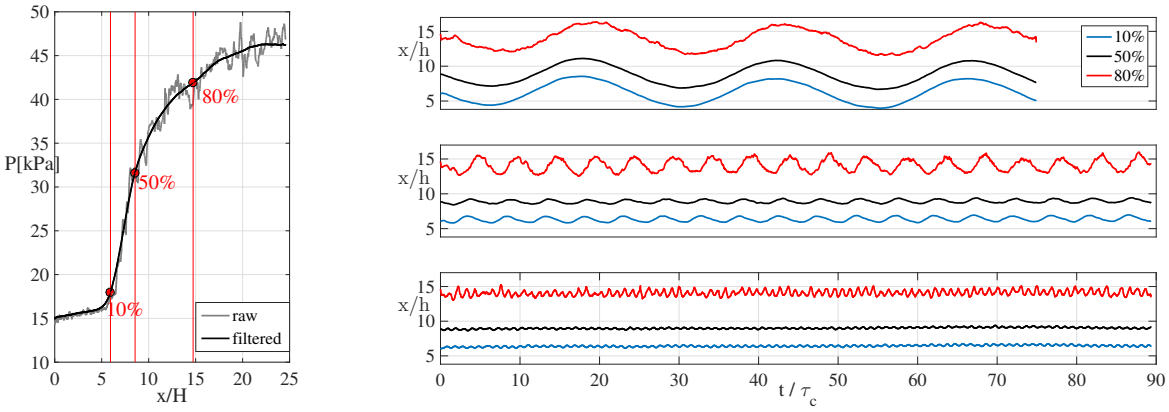

Figure 3.21: (Left) Original and filtered signal used to identify the location of the 10, 50, and 80% pressure locations. (Right) Temporal variation of the 10, 50 and 80% pressure rise locations for (top) 20Hz, (middle) 100Hz and (bottom) 500Hz.

Figure 3.22 shows $\chi_{st}(t)$ plotted as a function of normalized time for the different frequency perturbations. The single-sided amplitude spectra $\xi_{st,i}$ of these signals are shown at the bottom left. Not surprisingly, the most energetic spectral content matches the frequency of excitation in all cases. The peak spectral content for each frequency is shown alongside. $\xi_{st,i}(f = f_i)$ is plotted as a percentage of the undisturbed shock train length to show the shock train length sensitivity to a particular excitation frequency. It is seen that the 60-100 Hz perturbation range leads to a resonance-like behavior as it causes the largest increase (about 15%) in shock train length over the unperturbed shock structure. This highlights the spring-like behavior of the shock train in response to upstream instabilities, with a resonance frequency $f_c \in$ [60Hz; 100Hz].

We observe that the resonance is caused when the shock train compression/expansion cells adjust to the boundary layer as fast as possible. In the phase where the boundary layer shrinks, the leading shock moves downstream, pushing the other cell structures further downstream, thereby reducing the size of the compression/expansion cell sizes (this corresponds to case A). The opposite is true when the boundary layer grows (corresponding to case C). The cell size adjustment to the inlet boundary layer starts at the foot of the shock train (leading shock) and propagates to the tail (trailing shock), with an observable delay

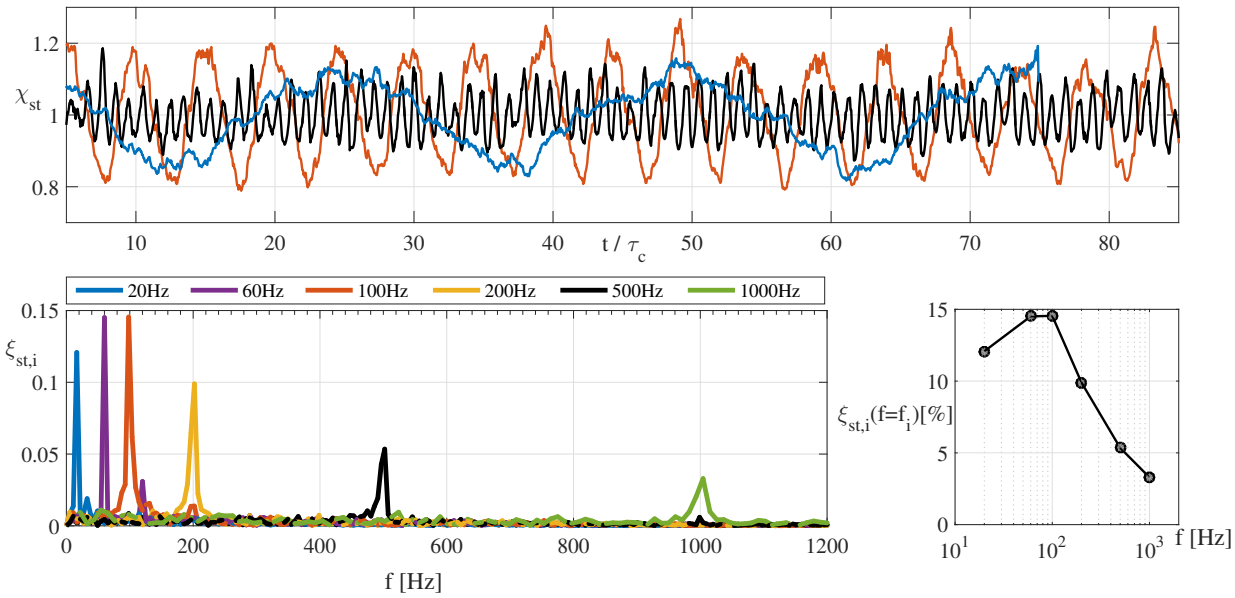

Figure 3.22: (Top) Shock train length as a function of time for 20, 100 and 500Hz excitations. (Bottom left) Single-sided amplitude spectra for the shock train length for all frequencies. (Bottom right) Amplification of the shock train length for all excitation frequencies expressed as percent of unperturbed length.

as the shocks interact with their neighbors. This causes a phase lag that is augmented by each compression/expansion cycle. This is the same mechanics illustrated in Fig.3.7: moving from the earliest time snapshot, it can be seen that the first shock pushes the next shock and so on until the entire shock train has adjusted to the change in inflow condition.

The resonance frequency can be determined with greater accuracy by measuring the phase lag between the time-varying wall pressure locations x_{10} and x_{80}. The fluctuating components of these two quantities are x'_{10} and x'_{80}, respectively, and defined as the fluctuation about the arithmetic average of $\overline{x_{10}}$ and $\overline{x_{80}}$ from x_{10} and x_{80}. Figure 3.23 shows the time variation of these two fluctuating quantities. In addition, the cross-correlation between the two signals is also shown. This quantity corresponds to the convolution product $x'_{10} \star x'_{80}\,(\tau)$ where τ is the time-separation of the signals. The red line gives the location of maximum correlation, while the dashed black line locates the origin. Note that the maximum correlation location does not coincide with zero time-difference, indicating that there is a time lag between the

oscillations at the two locations. This time-lag is indicated in the top right corner of all $x'_{10} \star x'_{80}$ plots. Using the corresponding excitation frequency, the time lag is converted to a phase lag. The measured phase lag between the x'_{10} and x'_{80} signals for the 20, 60, 100 and 200Hz oscillation cases were 23.7, 64.8, 100.8 and 129.6°, respectively. Resonance happens for a phase lag of 90°, and the resonance frequency f_c is estimated at 93Hz using linear interpolation for this shock train. This is within the peak range of spectral-response based on the experiment as mentioned at the end of Sec. 3.1.2. Figure 3.23 also reveals the strength of the resonance. For comparison, Fig.3.22 shows a 12% increase of shock train length at 20Hz, and a modest 15% increase of shock train length at 100Hz, which is close to the resonance frequency. From Fig.3.23, the oscillation amplitude for x'_{10} is much smaller at 100 Hz($\approx 0.37h$) than at 20 Hz ($\approx 2.01h$). Hence, the 15% increase in shock train length corresponds to a much higher amplitude ratio between the tail and foot at 100Hz (2.64) than at 20Hz (1.01). Had the x'_{10} amplitude oscillation remained constant for all excitation frequencies, the oscillation of the shock train length at 100Hz could have been as high as $2.01 \div 0.37 \times 15\% = 81\%$ of the unperturbed length. Such resonance could potentially disrupt the shock train compression ratio and even move it out of the isolator unstarting the engine. More interestingly, this analysis reveals that a low-pass filter precedes the spring-like behavior of the isolator, which reduces the oscillation amplitude of the shock train. This aspect is further investigated below.

The x'_{10} and x'_{10} signals spectral contents $\xi_{10,i}$ and $\xi_{80,i}$ are now separately analyzed using the same process as χ_{st}. Figure 3.24 is the equivalent of Fig.3.22 and quantifies the oscillation amplitudes normalized by the initial shock train length of both the foot and tail of the shock train as a function of the excitation frequency. While the oscillation at the lowest frequency is the largest (about 25% of the unperturbed shock train length), it is remarkably equal for both foot and tail. This suggests there is little interest investigating frequencies lower than 20 Hz as the shock train's dynamic response seems to fully accommodate such high wavelengths (response time much smaller than the excitation). The foot and tail oscillation

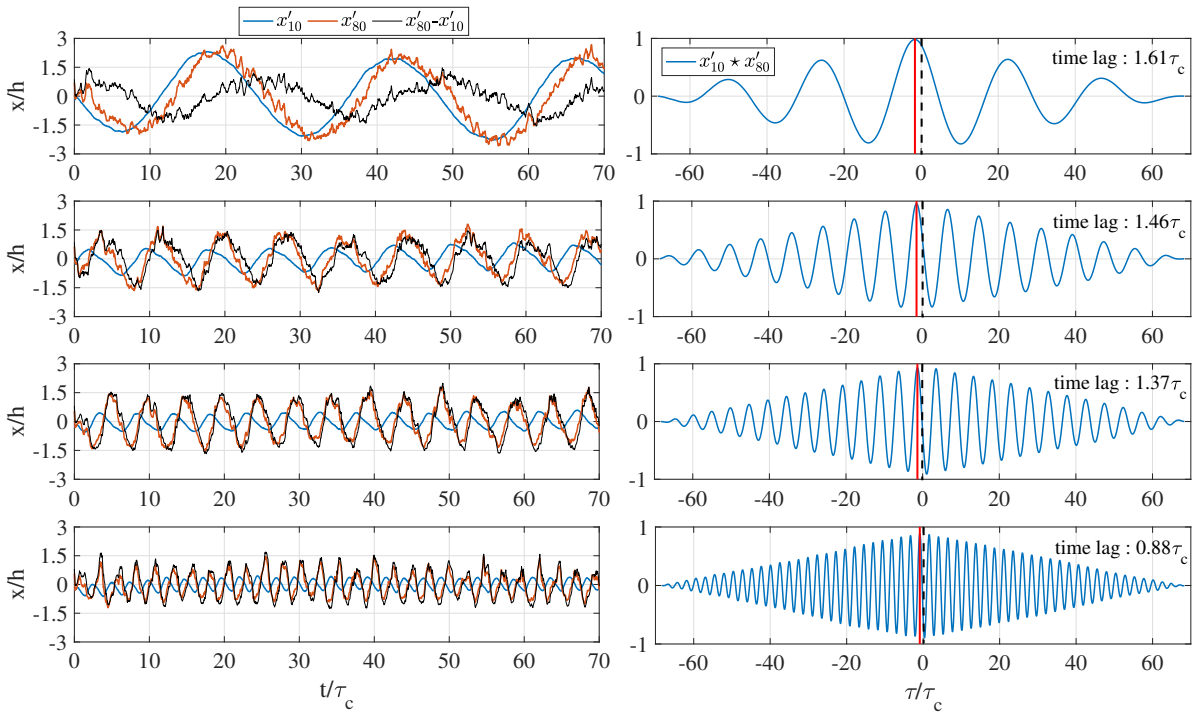

Figure 3.23: (Left) x'_{10}, x'_{80} and x'_{80}-x'_{10} as a function of time (from top to bottom) for 20, 60, 100 and 200Hz excitation. (Right) Cross-correlation between x'_{10} and x'_{80} for corresponding frequencies in the left plot. Red line indicates the peak location.

amplitude might increase, but remain equal and the shock train would just translate inside the isolator in between the solution of case A and C. As the frequency increases, the reduction in oscillations of the shock train is more pronounced at the foot than the tail of the shock train, which is also observable in Fig.3.23. The boundary layer detaches at the shock train foot, and the 10% pressure rise location resides in the recirculation bubble slightly upstream of the axial position of the first shock as seen in Fig.3.10. Since this separation bubble has a very low dynamical response due to the highly viscous and low-speed fluid contained within, the response of the shock-train also is damped with increasing perturbation frequency. Further, the static pressure in the recirculation bubble tends to be more uniform (that is, spatially homogenized) and would, therefore, be less sensitive to high-frequency changes to the flow field. On the contrary, the 80% pressure rise location is directly located under the trailing shocks in the shock train and is more directly correlated to their strength.

As noted earlier, the grid coarsening introduces artificial numerical dissipation, which

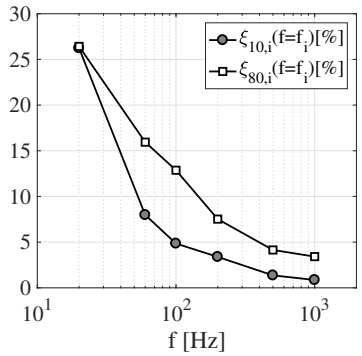

Figure 3.24: Amplitude variation of x_{10} and x_{80} for all excitation frequencies f_i expressed as percent of the unperturbed shock train length..

dissipates the highest frequency structures in the flow. Increased resolution will alter shock train response by changing the dynamics of the recirculation bubble at the shock foot. Further, it was also observed that R1 grid based shock train structure differs from the R2 and R3 profiles, especially weakening the centerline compression and expansion waves. As resonance seems to be partly triggered by the phase lag between the leading and tailing shocks, its characteristic frequency would logically be affected by an increase in strength and number of shocks. Hence, it is entirely plausible that a resonance will be observed on finer grids as well, albeit with different transfer functions than in Fig. 3.22. Finally, the large amplitude ratio between the tail and foot oscillation (Fig. 3.23) is the second cause for the increase in shock train length. Its causes are not elucidated yet, and it remains to be seen whether it would happen on higher resolution grids.

3.4.2 Grid-resolved oscillation analysis

In order to address these concerns, a last simulation is run on grid R2 at the resonance frequency of 93 Hz estimated from R1 calculations. As the R2 simulations presented in Sec. 3.1.2 are slowly convecting upstream, the back pressure is reduced from 70 to 65% normal shock rise to stabilize the shock train and avoid a contamination of the forced inflow oscillation with large-scale motions. This simulation has run on 8000 cores for 360 wall-clock hours. This represents a physical runtime of 68.4 ms or 33.4 τ_c, corresponding to 6.4

oscillation periods. The shock train accommodates the lower back pressure and becomes stable during the first 10 τ_c. The analysis below is based on data collected after this initial period. Additionally, the sampling rate is increased from 10 to 476 kHz to permit time-resolved analysis on the high-speed centerline flow.

The R2 grid simulation is first used to analyze wall pressure similarly to the R1 grid results shown in Fig. 3.25. The time lag between the x'_{10} and x'_{80} signals is measured at 0.31 τ_c giving an equivalent phase lag of 21°. This is less than the measured value on the coarse grid: a higher oscillation frequency would be necessary to trigger a 90° phase lag. As the resolution of grid R2 is twice higher than grid R1, the cut-off frequency is also doubled. Since the phase lag decreases by a factor ≈ 4, we can deduce that the smallest length scales (located in the boundary layer) play a paramount role in shock train dynamic. Consequently, the characteristic frequency is underestimated when low-wavelengths are filtered out. Yet, the amplitude of shock train length oscillations is similar to the R1 simulations given the change of back pressure and resolution. A $\xi_{st}(f = 93Hz)$ of 11.1% is computed, with a $\xi_{10}(f = 93Hz)$ and $\xi_{80}(f = 93Hz)$ of 7.4 and 17.6% respectively. These values are respectively of 14.5, 5.4 and 13.4% (using a linear interpolation at 93 Hz on Figs. 3.22 and 3.24) on grid R1.

As seen in Fig. 3.26, the change in shock train length over half a period (phase angle $\phi = [0,\pi/2,\pi]$) is very noticeable, particularly in terms of the number of shocks. Therefore, the refined grid simulation shows an increase of shock train length primarily due to the ratio between its tail and foot oscillation amplitudes, rather than a consequent phase lag (which is still present). This suggests that a model of the isolator response mechanism solely based on the phase-lag resonance phenomenon (analogous to a conventional harmonic oscillator) is not complete.

In an effort to identify the causes of the large oscillation amplitude of the shock train tail as compared to the foot, the time-resolved centerline pressure signal is scrutinized. Contrary to wall pressure profiles, the centerline profile is not filtered in space to retain the shock

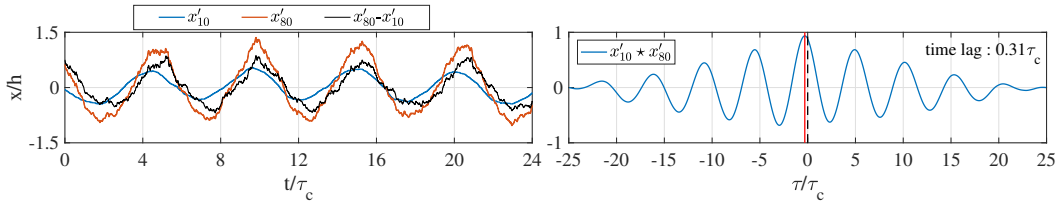

Figure 3.25: (Left) x'_{10}, x'_{80} and x'_{80}-x'_{10} as a function of time for 93 Hz excitation on grid R2. (Right) Cross-correlation between x'_{10} and x'_{80} for corresponding frequencies in the left plot. Red line indicates the peak location.

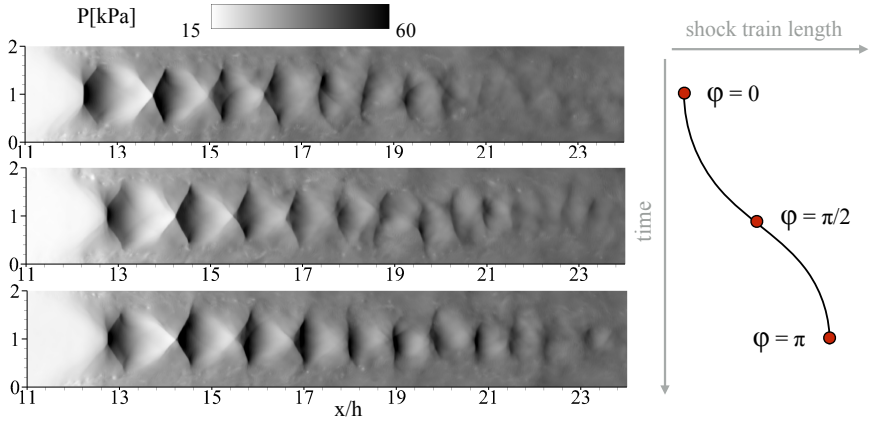

Figure 3.26: Snapshots of static pressure contours at various times over one half-oscillation period.

resolution but is filtered in time using a moving average filter (a simple unweighted mean) of bandwidth 0.1ms, *i.e.* less than 1% of an oscillation period. The space-time contour of the shock-train length is shown in Fig. 3.27. It is seen that the oscillation waveforms tend to distort from a clean sinusoidal form at downstream locations. Further, the shock train tail fades away when the structure is convecting downstream.

The time-varying locations and amplitudes of the constituent shocks are extracted. In Fig. 3.28, the phase angle ϕ based on the 93 Hz frequency oscillation is plotted as a function of two shock-related quantities: 1) the pressure $\tilde{P}_s$, defined as the peak pressure of shock number s normalized by the back pressure, and 2) the velocity $\tilde{u}_s$, which is defined as the local convective velocity of the s-th shock normalized by the inlet bulk speed. The vertical dashed line represents $\tilde{u}_s = 0$, while the horizontal line give the average of all $\tilde{P}_s$ realizations.

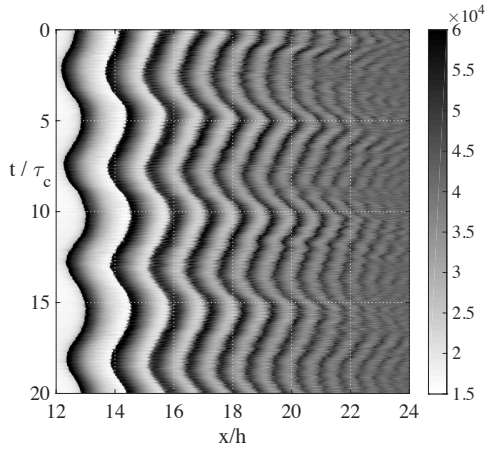

Figure 3.27: Space-time plot of the centerline pressure (kPa) for the 93 Hz oscillation case on grid R2

A 5% amplitude of $\tilde{u}_s$ (half the range of the plots) equals to a velocity variation of $\approx$ 26 m/s. Since the velocity decreases with downstream distance, this 5% amplitude corresponds to an increasing fraction of the local flow velocity. As a result, the amplitude of the s-th shock pressure oscillation increases as s increases: this shows up as an increased scattering in the $P_s - u_s$ plot. This increases the sensitivity of the tail to large-scale oscillations, which alternatively force the shock train into a weak or strong state, as identified in Fig. 3.7. The apparent Mach number range values defined in Sec. 3.2 3.2.2 increase with the convective velocity, such that the last shocks vanish ($Ma =< 1$) in the weak state. The tail of the shock train weakens and disappears at $\phi = 0$, then strengthens and reappears at $\phi = \pi$. This phenomenon is postulated to be the cause of the large ratio between x'_{10} and x'_{80} observed in all simulations for frequencies superior to 20 Hz.

3.4.3 Mechanics of shock train length fluctuations

From the discussion in the previous sections, it is possible to derive three different physical processes that affect shock train length when the inflow conditions are perturbed:

1. Shock-to-shock time-lagged interactions: Here, the upstream perturbation propagates through the cells with a certain time-lag depending on a local wave-speed. The wave-speed depends both on the perturbation frequency, as well the size of the compression-

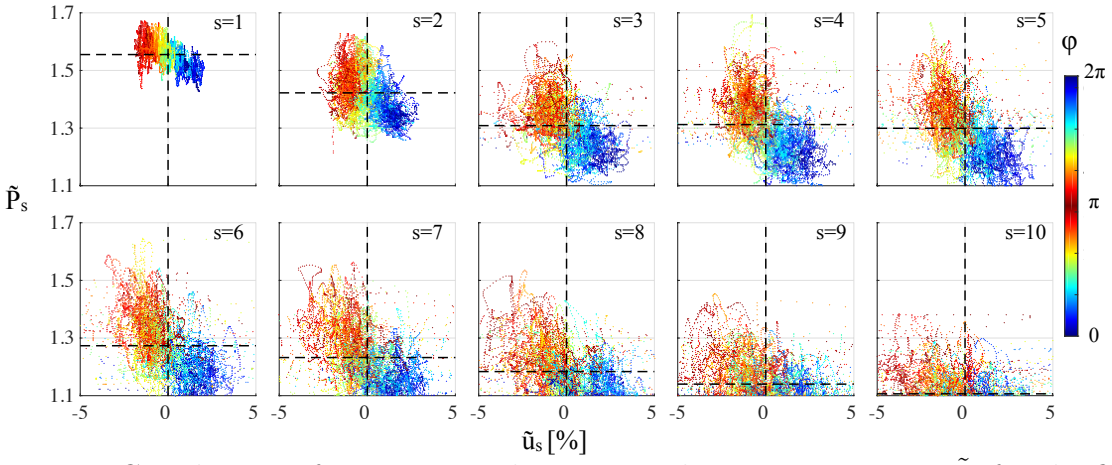

Figure 3.28: Correlations of convective velocity u_s with compression rate $\tilde{P}_s$ for the first 10 shocks of the shock train. The realizations are colored by their phase number.

expansion cells. As the large scales drive this mechanism, even coarse grids could capture this process. The resonance frequency is however very sensitive to the spatial resolution. When the phase lag is 90°, resonance behavior similar to harmonic oscillators is observed.

2. Apparent shock Mach number: In addition to the harmonic oscillator behavior, the length of the shock train also depends on its convective velocity relative to the flow velocity. To achieve a shock convective velocity on the order of the bulk streamwise velocity U and appreciably affect its apparent Mach number, the oscillation frequency f_s and amplitude A_s must be high enough such that $U \approx A_s f_s$. This effect introduced another characteristics frequency, which converts the isolator into an anharmonic oscillator. If the frequency f_s is high enough, the shock train tail will periodically disappear, which will change its length even if the shock-to-shock phase-lag is far from 90°. This is observed in the R2 grid simulations (Sec. 3.4.3.4.2).

3. Leading shock shape: As the inflow boundary layer thickness is varied, the shock train moves up or downstream. In addition, the leading shock undergoes changes in shape. When the leading shock is formed from a thin boundary layer, the normal portion

of the lambda-shaped shock structure grows, increasing the pressure jump across this shock and decreasing the overall shock train length. When a thicker boundary layer is encountered, the oblique part of the shock dominates, causing a growth in the length but a decrease in the pressure jump across the leading shock. From the data collected, it is not clear how fast the shock structures adapt to the changing boundary layer. Hence, the exact impact of this change in shock structure in a dynamic environment is not fully understood yet.

Another observation related to the mechanism is the importance of the transverse variations in the flow field. The momentum thickness variation amplitude is $0.027h$ (0.45mm) and is applied in the transverse (wall-normal) direction. Yet, the shock train motion can be roughly two orders of magnitude larger in the axial direction, while its length oscillates at a maximum amplitude of 40 mm. The resonance phenomenon is greatly attenuated by the upstream low-pass response of the shock train foot. Hence, even minor changes to the inflow boundary layer can have a significant impact on the shock train stability should the low-pass region be too small to filter these out. Also, the artificial increase of viscosity (x4) increases the wall shear stress and contributes to the damping of the recirculation bubble displacement. Finally, only sinusoidal excitations have been considered in this study. It may be the case that the shock train is relatively robust to broadband fluctuations in the inflow boundary layer.

3.5 Chapter conclusions

Direct numerical simulations of shock trains in a turbulent channel have been carried out. The database contains shock train data at different inflow conditions, characterized by variations in inflow boundary layer thickness. The other inflow parameters such as pressure, centerline Mach number and wall friction coefficient were kept constant. The simulations show that when the inflow confinement ratio reduces, the shock train is pushed towards

the exit. Additionally, the normal-like portion of the leading bifurcating shock increases with smaller inflow confinement ratio, leading to shorter but stronger compression cells. Hence, the spatial pressure growth rate of a pseudoshock decreases when the confinement ratio increases. A decomposition of the energy conversion shows that the indirect conversion path (mean kinetic energy converted into turbulent kinetic energy, then later dissipated into internal enthalpy) is important. Thicker boundary layer case rely more on this indirect and slower conversion process. This is consistent with the observation that the pressure growth rate of high confinement ratio pseudoshocks is smaller than that of lower confinement ratio.

When the inflow conditions are varied over time, the shock train response is non-trivial and depends on the excitation frequency. With too high or too low an excitation frequency, the shock train either stays nearly stationary or moves coincidentally to the inflow variation. At higher frequencies, two additional physical processes contribute to the appearance of a resonance phenomenon (an increase of shock train length). First, the perturbations travel downstream at a finite speed, and a phase lag between the train's foot and tail appears similar to a harmonic oscillator. Second, the shock's strength is correlated to their convective velocity relative to the flow stream. Shocks at the tail of the train, therefore, weaken and disappear while convecting downstream, or strengthen and reappear while convecting upstream, further increasing the shock train length oscillation amplitude. These two processes are triggered at different characteristic frequencies, defining the shock train as an anharmonic oscillator. Additionally, it is deduced that the low-pass filter nature of the leading shock prevents the shock train from exhibiting much larger spatial oscillations. Nevertheless, even small variations in the inflow boundary layer thickness are seen to cause large changes in shock train length.

CHAPTER IV

One-dimensional modeling of calorically perfect pseudoshocks

A one-dimensional model for pseudoshock is designed through data-driven optimization. It accurately predicts the pseudoshock length and pressure rise over a wide range of flow conditions relevant to dual-mode scramjet engines. The model is based on a flux-conserved approach coupled with a new pressure growth rate closure equation derived in light of recent findings in shock train physics presented in Chap.III. Both experimental and numerical datasets of both normal and oblique pseudoshocks are used to calibrate the model through a genetic algorithm. The model parameters are also determined to account for the pressure roll-off present in normal-type shock train, which permits the model to capture the transition from normal to oblique pseudoshock relevant to dual-mode scramjet engines. Bayesian inference is used to quantify the parameters cross-correlations and most probable values as a function of operating conditions. Finally, the model is transformed into an anharmonic oscillator which captures the dynamic response of the shock train to upstream perturbations presented in Chap.III. The overall result is an exhaustive transfer function between inflow spatial perturbations and the pseudoshock location/length/pressure time-signal. Most of this work is included in Fiévet *et al.* [37].

The chapter is organized as follows:

- Sec. 4.1 discusses the motivations behind the design of a reduced-order model for

pseudoshocks.

- Sec. 4.2 presents previous efforts in pseudoshock modeling and predictive tools.
- Sec. 4.3 details the derivation of an improved 1D model based on a flux-conserved approach and a new data-driven pressure growth rate.
- Sec. 4.4 uses Bayesian inference to calibrate the new model coefficients.
- Sec. 4.5 explains how the 1D model is modified to account for dynamic effects.

4.1 Motivation

It is well-established that the pseudoshock length and pressure rise ratio (PRR) strongly depends on the inflow Mach number and boundary layer properties [136, 135, 120, 85, 17, 18, 16]. However, differences in experimental facilities (such as duct aspect ratio) and methods of measurements (boundary layer statistics are typically measured at the center plane only) result in a scattering of results present across the literature [85] when trying to collapse on robust correlations. Popular models such as Waltrup & Billig correlation [136] and Ikui *et al.* diffusion model [54] are often used to predict the wall pressure growth and provide an estimation of both back pressure ratio and pseudoshock length. However, for the reasons mentioned earlier, their accuracy rapidly decays when out of the particular range of inflow conditions used to calibrate these models or define key assumptions. For instance, Waltrup & Billig used an extensive dataset of normal and oblique pseudoshocks in cylindrical ducts for Re_θ from approximately 5000 to 50000. Their correlation does not match recent experimental profiles obtained in either low aspect ratio rectangular ducts [63, 33] or at higher [96] or lower [42] Reynolds numbers than Waltrup & Billig experiments.

Conversely, time-resolved CFD calculations such as LES [21, 91, 59, 126, 114] or the DNS presented in Chap. III have demonstrated in the last few years the ability of numerical simulations to resolve pseudoshocks. Although such calculations offer insight on the physics

involved in pseudoshocks for canonical configurations, they are currently too expensive to be directly used for engine designing. Cheaper computational models exist and were previously discussed such as compressible RANS. However, they are notoriously dependent on their turbulence closure model as seen in Fig. 1.12. Moreover, even state-of-the-art RANS are unable to capture the effect of changing inflow confinement ratio as seen in Figure. 3.17. On the other hand, reduced-order models calibrated using experimental/numerical datasets could become precious design tools. Such inexpensive one-dimensional (1D) model should be able to correctly predict both the pseudoshock pressure rise ratio and length. Possibly, these tools could even be incorporated into RANS models to ensure a correct pressure growth rate.

Lastly, once an accurate 1D model is derived, it would be of critical interest to model dynamic effect describing inflow/outflow instabilities effect on the pseudoshocks length and back pressure recovery. As unstart is, in essence, an intermittent failure event such dynamic model would help predict its occurrence.

The scope of this chapter is to design a robust 1D model valid over a wide range of inflow conditions. The model should be able to correctly predict both the length of pressure rise (pseudoshock length), the recovered back pressure and the pressure roll-off. First, some existing pseudoshock models are presented, notably Smart's flux conserved 1D approach [116]. The pressure rise rate closure equation used in Smart's model is then modified in light of Fiévet *et al.* recent results on shock train sensitivity to inflow boundary layer thicknesses obtained through Direct Numerical Simulations. Then, a diverse set of pseudoshock dataset is used to optimize the new model's parameter. As most available datasets involve calorically perfect gas, the model derived in this paper will not take into account any real gas effect. A Bayesian approach is then used to gain an understanding of both the parameters cross-correlations and range of validity. Lastly, the static model is fed into a complex anharmonic oscillator model to account for the impact harmonic inflow perturbations have on the shock train structure. In particular, pseudoshocks sensitivity to inlet boundary layer profiles and confinement ratio was studied in the previous Chapter (Chap. III), and the DNS extensive

time-resolved dataset is used to calibrate the dynamic model.

4.2 Previous work

Some pseudoshock predictive tools and their limitations are presented in this section. First, popular empirical correlations between inflow characteristics and pseudoshock lengths are presented. Second, McLafferty's maximum pressure recovery model [88] based on conservation of flux-conserved properties is explained. Then, Smart's 1D model [116] is presented.

4.2.1 Empirical correlations

Walltrup and Billig [135] have derived from several experiment an empirical correlation for the wall pressure rise based on the incoming Mach number and boundary momentum thickness. This correlation is valid for pipe flow where a single momentum thickness value can be defined, and is presented in Eq. 4.1:

$$50\left(\frac{P}{P_0}-1\right)+170\left(\frac{p}{p_0}-1\right)^2=\frac{(x-x_f)(M_0^2-1)Re_\theta^{0.25}}{\sqrt{D\theta}} \tag{4.1}$$

where $(x-x_f)$ corresponds to the distance from the pseudoshock foot and P_0, M_0 and θ are the wall pressure, centerline Mach number and boundary layer momentum thickness upstream of the shock train respectively. D is the pipe diameter. This correlation tends to present a flattened pressure growth rate preventing the correlation to capture the low-Mach number pseudoshock roll-off. Also, it does not converge in space towards a particular pressure value, which means that it cannot estimate both the final pressure recovered at the end of the pseudoshock and its length. Billig [10] suggested a modification of the correlation for rectangular duct flows shown in Eq. 4.2 where D_h is the hydraulic channel height defined as $D_h=\frac{L_1L_2}{L_1+L_2}$ for a $L_1\times L_2$ rectangular cross-section.

$$50\left(\frac{P}{P_0}-1\right)+170\left(\frac{P}{P_0}-1\right)^2=\frac{(x-x_f)(M_0^2-1)Re_\theta^{0.2}}{\sqrt{D_h\theta}} \tag{4.2}$$

Sullins and McLafferty [120] compared their rectangular duct experimental dataset with this modified correlation and found that it captures the pressure growth rate accurately throughout the shock train (up to 80% pressure rise), but still fails to account for the roll-off in the mixing region. Geerts and Yu [46] replaced θ by the quadratic average of all walls mean momentum thicknesses in Eq. 4.1 in an effort to account for corner flow effects. It led to an improvement of the correlation accuracy in estimating the pseudoshock length when knowing the target back pressure for their oblique pseudoshocks experiments (Mach numbers of 2.5, 3.0 and 6.0).

In general, experimental datasets of various Mach number do not tend to collapse on these correlations [120, 121, 63, 41] and cannot predict the maximum pressure recovered at the end of the pseudoshock. Instead of relying on empirical correlations, models based on conservation principles accounting for viscous loss have been elaborated.

4.2.2 Maximum pressure recovery

The maximum pressure recoverable from a shock train given its inflow bulk Mach number and boundary layer description was computed by McLafferty [88]. His approach consists in computing the equivalent flux-conserved properties at the shock train foot (Fig. 4.1), and use 1D conservation laws to find the unique subsonic solution verifying the conservation of mass flow rate and stream thrust. In the remaining of the dissertation, bulk flow variables located at the start of the pseudoshock will be defined in state 0, the corresponding flux-conserved variable will be in state 1, and the post pseudoshock variables in state 2.

The flux-conserved values of state 1 (M_1 and P_1) are now derived for various datasets [98, 33, 120, 89] using the following approach presented by Sullins & McLafferty [120]. This method requires only a minimal amount of information at the shock train foot: the centerline Mach number M_0, the centerline temperature T_0, the wall pressure P_0 and boundary layer confinement ratios $\mathcal{A}_* = A_*/A$ and $\mathcal{A}_\theta = A_\theta/A$. When flow conditions are provided at the nozzle exit plane, as in Merkli *et al.* experiment, Fanno equations are used to estimate the

bulk Mach number M_0 and wall static pressure P_0 upstream of the shock train foot. First the thrust F is evaluated from Eq. 4.3. The mass flow rate $\dot{m}$ is also estimated from Eq. 4.4. The stream-thrust-averaged speed U_{sta} is then computed from Eq. 4.5. Next, all cases being considered adiabatic, the conservation of total enthalpy gives the local temperature T as a function of speed U_{sta} which is then used to compute M_1. P_1 is finally derived from Eq. 4.7.

The flow conditions of all datasets considered in the present study are presented in Tab. 4.1. In the DNS dataset [33], F and $\dot{m}$ can be directly integrated. This allows to assess the accuracy of the approximation made with Eqns. 4.3 and 4.4. Interestingly, the approximations are very good : F is evaluated at 303.5 and 306.1 kg.m^{-3}.s^{-2} using the direct integration and approximation respectively. Likewise, the mass flow rate is directly integrated at 0.513 and approximated to 0.520 kg.m^{-2}.s^{-1}.

$$F = P_0 \; A \; [1 + \gamma M_0^2 \; (1 - \mathcal{A}_* - \mathcal{A}_\theta) \;] \tag{4.3}$$

$$\dot{m} = P_0 \; M_0 A \sqrt{\frac{\gamma}{RT_0}} (1 - \mathcal{A}_*) \tag{4.4}$$

$$U_{sta} = \frac{\gamma}{\gamma + 1} \frac{F}{\dot{m}} \; + \; \left[\frac{\gamma}{\gamma + 1} \frac{F}{\dot{m}} \; - \; \frac{2\gamma R T_t}{\gamma + 1} \right]^{\frac{1}{2}} \tag{4.5}$$

$$M_1 = U_{sta} \; / \; \left[\gamma R \big(T_t - \frac{U_{sta}^2}{2 c_p} \big) \right]^{\frac{1}{2}} \equiv \; U_{sta} \; / \; \left[\frac{\gamma R}{c_p} \frac{\int h \; U \; dS}{\int U \; dS} \right]^{\frac{1}{2}} \tag{4.6}$$

$$P_1 = \frac{F}{A} - \frac{\dot{m} U_{sta}}{A} \tag{4.7}$$

The maximum total pressure recovery is computed from state 1 assuming no losses due to friction and adiabatic walls, *i.e.* simply using normal shocks relations (McLafferty proposes a correction to account for friction). The total pressure recovery from state 0 is found to decrease when the inflow boundary layer thickens as seen in Figs. 4.2 and 4.3. An increase

of $\mathcal{A}_*$ essentially reduces the flux-conserved Mach number M_1 and therefore the maximum pressure rise ratio. A normal shock pressure rise is recovered in the absence of a boundary layer at the foot of the shock train as shown in Figs. 4.2 and 4.3, in accordance with compressible inviscid theory.

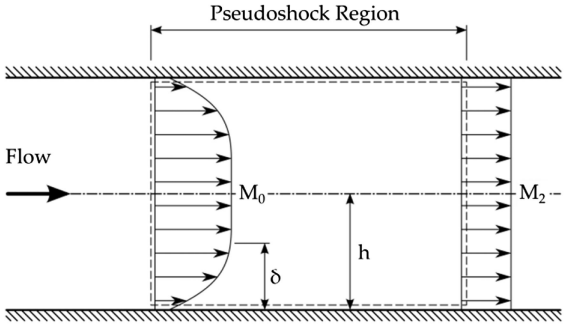

Figure 4.1: Control volume for the flux conserved analysis of McLafferty [88].

McLafferty's pressure recovery model requires a complete description of the inflow boundary layer. However, information on the displacement and momentum thicknesses profiles are often unavailable in experimental data (δ^* and θ). When measured, they are usually located far from the sidewall and corner effects are therefore neglected. On the other hand, numerical simulations can overcome such limitation and compute accurate 3D flux-conserved properties.

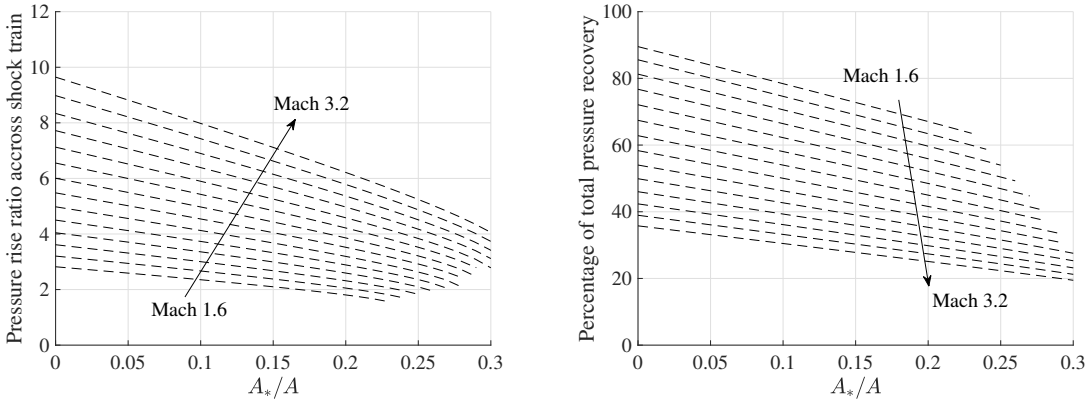

Figure 4.2: (Left) Maximum pressure rise ratio for various confinement ratio A^*/A and bulk inflow Mach number M_0. (Right) (Left) Maximum total pressure recovery for various confinement ratio A^*/A and bulk inflow Mach number M_0.